Universität Rostock Traditio et Innovatio

Improved Magnetic Resonance Velocimetry to Acquire Velocity and Turbulence Statistics for Nuclear Reactor Safety Problems

Dissertation

zur Erlangung des Gerades

Doktor-Ingenieurin (Dr.-Ing.)

am Lehrstuhl Strömunsgmechnanik
der Fakultät für Maschinenbau und Schiffstechnik
der Universität Rostock

vorgelegt von
Kristine John
aus Rostock

Rostock, 2023

https://doi.org/10.18453/rosdok_id00004598

1. Gutachter:	Prof. Dr.-Ing. habil. Sven Grundmann Universität Rostock
2. Gutachter:	Prof. Dr. rer. nat. habil. Oliver Speck Otto-von-Guericke-Universität Magdeburg
Tag der Einreichung:	21.08.2023
Tag der Verteidigung:	27.11.2023

Abstract

Magnetic resonance velocimetry (MRV) is a comparatively new measurement method in experimental fluid dynamics, which neither requires tracer particles nor visual or physical access to the flow field. In recent years, nuclear reactor safety (NRS) problems have been identified as an application that could greatly benefit from this measurement technique. In particular, MRV can provide comprehensive experimental data for validating computational fluid dynamics (CFD) methods that are used to predict the flow field in fuel assemblies. Besides the established measurement of the mean velocity vector, the main object of this work is to extend the data acquisition to turbulence statistics, as MRV enables quantifying the Reynolds stress tensor. The measurements are performed on an MRV-compatible replica of the OECD/NEA-KAERI benchmark that proposed two generic fuel assembly designs to assess results from different CFD methods. The considered flow is single-phase and isotherm. Laser Doppler velocimetry (LDV) reference data is available from the benchmark studies, which allows for verifying the MRV results but also enables highlighting its advantages over optical measurement techniques. The data acquired using MRV includes the three-component (3C) mean velocity vectors in a three-dimensional (3D) volume covering the flow field over a length of more than 300 mm. In addition, the entire six-component (6C) Reynolds stress tensor (RST) is quantified in two-dimensional (2D) field of views (FOVs) similar to the positions investigated in the benchmark exercise. Particular focus is placed on reducing the effect of systematic errors arising from the complex fluid motion to meet the requirements for CFD-grade experiments defined by the Nuclear Energy Agency (NEA). The thesis identifies improvements in MRV that substantially reduce the effect of errors in the measurement data. As a result, the comparison with the reference data from the benchmark study yields an excellent agreement and emphasizes the considerable value that MRV can provide in the assessment of CFD methods.

Kurzfassung

Die Magnetresonanz-Velocimetrie (MRV) ist eine relativ neue Messmethode in der experimentellen Strömungsmechanik, die weder Tracerpartikel noch einen visuellen oder physischen Zugang zum Strömungsfeld erfordert. In den letzten Jahren wurde die nukleare Reaktorsicherheit (NRS) als ein Anwendungsgebiet identifiziert, das von dieser Messtechnik stark profitieren kann. Dies gilt insbesondere für die Validierung von CFD-Methoden, die zur Vorhersage des Strömungsfeldes in Brennstabbündeln eingesetzt werden. Neben der Messung der mittleren Geschwindigkeitsvektoren ist das Hauptziel dieser Arbeit auch den Reynolds'schen Spannungstensor zu erfassen. Die Messungen werden an einer Nachbildung des OECD/NEA-KAERI-Benchmarks durchgeführt. Die betrachtete Strömung ist einphasig und isotherm. Für die Benchmarkstudie wurden Laser-Doppler-Velocimetry (LDV) veröffentlich, die in dieser Arbeit dazu genutzt werden die Genauigkeit der MRV-Ergebnisse zu demonstrieren aber auch um deren Vorteile gegenüber etablierten optischen Messmethoden zu verdeutlichen. Die mit MRV gemessenen Daten umfassen die mittleren Geschwindigkeitsvektoren in einem dreidimensionalen Volumen, welches das Strömungsfeld über eine Länge von 300 mm abdeckt. Darüber hinaus werden alle sechs Komponenten des Reynoldschen Spannungstensor in verschiedenen zweidimensionalen Ebenen erfasst. Besonderes Augenmerk wird dabei auf die Auswirkung systematischer Fehler gelegt, die sich aus den komplexen Fluidbewegung ergeben. Der Einfluss der Messfehler muss weitesgehend reduziert werden, um die von der Nuclear Energy Agency (NEA) festgelegten Anforderungen an ‚CFD-grade'-Experimente zu erfüllen. In dieser Arbeit werden Verbesserungen in der MRV identifiziert, die die Auswirkungen von Fehlern in den Messdaten erheblich reduzieren. Der abschließende Vergleich mit den Referenzdaten aus der Benchmarkstudie zeigt eine signifikant verbesserte Übereinstimmung und unterstreicht den erheblichen Wert, den die MRV bei der Bewertung numerischer Methoden bieten kann.

Acknowledgments

I feel deeply grateful for the enriching experience I had while working on my thesis at the MRI flow lab. I want to express my sincere appreciation to my supervisor, Prof. Dr.-Ing. habil. Sven Grundmann, for his guidance and the ability to participate in this outstanding project. I am also indebted to my colleagues at the Institute of Fluid Mechanics for their constant support and helpful discussions. I want to thank Martin, Swantje, and Caro, particularly, for their thoughtful comments on this thesis. Additionally, I am grateful for the valuable discussions and assistance I received from external research colleagues Markus and Hidajet, as well as Simon and Sebastian. Furthermore, I am thankful for all the contributions made by students to realize the experimental setup. Finally, I would like to thank my family and friends who encouraged me on my way.

This thesis was supported by the Federal Ministery for the Environment, Nature Conservation, Nuclear Reactor Safety, and Consumer Protection of Germany (BMUV) under grand number 1501602.

Contents

Part I.

Introduction

1. Purpose of this Study

In the past decades, MRV has contentiously proven its capability to provide new insights to technical flows. Its advantage over established methods is the capability to acquire data in a 2D or 3D FOV without optical or physical access to the region of interest (ROI). A further remarkable feature of MRV is its ability to capture millions of mean velocity vectors within a few hours. The data is comparable to the results from a Reynolds-averaged-Navier-Stokes (RANS) simulation or can serve as a time-averaged reverence of scale resolving CFD methods.

Among others, NRS was identified as a field of application that could benefit significantly from this measurement technique, especially regarding the validation of CFD methods. CFD enables a comprehensive prediction of the flow field inside the reactor core. However, the scales of turbulent fluctuations are partly or entirely modeled with a variety of approaches available to incorporate their influence on the flow field. It is, therefore, necessary to find the most reliable CFD method for addressing a particular problem. In this process, experimental data are a crucial element to assess the numerical methods, and the comprehensive data available from MRV enables a detailed analysis of their reliability. A remarkable feature of MRV is the acquisition of flow properties in a three-dimensional region of interest, allowing for a full-field validation of the numerical results as it is demonstrated in studies by Bruschewski et al. (2022) and Wüstenhagen et al. (2021, 2023).

The work presented in the following has been undertaken as part of the 'MRV4NRS' project, funded by the Federal Ministery for the Environment, Nature Conservation, Nuclear Reactor Safety, and Consumer Protection of Germany (BMUV) under grand number 1501602. The general objective of the project was to provide experimental data from MRV for the validation of CFD methods used to predict the flow field in fuel assemblies of pressurized water reactor (PWR). Spacer grids with mixing vanes are implemented in these fuel assemblies to support the fuel rods and enhance the heat transfer inside the reactor core. A common approach to experimentally investigate the flow created by the spacer grids is to consider single-phase flows at ambient conditions, which can straightforward be accomplished by means of MRV, and had been realized in previous studies by Piro et al. (2016, 2017), Bruschewski

et al. (2020, 2021b), and Oliveira et al. (2020, 2021).

The measurements presented in these prior studies were limited to the acquisition of the mean velocity vector. However, MRV also enables quantifying turbulence statistics in terms of the RST. The principles of the underlying imaging method are well known but have mainly been optimized for medical applications, while studies using MRV turbulence acquisition at reactor-relevant Reynolds numbers are limited (Elkins et al., 2009; Schmidt et al., 2021b). Nonetheless, information on the turbulence statistics allows for a more detailed interpretation of the flow and provides more comprehensive data for the assessment of CFD results, making it desirable to optimize this method for applications in technical flows such as in fuel assemblies.

In this process, the focus is on identifying and minimizing the influence of errors. It is well known from medical and technical applications that MRV is prone to motion-induced systematic measurement errors (Bruschewski et al., 2019). Significant sensitivity to these errors was in particular found in the acquisition of the Reynolds stresses (Schmidt et al., 2021b; John et al., 2022).

Various imaging techniques can be implemented in MRV, whereby the most suitable methods depend on the respective field of application. This is not only due to the different flow conditions and measurement systems but also due to the requirements placed on the measurement method. For example, short acquisition times are desired in medical examinations whereby loss of quantitative accuracy may be acceptable. In contrast, measurements in technical applications can take several hours to days to obtain the most accurate results.

This thesis presents measurements in an MRV-compatible replica of the OECD/NEA-KAERI benchmark (NEA, 2013). The benchmark investigates the single-phase flow in a fuel assembly model of a PWR reactor core at Reynolds-number 50 250 with different generic spacer grid designs to enhance the mixing of the flow medium. The objective of this experimental study can be summarized as follows:

- provide more comprehensive data for the validation of single-phase CFD methods used to predict the flow in fuel assemblies.
- identify measurement routines with low sensitivity to systematic errors to meet the requirements on experimental data to be used for CFD validation
- improve the accuracy of MRV turbulence quantification at reactor-relevant Reynolds numbers

The following chapter contextualizes this thesis in the current state of research, followed by part II where a description of turbulent flows as they occur in the

fuel assembly model (chapter 3), the functionality of MRV (chapter 4), and its application in turbulent flows (chapter 5) are discussed.

Part III presents the measurement campaign conducted in the replica of the OECD/NEA-KAERI benchmark, with details on the experimental methods (chapter 6), the flow conditions (chapter 7) and the accuracy and results of data acquisition downstream of both spacer grid designs (chapter 8 and 9). The results of this study are compared in part IV to the experimental data and the findings of the OECD/NEA-KAERI benchmark study to identify the reliability and the advantages of MRV in this context. The thesis concludes in part V with a summary of this thesis and aspects of ongoing and future work.

2. State of the Art

This chapter summarizes different aspects to contextualize this study within the current state of research. This includes an introduction to the OECD/NEA-KEARI benchmark chosen to be investigated by means of MRV, followed by a review of the concept of CFD-grade experiments proposed by the NEA. Finally, an overview of studies that have utilized MRV in technical flows, particularly for examining the flow field in fuel assembly models, is presented. The chapter closes with an overview of the intended progress in this thesis compared to the previous work at the MRI Flow Lab that aimed to establish MRV as a reliable measurement technique in experimental fluid mechanics for research and industrial-relevant applications.

2.1. OCED/NEA-KAERI Benchmark

Nuclear power plants provide electrical energy from nuclear fission. The first reactors were built in the 1950s and are providing 10 % of the world's electricity today (IAEA, 2022). Many nations continue to expand nuclear power to meet the rising demand for electrical power and to replace fossil fuels. However, disasters such as Chornobyl in 1989 or Fukushima in 2011 recall the destructive power of this technology, leading to huge interest and need in nuclear reactor safety studies worldwide.

In June 2002, the NEA of the Organisation for Economic Co-Operation and Development (OECD) held a meeting of experts to define an action plan on the application of CFD to NRS problems. As the NEA Committee on the Safety of Nuclear Installations (CSNI) stated in their proceeding published shortly after the meeting, they aimed to identify NRS problems for which CFD has an advantage as well as to review the existing codes, assessment methods and guidelines for its application (NEA, 2002).

A result of these efforts is the regular workshop 'CFD4NRS' that started in 2006 to exchange recent progress of CFD modeling, verification, and validation related to NRS. Several blind benchmarks emerged from these meetings focusing on various NRS-related issues such as thermal fatigue, hydrogen behavior, and turbulence in rod bundles. The so-called OECD/NEA-KAERI benchmark study addressed the latter problem by examining the reliability of

CFD methods to predict the flow field in different fuel assembly models of a PWR.

PWR are the most common design for nuclear power plant today (IAEA, 2022). In the reactor core, the nuclear material is stored as pellets in rods surrounded by cladding, and light water serves as a moderator and coolant. Cooling the fuel rods is required to dissipate the heat emitted from nuclear fission for power generation, but it is also crucial for the safe operation of the reactor. Insufficient cooling may result in the destruction of the cladding and the emission of radioactive radiation. Therefore, detailed knowledge of the flow field inside the reactor core is essential to understand the mixing of the coolant and, thus, maintain the safe operation of the power plant.

The fuel rods are assembled using spacer grids equipped with vanes to increase the mixing of the coolant, thereby optimizing the heat transfer. For this reason, identifying the optimal design of the spacer grids is of great relevance. In the OECD/NEA-KAERI benchmark, the accuracy of CFD methods is compared in a fuel assembly model of 5x5 equally sized fuel rod models, which is a common scaling in the experimental investigation of fuel assemblies. Two generic spacer grid designs were proposed, representing a split-type and a swirl-type mixing vane configuration. Figure 2.1 depicts a realistic fuel assembly design by Framatome Inc.(Courbevoie, France) with 17x17 fuel rods used in a PWR and the generic 5x5 fuel assembly designs proposed in the OECD/NEA-KAERI benchmark study.

The benchmark was intended as a blind benchmark exercise. Inlet flow conditions and experimental reference data were provided by the Korea Atomic Energy Research Institute (KAERI) to assess the numerical results. Chang et al. (2014) performed LDV measurements in a horizontal cold loop facility with both fuel assembly designs at ambient pressure and temperature. The setup is named MATiS-H, the acronym for *Measurement and Analysis of Turbulent Mixing in Subchannels-Horizontal*.

When the blind benchmark started in April 2011, 48 participants out of 22 countries had registered to participate, which illustrates the relevance of this project. Twenty-five of the participants handed in CFD results before the opening of the experimental results on May 30th, 2012. The report of NEA (2013) summarizes these and further details on the benchmark task and the comparison of the results. Additionally, Chang et al. (2014) provide a comprehensive description of the experimental study, and Lee et al. (2014) discusses the synthesis and ranking of the numerical results.

Although LDV is a precise measurement technique, some doubts about the validation of CFD methods based on these data are documented. In the summary of the benchmark (NEA, 2013), it is addressed that participants were

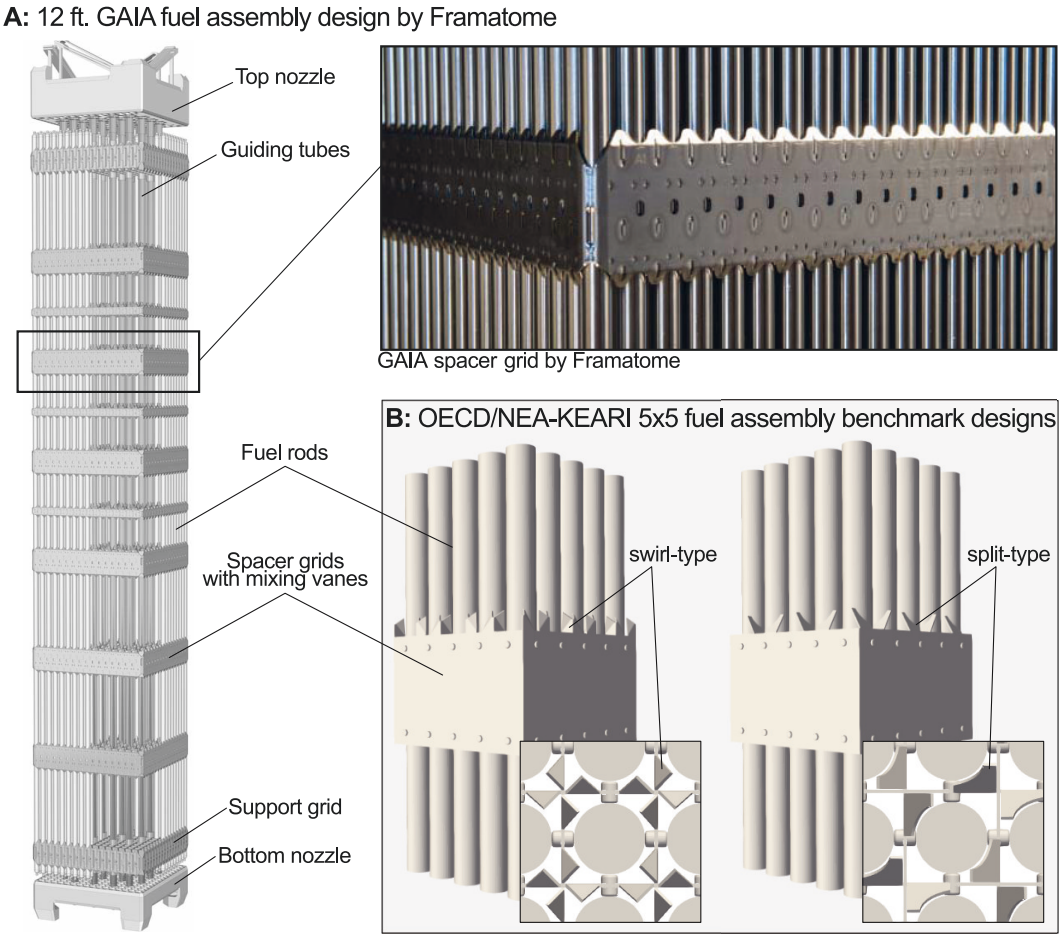

Figure 2.1.: Fuel assembly in a pressurized water reactor. **A**: Realistic design GAIA by Framatome Inc., and **B**: generic fuel assembly models proposed in the OECD/NEA-KEARI benchmark study (NEA, 2013). Pictures of GAIA fuel assembly and GAIA spacer grid: ©2018 Framatome Inc.(Framatome, 2018)

concerned about the impact of the experimental setup on the flow field, as an outlet manifold was required to provide optical access. The measurement plane was only 10 mm away from this outlet. Furthermore, moving the spacer grid to take measurements at different distances between the measurement plane and the mixing vanes was necessary. MRV does not require optical access to the flow field, allowing for simpler outlet conditions in the experimental setup.

Moreover, the synthesis of the results by Lee et al. (2014) yields that the amount of data used for comparison affects the ranking of the CFD methods. The results are evaluated by using one-dimensional (1D) profiles of the velocity and turbulence intensity and comparing the vorticity and the circulation obtained in an entire subchannel. Lee et al. (2014) found that the rankings obtained from the different metrics are not related, as, for example, the top three methods to predict the vorticity only reached a middle rank when considering the velocity and turbulence intensities. Furthermore, the ranking varied for different distances to the spacer grid. With MRV, the three-dimensional data

acquisition enables a full-field assessment of numerical results, resolving these ambiguities.

2.2. CFD-Grade Experiments

CFD is a promising and well-established approach to predicting flow fields in complex structures. However, verification and validation of the mathematical models used to describe reality must be considered. Therefore, large organizations such as the NEA as part of the OECD proposed guidelines for the assessment of numerical methods. The NEA focused especially on the application of CFD methods in nuclear reactor safety studies. Since the previously mentioned meeting of experts in 2002 (NEA, 2002), writing groups have formed to organize the different activities that aimed to identify NRS problems that benefit from the application of CFD (NEA, 2015b), define the assessment of CFD methods (NEA, 2015a), and the extension of CFD on multi-phase flows (NEA, 2014).

Among these activities, MRV measurements can assist in the assessment process, which generally involves verification, validation, and demonstration. While verification ensures that the equations are solved correctly, which is mainly addressed by the code developers, validation and demonstration are highly application-dependent and need to be supported by experimental results (NEA, 2022).

Experimental data of the flow field inside the reactor core is most commonly obtained using optical measurement methods such as LDV (Caraghiaur et al., 2009; Chang et al., 2008; Castro et al., 2020) and particle imaging velocimetry (PIV) (Conner et al., 2013; Matozinhos et al., 2020, 2021; Xiong et al., 2020). In these experimental studies, the flow inside the fuel assembly models is conventionally investigated under isotherm conditions, at ambient pressure and temperature, and at Reynolds numbers in the order of 10^5. Even though numerous experimental studies had been performed on the coolant flow inside a fuel assembly, it was recently identified by the NEA that distinct requirements for experimental data need to be defined to ensure the reliability of the validation (NEA, 2022).

The guidelines proposed by the NEA define the deviation between experiment Y_D and simulation Y_S as the comparison error δ_C. As both methods show an error against the unknown true value Y_T, the comparison error δ_C can also be defined as the difference between simulation error δ_S and experimental

error δ_E (NEA, 2022):

$$\delta_C = Y_S - Y_E = (\delta_E + Y_T) - (\delta_E + Y_T) = \delta_S - \delta_E = \delta_{model} + \delta_{num} + \delta_{input} - \delta_E. \tag{2.1}$$

The experimental error δ_E includes all uncertainties arising from the measurement process. The simulation error δ_S holds the error arising from the physical model δ_{model}, the numerical error δ_{num}, and the input error δ_{input}. The latter regards errors resulting from the selection of the inlet and boundary conditions and the material properties. The numerical error δ_{num} describes the deviations arising from the numerical approximation of the computational model compared to its exact solution. Finally, the modeling error δ_{num} describes the deviation between the chosen computational model and the correct value and is, therefore, the objective of the validation process.
The uncertainty of the comparison error $\tilde{\sigma}_C$ results from the combined uncertainties of all errors arising in the numerical and experimental process (NEA, 2022):

$$\tilde{\sigma}_C = \sqrt{\tilde{\sigma}^2_{model} + \tilde{\sigma}^2_{num} + \tilde{\sigma}^2_{input} + \tilde{\sigma}^2_E}. \tag{2.2}$$

In the proposal of the NEA (2022), the uncertainties $\tilde{\sigma}_{inlet}$, $\tilde{\sigma}_{num}$, and $\tilde{\sigma}_E$ are considered as the validation uncertainty $\tilde{\sigma}_{val}$, which then yields the modeling uncertainty

$$\tilde{\sigma}_{model} = \sqrt{\tilde{\sigma}^2_C + \tilde{\sigma}^2_{num} + \tilde{\sigma}^2_{input} + \tilde{\sigma}^2_E} = \sqrt{\tilde{\sigma}^2_C + \tilde{\sigma}^2_{val}}. \tag{2.3}$$

The guidelines of the NEA (2022) conclude, that when the validation uncertainty $\tilde{\sigma}_{val}$ is small, the modeling uncertainty $\tilde{\sigma}_{model}$ corresponds to the comparison uncertainty $\tilde{\sigma}_C$. Thus, experiments aiming to be classified as CFD-grade need to provide low experimental errors δ_E and precise documentation of the inlet- and boundary conditions, the flow medium, and the material properties of surfaces and solids included in the region of interest to minimize the inlet error δ_{input}.
Besides this, the requirements specify that sufficient local measurements and flow parameters must be acquired. Whereby the latter depends on the CFD method to be evaluated. For example, large-eddy-simulation (LES) methods can only be fully validated if the frequency spectrum of the turbulent fluctuations is quantified.

2.3. Capabilities of Magnetic Resonance Velocimetry

MRV is a measurement method evolved from magnetic resonance imaging (MRI) that enables the acquisition of various flow properties and is, therefore, of great relevance for engineering applications (Elkins and Alley, 2007; Bonn et al., 2008). Established methods are based on phase-contrast magnetic resonance imaging (PC MRI) similar as proposed by Markl et al. (2003) for medical applications. Recent studies used the technique, for example, to investigate the 3D flow field in turbine blade cooling systems (Bruschewski et al., 2022; Wüstenhagen et al., 2023), the temperature distribution in heat exchangers (Buchenberg et al., 2016; Bruschewski et al., 2021c), and combined with concentration measurements to visualize film cooling (Gunady et al., 2021). Measurements of velocity and turbulence statistics in established generic flow designs such as the backward facing-step (Elkins et al., 2009), a channel of periodic hills (Schmidt et al., 2021b), and the FDA-benchmark nozzle (John et al., 2022), enabled comparisons with results from optical measurements and demonstrated the accuracy of MRV. In addition, velocity-sensitive MRI is applied in chemical and process engineering (Gladden and Sederman, 2017; Janiga et al., 2017). However, the expression MRV is not entirely established in non-medical applications of flow-sensitive MRI, even though the underlying techniques are similar.

The term magnetic resonance *velocimetry* was introduced by Elkins et al. (2003), who acquired the mean velocity field in an internal turbine blade cooling system using velocity-sensitive MRI. Later, Elkins and Alley (2007) clarified that MRV encompasses all MRI methods to quantify flow properties, which is the definition followed in this work.

Compared to conventional optical or probe measurements, the main advantage of MRV is its capability to provide two- or three-dimensional insights into technical flows without any optical or physical access to the region of interest. Inside the FOV, the entire flow field is acquired, including the wall boundary layers within the discretization limits of the spatial resolution. No index-matching or tracer particles are required. Moreover, the measurement method is comparatively fast: millions of data points of a three-dimensional mean velocity field are captured and post-processed within a day. Limitations apply only to the available spatial and temporal resolution. With a medical human MRI system as used in this study, a compromise between measurement time, signal-to-noise ratio (SNR), and spatial resolution in setups of the size of the fuel assembly model is reached at 1 mm. Moreover, MRV cannot resolve the scales of turbulent motion but can provide turbulence statistics in terms

of the RST.

Studies using MRV to investigate coolant flows in fuel bundles have first been reported in a simplified model of a Canada Deuterium Uranium (CANDU) with eight fuel elements by Piro et al. (2016) and later with 37 fuel elements (Piro et al., 2017). Both aimed to evolve experimental and numerical methods for predicting geometry-induced mixing inside the fuel assembly. In a final measurement campaign, the influence of a deformed CANDU pressure tube that holds the fuel assembly was investigated, and the results were validated using LDV measurements (Bruschewski et al., 2020; Piro et al., 2020). Another research group used MRV to examine the influence of blocked subchannels resulting from a loss of coolant accident on the flow inside a PWR fuel assembly model (Oliveira et al., 2020, 2021). Preliminary to this study, MRV measurements of the 3D velocity field in a fuel assembly model with mixing grids derived from a realistic design by Framatome GmbH (Erlangen, Germany) were performed at the same MRI facility and compared to numerical results (Bruschewski et al., 2021b). All of these studies showed promising results, but were limited to the acquisition of the 3D mean velocity vector. The following section outlines the intended progress in this thesis to improve the measurement method and extend the acquisition to the RST.

2.4. Intended Progress Compared to Previous Work

The work presented in the following merges established methods of velocity-sensitive MRI, also known as MRV, to accurately acquire the flow field in the OECD/NEA-KAERI benchmark. The selection of methods and the concept of this work evolved from previous work undertaken at the MRI Flow Lab at the University of Rostock. This laboratory is settled at the Faculty of Mechanical Engineering and Marine Technologies and is dedicated to applying MRV in engineering and scientific research. This section outlines joint previous developments of the author of this thesis with colleagues at the MRI Flow Lab and external institutes. Furthermore, it identifies the improvements needed to meet the objective of this thesis.

The work on this thesis started with the opening of the laboratory in 2018. The general aim was to strengthen the position of MRV as a reliable method in experimental fluid mechanics. A first achievement was the implementation of a measurement method with low sensitivity to flow-induced errors named single point imaging with synchronized encoding (SYNC SPI)(Bruschewski et al., 2019) to acquire the mean velocity vector. Follow-up measurements with this method in a Venturi nozzle in cooperation with the University of

Delft yielded accurate results up to flow velocities of $12\,\mathrm{m\,s^{-1}}$ (John et al., 2020). A drawback of the method is the significant extended acquisition time which is why John et al. (2020) also investigated the utilization of innovative under-sampling techniques such as those proposed by Lustig et al. (2007) for medical applications. Nonetheless, treating this method as a gold standard for validating new measurement concepts appeared more feasible than using it regularly in common MRV applications. This conclusion placed the focus on optimizing the experimental setups and conventional PC MRI to achieve accurate results at convenient acquisition times.

Moreover, collaborations with MRI experts evolved to extend the capabilities and the accuracy of MRV to other flow parameters. Joint publications emerged regarding the measurement of temperature (Bruschewski et al., 2021c), convective acceleration (Schmidt et al., 2021a), and turbulence quantification (Schmidt et al., 2021b; John et al., 2022). At the same time, CFD users of Framatome GmbH (Erlangen, Deutschland) expressed their interest in using MRV in the assessment of CFD methods, which resulted in the implementation of a first test facility to perform experiments at reactor-relevant Reynolds numbers (Bruschewski et al., 2021c).

Several aspects emerged from these studies that are addressed and improved in this thesis. The results of the preliminary measurements in a fuel assembly model at the MRI Flow Lab were promising but had been limited to the acquisition of the mean velocity vector. Additionally, the calculated flow rate along the channels axis yielded strong deviations due to systematic errors inside and downstream of the spacer grid (Bruschewski et al., 2021b).

Moreover, extending the measurements in fuel assembly models to the acquisition of the Reynolds stresses was found to be desirable. However, the previous studies at the MRI Flow Lab acquired the turbulence statistics in comparatively simple geometries and identified a substantial impact of systematic errors in shear layers (Schmidt et al., 2021b; John et al., 2022). The flow in the fuel assembly model is much more complex due to the vortices formed by the mixing vanes. Thus, the velocity gradients and higher orders of motion occurring in this geometry are expected to significantly increase the sensitivity to systematic errors. As it is desirable to acquire the complex flow field evolving in the fuel assembly in 3D or multiple 2D measurements, the application of SYNC SPI to overcome these errors is inconvenient due to the extended acquisition time. Thus, an improved method to acquire mean velocity and turbulence statistics must be identified in this study to use MRV for NRS problems.

Part II.

Theory

The previous part highlighted the need for experimental data in the assessment of CFD methods in NRS studies and identified the potential of MRV to provide such data. This part focuses on the theory of turbulent flows, the general imaging principle of MRI, and the functionality of velocity-sensitive MRI, which is here referred to as MRV.

Chapter 3 summarizes the characteristics of turbulent flows as they occur in the fuel assembly model to understand the validity of time-averaged measurement data provided by MRV. Even though fluctuations at a high dynamic range characterize these flows, they can be considered statistically stationary at appropriate circumstances, allowing for an investigation based on time-averaged metrics. All analyses refer to single-phase and isothermal flows as realized in the experimental investigation of the fuel assembly model.

The Reynolds decomposition is a familiar concept for analyzing such flows based on the mean velocity and the velocity fluctuations. If implemented in the Navier-Stokes equations, this result in the RANS equations and yield the Reynolds stresses. In CFD methods based on these RANS equations, various models exist to approximate the Reynolds stresses, making it necessary to find the most appropriate method for a certain application.

Both metrics, mean velocity and statistics of the fluctuations in terms of the Reynolds stresses, can be acquired using MRV, which emphasizes its significance for the assessment of RANS CFD methods. The functionality of magnetic resonance imaging and its expansion to MRV are discussed in chapter 4. The methods discussed here and used in this thesis are based on Cartesian PC MRI similar to the well-known 4D Flow sequence design by Markl et al. (2003).

Several studies have demonstrated the ability of MRV to provide reliable data in technical flows, especially when considering the mean velocity vector. However, the fluid motion causes numerous systematic errors that must be attended to satisfy the requirements of CFD-grade experiments. Therefore, chapter 5 is dedicated to the accuracy of MRV in turbulent flows and a short overview of imaging methods that are favorable for the desired measurements in the fuel assembly model.

3. Fundamentals of Turbulent Flows

This chapter focuses on the fluid mechanical basics of the turbulent flow inside the fuel assembly model. As it is not possible to replicate the actual operational conditions of the nuclear reactor in an experimental environment, and the focus is on the assessment of the turbulence models used in single-phase CFD methods, the flow is deemed to be single-phase, steady-state, and isotherm. As in a realistic PWR, the flow medium is water, but measurements are performed at ambient temperature and pressure, making the flow medium a constant-property fluid. Previous experimental studies investigating the flow field in fuel assemblies have assumed similar boundary conditions. Common concepts on turbulent flows considered in the following are summarized from Pope (2000) and Tropea et al. (2007), in particular from the chapters by Romano et al. (2007) and Panton et al. (2007). The last section reflects the metrics considered in previous experimental studies to analyze the turbulent flow in fuel assemblies models.

3.1. Similarity of Flows

Compared to the experimental study performed by Chang et al. (2014) on the benchmark configuration, the dimensions of the replica used in the MRV measurements are scaled to find an optimum between relative resolution and required flow velocity to reach the target flow state. In fluid dynamics, dimensionless numbers ensure the similarity of scaled flow fields and allow for comparing results from different numerical or experimental methods. In the case of the stationary, isotherm, and incompressible flow in the fuel assembly model, the Reynolds number Re must be considered. It indicates the ratio of inertial forces to viscous forces and is defined as:

$$Re = \frac{uL\rho}{\mu} = \frac{uL}{\nu}. \tag{3.1}$$

u denotes the characteristic velocity of the flow, μ is the dynamic and $\nu = \mu/\rho$ the kinematic viscosity and ρ the density of the fluid. L is a characteristic

length scale of the flow. In a non-circular channel, this length is commonly associated with the hydraulic diameter d_h defined as the ratio between the cross-sectional area of the flow A and its wetted perimeter U:

$$d_h = 4\frac{A}{U} \tag{3.2}$$

The ratio of inertial to viscous forces expressed by the Reynolds number determines whether the flow is laminar or turbulent. At low Reynolds numbers, the viscous forces predominate, and the flow elements can be considered to move in layers between which no mixing occurs. With increasing Reynolds number, disturbances in the flow are no longer damped by the viscous forces, and fluctuations of velocity, pressure, and temperature expand in the flow field. Thus, turbulent flows are characterized by a more complex dynamic in which various scales of motion are occurring.

3.2. Fluid Dynamics

In contrast to solids, liquids exhibit a constant deformation when subjected to a force. In analyzing single-phase flows, the volume elements and time scales are commonly larger than the molecular scales. Thus the parameters change continuously. When describing the flow of constant property Newtonian fluids, the mass conservation in its divergence-free form

$$\nabla \cdot \mathbf{u} = 0 \tag{3.3}$$

and the Navier-Stokes equations need to be considered. The latter evolves from Newton's second law and relates the substantial derivative of the velocity $\boldsymbol{u}(\boldsymbol{x}, t)$ to the forces acting on the flow field:

$$\frac{\mathrm{D}\mathbf{u}}{\mathrm{D}t} = \frac{1}{\rho}\nabla p + \nu\nabla^2\mathbf{u}. \tag{3.4}$$

Here, ρ is the density, p is the modified pressure, including the gravitational forces and the normal stresses, and ν is the kinematic velocity. The velocity $\boldsymbol{u} = u_i = [u, v, w]^T$ is a three-component vector, which is here considered in the three-dimensional Cartesian space $\boldsymbol{x} = x_i = [x, y, z]^T$. $\mathrm{D}/\mathrm{D}t$ is the substantial derivative defined as:

$$\frac{\mathrm{D}}{\mathrm{D}t} = \frac{\partial}{\partial t} + \mathbf{u} \cdot \nabla = \frac{\partial}{\partial t} + u_i\frac{\partial}{\partial x_i}. \tag{3.5}$$

The first term yields the local derivative in time, while the latter holds the convective change. The local derivative $\partial/\partial t$ is zero for stationary flows. Theoretically, the equations 3.3 and 3.4 yield four independent equations to quantify the three components of the velocity vector and the pressure.

However, small time increments and high spatial resolution would be required in turbulent flows to resolve all scales of motion arising from the random fluctuations that expand in the flow field. The statistics of these fluctuations will be discussed in more detail in the following subsection 3.4. A common approach in the analysis of turbulent flows is the Reynolds decomposition, where the velocity $\boldsymbol{u}(\boldsymbol{x}, t)$ is described by its mean value $\langle \boldsymbol{u}(\boldsymbol{x}) \rangle$ and its fluctuations $\boldsymbol{u}'(\boldsymbol{x}, t)$:

$$\boldsymbol{u}(\boldsymbol{x}, t) = \langle \boldsymbol{u}(\boldsymbol{x}) \rangle + \boldsymbol{u}'(\boldsymbol{x}, t). \tag{3.6}$$

Including equation 3.6 to the Navier-Stokes equations in 3.4 for stationary flows ($\partial/\partial t = 0$) yields the RANS equations:

$$\rho \langle u_j \rangle \frac{\partial \langle u_i \rangle}{\partial x_j} = \nu \nabla^2 \langle u_j \rangle - \frac{\partial \langle u_i' u_j' \rangle}{\partial x_j} - \frac{1}{\rho} \frac{\partial \langle p \rangle}{\partial x_j}. \tag{3.7}$$

It becomes apparent that with the velocity covariances $\langle u_i' u_j' \rangle$, there are too many unknowns to be solved by four independent equations. Thus, they need to be approximated by additional equations based on the mean flow parameters or by defining additional transport equations, which is known as the closure problem. The RANS equations are the basis of RANS CFD simulations, where a variety of turbulence models exist to approximate the effect of the velocity covariances $\langle u_i' u_j' \rangle$. Experimental data is then required to identify the most accurate models for a certain application.

3.3. Reynolds Stresses

The velocity covariances $\langle u_i' u_j' \rangle$ are referred to as Reynolds Stresses in this thesis, which follows the outline by Pope (2000) that is summarized here. The stresses acting on the fluid become apparent when rewriting equation 3.7 to

$$\rho \langle u_j \rangle \frac{\partial \langle u_i \rangle}{\partial x_j} = \frac{\partial}{\partial x_j} \left[\eta \left(\frac{\partial \langle u_i \rangle}{\partial x_j} + \frac{\partial \langle u_j \rangle}{\partial x_i} \right) - \langle p \rangle \delta_{i,j} - \rho \langle u_i' u_j' \rangle \right]. \tag{3.8}$$

The term on the right side of the equation reveals the three stresses acting on the fluid: the viscous stress with the dynamic viscosity η, the isotropic stresses from the mean pressure field $-\langle p \rangle \delta_{i,j}$ with $\delta_{i,j}$ being the Kronecker delta, and the stresses arising from the fluctuations $\rho \langle u_i' u_j' \rangle$. As in this thesis, the latter is conventionally considered without the density ρ when dealing with constant

property fluids. This leaves the velocity covariances $\langle u_i' u_j' \rangle$ to be referred to as the Reynolds stresses, which then have the dimension $\mathrm{m}^2\,\mathrm{s}^{-2}$.

The Reynolds stresses are the symmetric components of a second order tensor $\boldsymbol{\tau} = \tau_{i,j}$ with the diagonal components $i = j$ being the normal stresses, and the off-diagonal components $i \neq j$ being the shear stresses:

$$\boldsymbol{\tau} = \tau_{i,j} = \langle u_i' u_j' \rangle = \begin{bmatrix} \langle u'^2 \rangle & \langle u'v' \rangle & \langle u'w' \rangle \\ \langle u'v' \rangle & \langle v'^2 \rangle & \langle v'w' \rangle \\ \langle u'w' \rangle & \langle v'w' \rangle & \langle w'^2 \rangle \end{bmatrix}. \tag{3.9}$$

The specific mean kinetic energy of the turbulent fluctuations TKE, also known as turbulent kinetic energy, is quantified as half the trace of the Reynolds stress tensor:

$$TKE = \frac{1}{2} \langle u_i' u_i' \rangle. \tag{3.10}$$

As it quantifies the specific energy of the turbulent fluctuations, is it a parameter of great interest that is addressed in various turbulent models of RANS CFD.

3.4. Statistics

The previous sections discussed the analysis of turbulent flows assuming stationarity, even though turbulent flows are characterized by random fluctuations. In a fully developed turbulent flow, the fluctuations can be considered by superimposed eddies of a continuous but limited scale range. Each eddy has a size l_E, a velocity $u(l_E)$, and a time scale $T_E = l_E / u(l_E)$, whereby the characteristic scales of the largest structures are comparable to that of the flow. The Reynolds number $Re(l_E)$ of these large scales is in the same order as the Reynolds number of the flow. However, the large eddies are unstable and break down into smaller eddies. This decay can be considered a random process and continues until the viscous effects at the smallest scales dominate and their kinetic energy dissipates. Within this process, the energy transfers from larger to smaller eddies, which is referred to as the energy cascade.

Due to the random nature of the eddy decay, a fully developed turbulent flow can be considered stationary if the statistics of the fluctuations do not change over time. The temporal autocorrelation function $R_i(\boldsymbol{x}, t, s)$ is a straightforward method to analyze the random process that yields the correlation of the fluctuations u_i' in the ith-direction at the time interval s

$$R_i(\boldsymbol{x}, t, s) = \frac{\langle u_i'(\boldsymbol{x}, t) u_i'(\boldsymbol{x}, t+s) \rangle}{\langle u_i'(\boldsymbol{x}, t)^2 \rangle}. \tag{3.11}$$

For the fully developed turbulent flow, the correlation decreases with growing s, and the integral of the autocorrelation function converges to the integral time scale T_i:

$$T_i(\boldsymbol{x}, t) = \int_o^\infty R_i(\boldsymbol{x}, t, s)\mathrm{d}s \tag{3.12}$$

Thus, T_i can be considered a measure for the largest scales in the turbulent flow in the i-th direction. At times larger than T_i, there is no dependence between the velocity at the different time steps. Furthermore, the equation yields that an integral time scale can be quantified for each component of the velocity vector.

The Fourier transform of the autocovariance, which is $R_i(\boldsymbol{x}, s)\langle u_i'(\boldsymbol{x}, t)^2\rangle$ yields the frequency spectrum $E(\omega_E)$

$$E(\omega_E) = \frac{1}{\pi}\int_{-\infty}^\infty R_i(\boldsymbol{x}, t, s)\langle u_i'(\boldsymbol{x}, t)^2\rangle \exp^{-i\omega_E s}\,\mathrm{d}s \tag{3.13}$$

of the random process, where ω_E are the frequencies of the fluctuations.

The turbulent flow is statistically stationary, if these metrics are interdependent of t. Furthermore, if the fluctuations occur with a probability that follows a Gaussian distribution, the random process is uniquely described by the mean velocities $\langle u_i(\boldsymbol{x})\rangle$, the variance $\langle u_i'(\boldsymbol{x}, t)^2\rangle$ of the fluctuations, and the autocorrelation function $R_i(\boldsymbol{x}, s)$, or the frequency spectrum $E(\omega)$, respectively. Moreover, the autocorrelation function can be expressed as

$$R_i(\boldsymbol{x}, s) = \exp\left(\frac{-|s|}{T_i(\boldsymbol{x})}\right). \tag{3.14}$$

Figure 3.1 depicts this analysis for a velocity $u(t)$ measured at one point in the flow field using LDV. The data was originally acquired to validate MRV turbulence measurements in a periodic hill channel by Schmidt et al. (2021b). Additionally, the velocity distribution and the autocorrelation function of a Gaussian distributed velocity with the same variance $\langle u'^2\rangle$ are depict to illustrate the deviation to the acquired data. This aspect becomes particularly relevant in MRV turbulence quantification for which a Gaussian distributed velocity is a fundamental assumption.

Similar to temporal statistics, an analysis of the spatial scales of turbulent motion can be considered by the spatial autocorrelation function $R_i(\boldsymbol{x}, r, t)$

$$R_i(\boldsymbol{x}, r, t) = \frac{\langle u_i'(\boldsymbol{x}+r, t)u_i'(\boldsymbol{x}, t)\rangle}{\langle u_i'(\boldsymbol{x}, t)^2\rangle}. \tag{3.15}$$

which then allows calculating the integral length L_i

$$L_i(\boldsymbol{x}, t) = \int_o^\infty R_i(\boldsymbol{x}, r, t)\mathrm{d}r \tag{3.16}$$

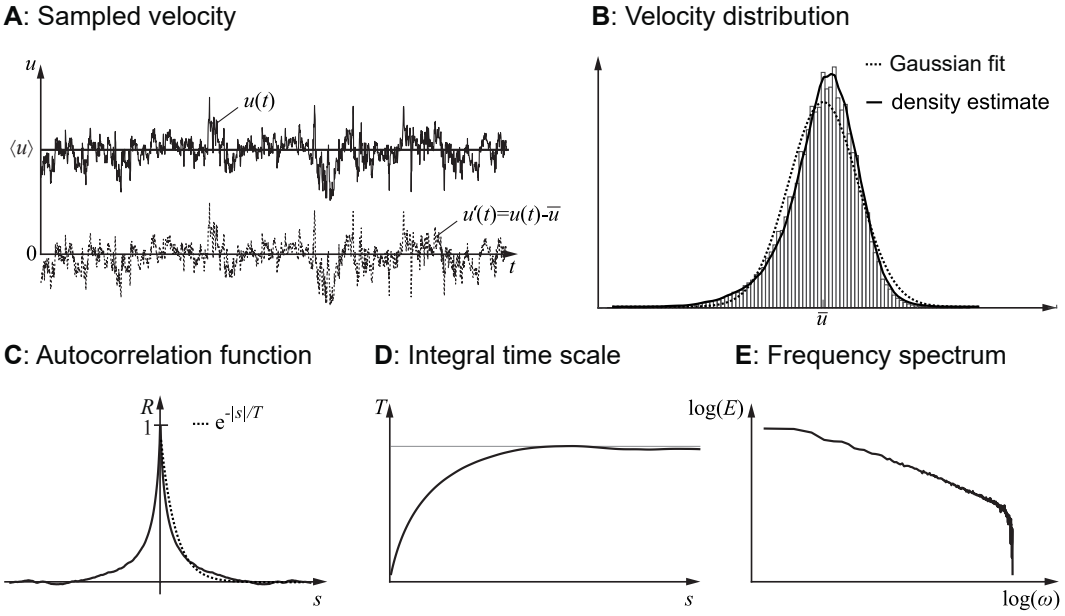

Figure 3.1.: Turbulence statistics demonstrated using an LDV measurement originally acquired for the validation of MRV RST measurements by Schmidt et al. (2020). The velocity of the passing particles over the time t is shown in **A**. From this, the velocity distribution is calculated (**B**) with its estimated probability density and a Gaussian fit of the data. The resulting autocorrelation function $R(s)$ is depicted in **C**. The dotted line indicates the autocorrelation function of a Gaussian distributed velocity. Integrating the autocorrelation function yields the integral time scale T (**D**), and the Fourier transform of the autocovariance ($R(s)\langle u_i'^2\rangle$) reveals the frequency spectrum of the fluctuations $E(\omega_E)$ (**D**). A Gaussian distributed velocity is a fundamental assumption in MRV RST measurements.

A connection between spatial and temporal scales is possible using the hypothesis on frozen turbulence, also known as Taylor's hypothesis. With regards to the convective velocity u_c of the mean motion in the flow field, this yields:

$$T_i = \frac{L_i}{u_c} \tag{3.17}$$

Having discussed statistical stationarity, two further characteristics of turbulent flows should be mentioned here, as many theoretical approaches are based on homogeneous isotropic turbulence. Homogeneity exists when the turbulence does not depend on position and thus is statistically invariant against translation. Whereas isotropic turbulence is statistically invariant against rotations, thus, the statistics of the fluctuations do not depend on the direction.

3.5. Experiments in Fuel Assemblies

This section focuses on the metrics used in previous experimental studies to characterize the flow in fuel assembly models and the possibilities of experimental flow analysis using MRV. Early attempts to experimentally investigate the

turbulent flow behind spacer grids had been performed using single-point measurement techniques, such as Pitot-tubes (Rehme, 1973; Rehme and Trippe, 1980) or LDV (Rowe, 1973). While the latter has been continuously employed, such as by Chang et al. (2008, 2014) and Castro et al. (2020), probe-based measurements have lost importance in these applications.

LDV is a non-intrusive and directional sensitive measurement technique offering a high spatial and temporal resolution at high accuracy. Depending on the number of laser beams pairs used in the measurement, LDV can provide the mean velocity vector and the Reynolds stresses. Furthermore, it allows for estimating the temporal autocorrelation function and integral time scale. However, as a single-point measurement technique, it does not enable to capture temporally evolving vortices, also known as coherent structures, in the flow field. Such data can be acquired using PIV, which instantaneously captures the velocity field in a measurement plane illuminated by laser light. Its temporal resolution allows the resolution of coherent structures in the flow field and provides estimates of the integral length scales in the region of interest. This measurement technique has been frequently used to investigate the flow field behind spacer grids in the past decade (Conner et al., 2013; Matozinhos et al., 2020, 2021).

In most studies investigating the turbulent flow field in fuel assemblies, deviations and agreements between different methods or spacer grid designs are quantified by comparing mean velocities $\langle u_i \rangle$, velocity covariances $\langle u_i' u_j' \rangle$ and turbulence intensities $u_{i,rms}$ defined as

$$u_{i,rms} = \sqrt{\langle u_i'^2 \rangle}. \tag{3.18}$$

A metric that is derived from the lateral mean velocities u and v of all n data points in an area A_{ROI} perpendicular to the stream-wise direction is the secondary flow intensity SFI

$$SFI = \frac{1}{A_{ROI}} \sum_{k=1}^{n} \frac{{}^{k}A \sqrt{{}^{k}\langle u \rangle^2 + {}^{k}\langle v \rangle^2}}{w_b} \tag{3.19}$$

which is related to the axial bulk velocity w_b. Here, ${}^{k}\langle u \rangle$ indicates the velocity of the kth data point with the assigned area ${}^{k}A$. It has been used in numerical (Busco and Hassan, 2018) and experimental studies (Matozinhos et al., 2021) to quantify the intensity of lateral flow structures created by the spacer grid.

Another parameter commonly considered is the axial vorticity ω_z

$$\omega_z = \frac{\partial v}{\partial x} - \frac{\partial u}{\partial y} \tag{3.20}$$

The axial vorticity ω_z is one component of the three-component vorticity vector $\boldsymbol{\omega}$ describing the rotation of the velocity field:

$$\boldsymbol{\omega} = [\omega_x, \omega_y, \omega_z]^T = \nabla \times \boldsymbol{u} \tag{3.21}$$

This quantity is a common parameter to identify temporally evolving coherent structures in turbulent flows. In the experimental studies on fuel assembly models, it has been mainly considered for the mean velocity components. In this context, the axial vorticity indicates stationary vortices formed by the mixing vanes and their decay downstream of the spacer grid. These structures created in the center of the sub-channel are also referred to as swirls. This analysis yields similar information as the SFI, but the vorticity also reveals the direction of rotation of the swirls.

In the synthesis of the results of the OECD/NEA-KAERI benchmark study, Lee et al. (2014) furthermore considered the axial circulation Γ_z

$$\Gamma_z = \int_A \omega_z \mathrm{d}A \tag{3.22}$$

in a single subchannel with the area A to evaluate the prediction of the vortex generation and its decay by the different numerical methods and the experimental reference data.

All of the mentioned parameters are calculated from time-averaged parameters of the flow field. Statistical quantities derived from the time-resolved measurement data, such as autocorrelation functions, integral scales, or frequency spectrum, have been considered in fewer studies, for instance, by Matozinhos et al. (2021). As stated by the NEA (2022) in their requirements for CFD-grade experiment, such data is essential in the assessment of LES methods. In contrast to RANS simulations, the turbulent scales are partially resolved in this numerical approach. For the validation of RANS methods, time-averaged data is considered sufficient to validate the turbulence model.

Previous studies using optical measurement techniques have in common that they are either limited to single-point measurements covering only a few subchannels of the fuel assembly or only provide the in-plane velocity components from 2D measurements. On the contrary, an inherent feature of MRV is its capability to perform measurements that are velocity sensitive in all three spatial directions in a 2D or 3D FOV. Besides the entire mean velocity vector, all six components of the Reynolds-stress-tensor can be acquired, enabling the turbulent kinetic energy TKE to be calculated.

In MRV, the data is captured without gaps, including all boundary layers within the discretization limits of the measurements. For 3D3C velocity measurements, the same post-processing routines as for time-averaged numerical

results can be used to visualize the mean flow structure. But more importantly, the data enables a full-field validation of numerical methods, as proposed by Wüstenhagen et al. (2021).

A popular method to visualize 3D flow structures are streamlines that are formed by the tangents of the velocity vectors

$$\frac{\mathrm{d}x_j}{\mathrm{d}x_i} = \frac{u_j}{u_i}. \tag{3.23}$$

In the flow field of fuel assemblies, streamlines enable the visualization of the swirls formed by the spacer grid, providing qualitative insights into the mixing within and between the subchannels.

The Q-criterion was initially invented to identify coherent structures in turbulent flows and is calculated from the second invariant of the velocity gradient tensor $\mathrm{d}u_i/\mathrm{d}x_j$ (Jeong and Hussain, 1995):

$$\frac{\mathrm{d}u_i}{\mathrm{d}x_j} = \underbrace{\frac{1}{2}\left(\frac{\mathrm{d}u_i}{\mathrm{d}x_j} + \frac{\mathrm{d}u_j}{\mathrm{d}x_i}\right)}_{S} + \underbrace{\frac{1}{2}\left(\frac{\mathrm{d}u_i}{\mathrm{d}x_j} - \frac{\mathrm{d}u_j}{\mathrm{d}x_i}\right)}_{\Omega}. \tag{3.24}$$

Here, S is the symmetric part and relates to the strain rate, while Ω is the asymmetric part that holds the rotation of the vector field, thus the vorticity ($\Omega = 1/2\omega$). From this, it follows that

$$Q_{crit} = \frac{1}{2}\left(||\Omega||^2 - ||S||^2\right). \tag{3.25}$$

With this metric, the three components of the velocity vectors are reduced to a scalar that identifies if the vorticity (positive values) or the strain rate (negative values) is dominant. The Q-criterion was derived as a more reliable method to identify coherent structures than the vorticity. As this requires the 3D3C velocity field at a sufficient spatial and temporal resolution, it is mainly used in the post-processing of time-resolved numerical results. However, it can also be calculated for the time-averaged experimental data obtained from MRV to visualize the swirls formed by the spacer grid.

The following chapter details the methods to quantify time-averaged data on velocity and turbulence statistics using MRV. To summarize this chapter on turbulent flows, it is worth reiterating that MRV directly provides time-averaged data of the turbulent flow field. Therefore, an analysis of the flow field from MRV measurements is at least equivalent to the optical measurements of previous studies, except for the more recent PIV studies where the autocorrelation function and the integral length scale were also considered.

The advantage over optical methods is the ability of MRV to measure all

three components of the velocity vector and all six components of the Reynolds stress tensor in a 3D region of interest without requiring visual access to the flow field. For this reason, MRV is expected to provide new insights into complex turbulent flows that occur in fuel assembly models and offer unique capabilities in validating numerical methods, especially for RANS turbulence models.

4. Magnetic Resonance Velocimetry

MRI was first introduced in the early 1970s by Lauterbur (1973) and Mansfield and Grannell (1973), even though the physical basics of the nuclear magnetic resonance (NMR) had been described years earlier. Since then, MRI has become an important technology in medical diagnostics, with extensive literature available on all aspects of the underlying physics and imaging methods.

The ability to image cardiovascular flow using PC MRI was first described in the early 1980s by Moran (1982). A few years later, Gao and Gore (1991) presented a general expression for the quantification of turbulent fluctuations in a steady flow using velocity sensitive MRI. The capabilities of MRI to quantify fluid motion have been regularly reviewed, for example, by Fukushima (1999). The reviews of Elkins and Alley (2007) and Bonn et al. (2008) emphasize the value of this method for fluid mechanics in biomedical and technical applications. Beyond that, the group of Gladden and Sederman (2013, 2017) continuously demonstrated its value for chemical and process engineering.

In most applications, capturing transient effects is not feasible with MRV, even though massive progress has been made in accelerating the measurements by using under sampled, non-Cartesian imaging methods (Markl et al., 2012; Untenberger et al., 2016). Tayler et al. (2011), for example, demonstrated measurements in which a temporal resolution of velocity-sensitive MRI of 91 frames per second was reached. However, the turbulent scales in their study are comparatively large, and the temporal resolution strongly depends on the spatial resolution and the imaging system used. Therefore, studies of high turbulent flows using conventional whole-body MRI systems can be considered to by limited to time-averaged or phase-locked measurements.

In recent MRV studies of technical applications performed on these MRI systems and using Cartesian PC MRI, the spatial resolution had been in the order of 1 mm, and the acquisition time is in the orders of minutes to hours to obtain flow parameters in a 2D or 3D region of interest at high SNR. A peculiarity of MRV is that the signal measured at each encoding step yields information from the entire FOV. Thus, the data is temporally averaged over the entire duration of the measurement. As the flow field is considered statis-

tically stationary, the obtained data is comparable to the result from a RANS simulation or provides a time-averaged reference for other CFD methods. Considering the RANS equation as introduced in section 3.2, the capabilities of MRV become apparent:

$$\underbrace{\rho \langle u_j \rangle \frac{\partial \langle u_i \rangle}{\partial x_j}}_{①} = \frac{\partial}{\partial x_j} \Bigg[\underbrace{\eta \left(\frac{\partial \langle u_i \rangle}{\partial x_j} + \frac{\partial \langle u_j \rangle}{\partial x_i} \right)}_{②} \underbrace{- \rho \langle u_i' u_j' \rangle}_{③} \Bigg] \underbrace{- \langle p \rangle \, \delta_{i,j}}_{④} \tag{4.1}$$

The convective acceleration ① and the viscous stresses ② can be derived from the MRV mean velocity measurements. Alternatively, the convective acceleration can be directly measured as shown by Schmidt et al. (2021a). Furthermore, the sensitivity to turbulent fluctuations enables to capture all six components of the Reynolds stresses ③. Finally, the pressure ④ can be derived from the measured quantities as demonstrated by Bruschewski et al. (2016b) and Haraldsson et al. (2018).

Over the past decades, MRV has proven reliable in providing the mean velocity vectors from complex 3D flow fields in various engineering applications. Increasing focus has also been placed on investigating and suppressing measurement errors, which is essential to meet the requirements of CFD-grade experiments. Fewer studies used MRV to quantify turbulence in high Reynolds-number flows, which, however, would be beneficial for validating CFD methods. This chapter provides the principles of velocity-sensitive MRI methods to quantify the mean velocity vector and the Reynolds stresses, as these parameters enable to derive the metrics identified in the previous chapter to be used in the analysis of the flow in fuel assemblies.

4.1. Principle Method of Imaging

This section summarizes the basic functionality of MRI from the books of Bernstein et al. (2004), Brown et al. (2014), and McRobbie et al. (2006). Its key principle is the interaction of the nuclear spin of the atomic nucleus with an external magnetic field. The spin is the intrinsic angular momentum of the nucleus and is a conserved quantity. If exposed to an external magnetic field, the spins are forced to precess toward the axis of the magnetic field. The angular frequency ω of this rotation depends linear on the magnetic field strength B_0 and is known as Lamor frequency

$$\omega_L = \gamma \cdot B_0. \tag{4.2}$$

Here, γ is the gyromagnetic ratio. The alignment of the spins with the external magnetic field generates a bulk magnetization parallel to it. However, it is not this equilibrium state that yields a measurable signal. Instead, a high-frequency pulse at the same frequency as the Lamor frequency causes the spins to leave the equilibrium, resulting in strong lateral components of the magnetization perpendicular to the external magnetic field. As the external magnetic field is commonly assumed to align with the z-axis, the lateral magnetization is considered in the $x-y$-plane. This magnetization $M_{x,y}$ rotates in the $x-y$-plane at the Lamor frequency ω_L

$$M_{x,y}(t) = M_x + iM_y = M_0 \exp\left(i\omega_L t + i\Phi_0\right). \tag{4.3}$$

Here, Φ_0 is the initial phase, and M_0 is the initial bulk magnetization. The excitation pulse in conventional MRI machines at a magnetic field strength of 1.5 T or higher, ω_L is in the order of 10^6 Hz, and is, therefore, referred to as radio frequency pulse (rf-pulse).

After excitation, the time-varying transverse magnetization $M_{x,y}$ induces a current in nearby receiver coils that yields the measurement signal. The strength of this signal decays due to relaxation effects minimizing the transverse magnetization. On the one hand, the spin-lattice relaxation forces the spins back to align with the external magnetic field, characterized by the time T_1. On the other hand, the interaction between the spins results in phase variations of the spins, causing their bulk magnetization to decrease. This process is characterized by the times T_2 and T_2^*. The latter considers that imperfections in the magnetic field accelerate the dephasing.

Figure 4.1 illustrates the described behavior of the magnetization vector in the equilibrium state (**A**), its path back towards the alignment with the external field after excitation (**B**), and the induced signal in the receiver coil (**C**). Due to its characteristic shape, the signal is also known as free induction

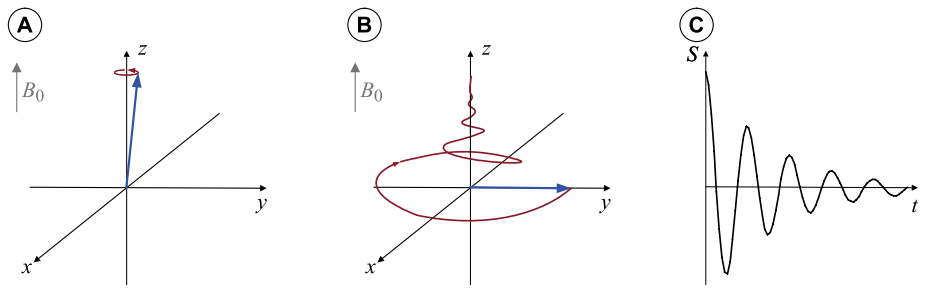

Figure 4.1.: Illustration of the spin's magnetization vector (blue arrow) in the equilibrium state (**A**) and after excitation (**B**). The red line in **B** symbolizes the path of its tip back to the alignment with the external magnetic field. The rotation of the magnetization in the transverse plane induces a signal in nearby receiver coils (**C**) that decays due to relaxation effects.

decay (FID). The decay is primarily driven by the dephasing of the spin's magnetization, as T_2^* is commonly significantly shorter than T_1.

To this point, the signal neither holds information on the spatial distribution of the spins nor details on the flow parameters. Therefore, temporary magnetic field gradients $\boldsymbol{G}(t)$ superimposing B_0 are applied to create a spatial dependency of ω_L:

$$\omega_L(\boldsymbol{x}, t) = \gamma B(\boldsymbol{x}, t) = \gamma(B_0 + \boldsymbol{G}(t)\boldsymbol{x}) \tag{4.4}$$

Here, $\boldsymbol{x}$ is the three-component Cartesian position vector, and t is the time. Due to the variation in the precession frequency, a spatially dependent phase deviation Φ in the rotation of the magnetic momentum develops:

$$\Phi(\boldsymbol{x}) = \int \omega_L(\boldsymbol{x}, t)\mathrm{d}t = \Phi_0 + \gamma \int \boldsymbol{x}\boldsymbol{G}(t)\mathrm{d}t \tag{4.5}$$

With Φ_0 being the initial phase variation, this formula holds the relation between $\boldsymbol{x}$ and Φ.

Figure 4.2 illustrates the effect of a magnetic field gradient considering the magnetization vectors at different positions. Applying magnetic field gradients causes the phase angles of the magnetization vectors to dephase, resulting in a lowered bulk magnetization. Furthermore, the effect of the spin's distribution and the strength of the magnetic gradient on the strength of the bulk magnetization is depicted. If the spin density spatially changes, the received signal intensity will differ from the signal from a homogeneous spin distribution. A certain magnetic gradient strength may result in a rephasing of the magnetization of the spin at a correlated distance and an increase in the received signal.

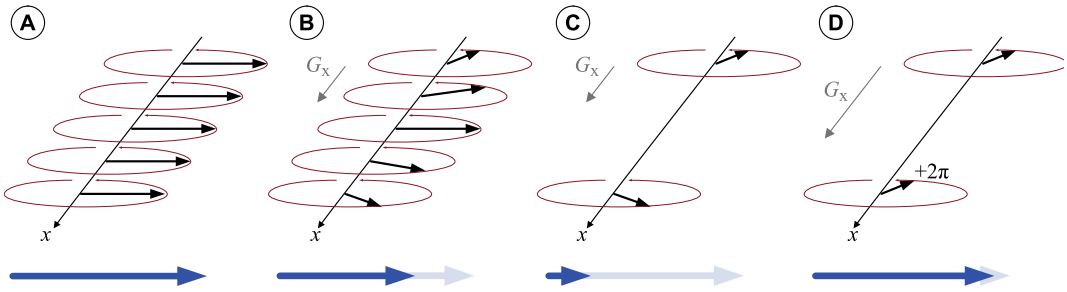

Figure 4.2.: Illustration of the effect of magnetic field gradients: If no magnetic field gradient ($G_x = 0$) is applied, the phase of all spins aligns, resulting in the maximum magnetization (**A**). Applying a magnetic gradient G_x results in a phase deviation that causes the bulk magnetization to decrease (**B**). A change in spin density results in a different bulk magnetization (**C**), but the signal recovers at a certain combination of spin distribution and magnetic gradient strength (**D**)

.

From this, the basic concept of MRI can be derived as a repeated application of magnetic field gradients $G_i(t)$ with varied strength to identify the spatial distribution of spin density, encoded in the spatial frequencies k_i

$$k_i = \int G_i(t)\mathrm{d}t. \tag{4.6}$$

A common imaging method in MRV is the gradient echo (GRE), for which a basic concept is depicted in Fig. 4.3. After the excitation, a first gradient $G_x(t)$ is applied, resulting in a dephasing and signal decay. It is followed by a second gradient of opposite orientation, causing the magnetization of the spin to realign and recover the signal, commonly known as the echo. The time between excitation and maximum echo is referred to as T_E. A common concept is to sample the signal while applying the second gradient to acquire a range of spatial frequencies. This technique is known as frequency encoding (FE).

In this 1D case, the Fourier-transformed signal relates to the spin density $\rho_S(x)$ as follows

$$S(t) = \int \rho_S(x) \exp\left(i\phi_x(x,t)\right) \mathrm{d}x. \tag{4.7}$$

Considering the temporal dependency in terms of the spatial frequency as in equation 4.6, the signal $S(k_x)$ results in

$$S(k_x) = \int \rho_S(x) \exp\left(-i2\pi k_x x\right) \mathrm{d}x. \tag{4.8}$$

It becomes apparent that the signal $S(k_x)$ and the spin density $\rho_S(x)$ are a

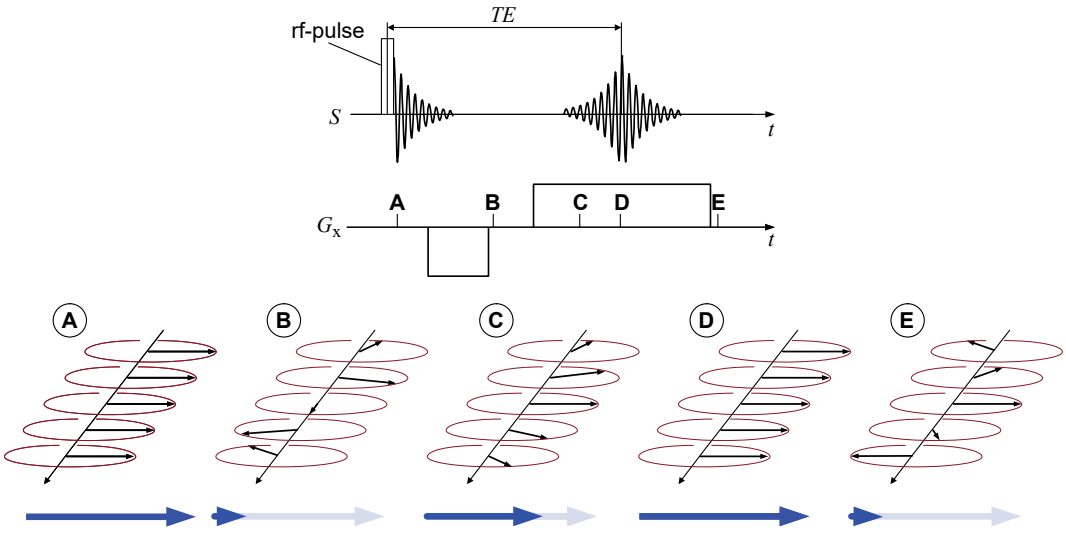

Figure 4.3.: Principle of GRE imaging with an illustration of the spins bulk magnetization at different spatial positions after excitation (**A**), after the first dephasing gradient, (**B**), and when the recall gradient is applied (**C**-**E**). The latter causes the spins to rephase (**C**), resulting in the maximum echo at the center of the gradient (**D**). Afterward, the spins dephase again (**E**).

Fourier transform pair. The inverse Fourier transform yields the spin density:

$$\rho_S(x) = \int S(k_x) \exp\left(i2\pi k_x x\right) \mathrm{d}k. \tag{4.9}$$

Using three orthogonal magnetic field gradients $\mathrm{G} = [G_x, G_y, G_z]^2$ enables spatial sensitivity of the signal in all three dimensions. The emitted signal $S(\boldsymbol{k})$ of the excited volume V than results in

$$S(\boldsymbol{k}) = \int_V \boldsymbol{x}\rho(\boldsymbol{x}) \exp\left(-i2\pi\boldsymbol{k}\boldsymbol{x}\right) \mathrm{d}V \tag{4.10}$$

The matrix of spatial frequencies sampled in an MRI measurement is defined by the desired spatial resolution $\mathrm{d}x_i$ in the respective direction and the size Δx_i of the volume of interest. The first depends on the range of spatial frequency $\Delta k_i = |k_{i,\max}| + |k_{i,\min}|$ measured in the respective direction:

$$\mathrm{d}x_i = \frac{1}{\Delta k_i} \tag{4.11}$$

This reveals that the spatial resolution is constant within a direction. The size of the measurement volume is defined by the sampling density $\mathrm{d}k_i$:

$$\Delta x_i = \frac{1}{\mathrm{d}k_i} \tag{4.12}$$

It follows that for a desired spatial data matrix of $n_x \times n_y \times n_z$, an equally sized matrix of spatial frequencies needs to be measured:

$$n_i = \frac{\Delta x_i}{\mathrm{d}x_i} = \frac{\Delta k_i}{\mathrm{d}k_i} \tag{4.13}$$

A principle scheme of a conventional Cartesian 2D GRE MRI measurement is displayed in Fig. 4.4. Multiple excitation of the volume of interest are required to sample the desired matrix of spatial frequencies $\boldsymbol{k}$ (k-space). The time between the excitation pulses is the repetition time T_R. In this Cartesian sampling, the previously introduced frequency encoding is only applied in one direction, here G_x, while other encoding strategies are used in the remaining directions. A magnetic field gradient is commonly applied during the rf-pulse to excite a distinct slap of the object in the scanner. This is known as the slice selection (SS), here applied in the z-direction. While G_z and G_x are the same for each excitation, G_y changes to move the sampled k-space line, which is known as phase encoding (PE). In a 3D measurement, the phase encoding would additionally be applied in the z direction. For fast imaging, the rf-pulse in GRE is usually designed to deflect the bulk magnetization only at small flip angles from the direction of the external field, which enables much shorter T_R

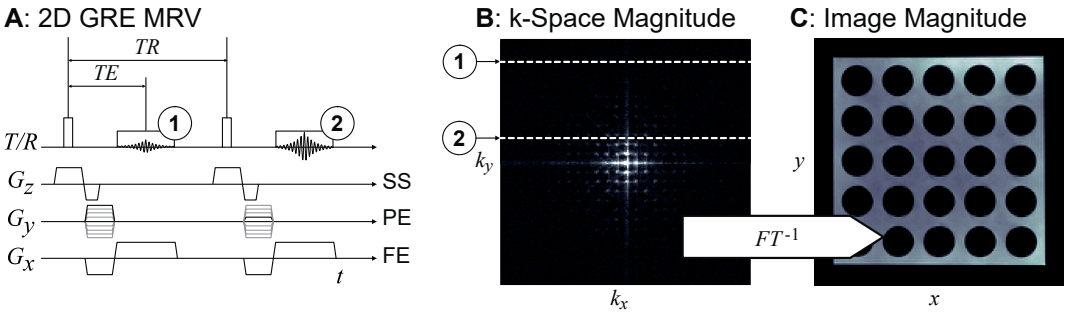

Figure 4.4.: **A**: Basic sequence design of a 2D GRE MRI measurement with slice selection (SS), phase encoding (PE) and frequency encoding (FE). ①, and ② indicate the position of the echo measured during the frequency encoding in the k-space (**B**). Applying the inverse Fourier transform (FT^{-1}) yields the data in the spatial domain, commonly referred to as the image. In **B** and **C** white indicates a high and black a low signal magnitude.

times (Haase et al., 1986).

As illustrated in Fig. 4.4**B**, the sampled signal results in a 2D k-space matrix. It becomes apparent that in the center of the matrix, the highest signal intensities are captured, as this holds the echo from the rephasing of the magnetization in the frequency encoding, and lower phase encoding gradients are applied. In contrast, the intensities are low for the outer edges, for which stronger magnetic field gradients are required. However, these data points have a higher spatial sensitivity, thus, providing the information on the fine details of the measured structure needed to get a high resolution in the measurement data. The transformed signal $S(\boldsymbol{x})$ is complex with the real part S_R and the imaginary part S_I. Its magnitude

$$|S(\boldsymbol{x})| = \sqrt{S_R(\boldsymbol{x})^2 + iS_I(\boldsymbol{x})^2} \tag{4.14}$$

yields the signal intensity distribution, which depends on the spins density but also on the T_1 and T_2^* relaxation of different tissue in the ROI. Additionally, the phase angle Φ

$$\Phi(\boldsymbol{x}) = \angle(\boldsymbol{x}) = \arctan\left(\frac{S_I(\boldsymbol{x})}{S_R(\boldsymbol{x})}\right) \tag{4.15}$$

can be utilized to encode further quantities, which is of great interest for velocity-sensitive MRI.

Conventionally, multiple receiver coils are used for the data acquisition, whose signals must be combined in the post-processing. Roemer et al. (1990) found that optimal results are obtained when the coil signals are weighted with their local sensitivity to obtain the combined signal S

$$S(\boldsymbol{x}) = \sum_{k=1}^{n} {}^k p(\boldsymbol{x})^k S(\boldsymbol{x}). \tag{4.16}$$

Here, ${}^kS$ is the signal from the kth coil of the n receiver coils with the local sensitivity ${}^kp$. However, this combination requires knowledge of the local sensitivity of each coil. Since the signal itself is an estimate of the this sensitivity, Roemer et al. (1990) proposed the sum-of-squares (SOS) combination as a straightforward estimator of p. In this approach, the complex signal S_k from the kth of the n coils is weighted with its conjugated value S_k^* before summing all coil signals

$$|S(\boldsymbol{x})| = \sqrt{\sum_{k=1}^{n} {}^kS(\boldsymbol{x}){}^kS(\boldsymbol{x})^*}. \tag{4.17}$$

Since multiplying a complex number by its conjugate complex yields a real number, this only yields the magnitude of the signal. The phase angle Φ_j is obtained by the complex angle $\angle$ of the summed signals:

$$\Phi(\boldsymbol{x}) = \angle \sum_{k=1}^{n} {}^kS(\boldsymbol{x}) \tag{4.18}$$

Besides the SOS approach, several methods exist to include more accurate estimates of the coil sensitivities. These are favorable to improve the SNR and to use the additional information of the coil positions to reduce the number of required phase encoding steps, referred to as parallel imaging. Early methods separated into algorithms that use the measured coil sensitivity, such as the sensitivity encoding (SENSE) proposed by Pruessmann et al. (1999), or performed an autocalibration, such as the approach for generalized autocalibrating partial parallel acquisition (GRAPPA) suggested by Griswold et al. (2002). A more recent approach is eigenvalue approach to autocalibrating parallel MRI (ESPIRIT)(Uecker et al., 2014) that claims to combine the advantages of both methods and has been used in a previous turbulence quantification in turbulent flows (Schmidt et al., 2021b).

4.2. Velocity Measurement

The common principle in MRV to conduct velocity sensitive measurements is PC MRI that was first presented by Moran (1982). Two decades later, Markl et al. (2003) proposed a method to perform 3D velocity measurements that are sensitive in all three spatial directions and phase locked for a phase-averaged acquisition of periodic flow in the human heart. Due to its temporal dimension, the method is known as 4D Flow. The approach has quickly gained interest in applications outside of the medical field, one of the earliest studies being measurements in a turbine blade cooling system by Elkins et al. (2003). In the past decades, MRV in technical flows often used imaging routines built on the 4D Flow sequence design, even though most studies investigated stationary

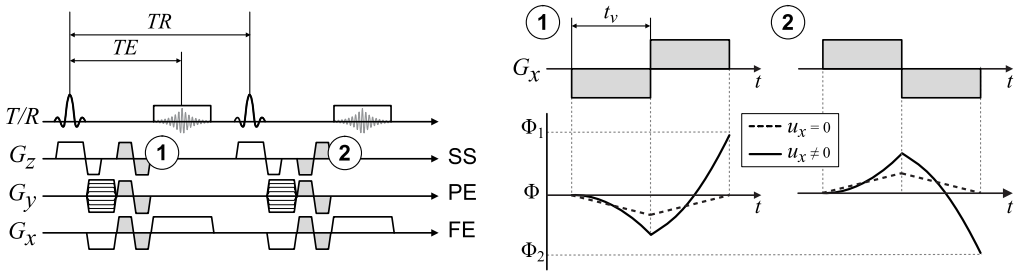

Figure 4.5.: Basic sequence design of a 2D GRE PC MRI measurement. (1) and (2) indicate the bipolar gradients that are visualized with an optimized waveform on the right side. Additionally, the effect of these gradients on the phase angle of a static spin (solid line) and a moving spin (dotted line) is illustrated.

flows (3D) without the need for phase-averaged (4D) measurements.

In general, PC MRI exploits the linear dependency of phase dispersion arising from motion to the velocity of the spins. In moving tissue, the spatial position $\boldsymbol{x}$ of a spin does not only depend on its initial position $\boldsymbol{x_0}$ but also on the velocity $\boldsymbol{u}$, the acceleration $\boldsymbol{a}$ and all higher orders of motion:

$$\boldsymbol{x}(t) = \boldsymbol{x}_0 + \boldsymbol{u} \cdot t + \frac{1}{2}\boldsymbol{a} \cdot t^2 + ... \tag{4.19}$$

For the phase angle Φ in equation 4.5 this results in:

$$\Phi(\boldsymbol{x}) = \Phi_0 + \gamma \boldsymbol{x}_0 \underbrace{\int \boldsymbol{G}(t)\mathrm{d}t}_{\boldsymbol{m_0}} + \gamma \boldsymbol{u} \underbrace{\int \boldsymbol{G}(t)t\mathrm{d}t}_{\boldsymbol{m_1}} + \gamma \frac{\boldsymbol{a}}{2} \underbrace{\int \boldsymbol{G}(t)t^2\mathrm{d}t}_{\boldsymbol{m_2}} + ... \tag{4.20}$$

$\vec{m}_n = \{m_{n,x}, m_{n,y}, m_{n,z}\}^T$ are the magnetic moments associated with the corresponding nth order of motion.

A fundamental assumption of the velocity measurement is that the acceleration $\boldsymbol{a}$ and all higher orders of motion are negligibly small. Which then results in the following:

$$\Phi(\boldsymbol{x}) = \Phi_0 + \gamma \boldsymbol{x}_0 \boldsymbol{m}_0 + \gamma \boldsymbol{u} \boldsymbol{m}_1 \tag{4.21}$$

In PC MRI, a bipolar gradient is added to the MRI sequence for which $\boldsymbol{m}_1 \neq 0$ and $\boldsymbol{m}_0 = 0$ to generate a distinct phase angle variation of moving spins. To extract the phase contribution from all other encoding gradients, the measurement is repeated with changed velocity sensitivity, for example, by simply reversing the bipolar gradient. The difference in the phase angles from both measurements holds the phase angle arising from the spin's motion.

This concept of PC MRI is illustrated in Fig. 4.5. The sequence shown on the left (**A**) illustrates the implementation of the velocity-sensitive gradients (gray) in the GRE sequence. On the right side, the effect of the bipolar gradients is illustrated using an optimized gradient waveform without ramps. The phase

difference of the moving spins then yields:

$$\Delta\Phi_x(\boldsymbol{x}) = \Phi_1(\boldsymbol{x}) - \Phi_2(\boldsymbol{x}) = \gamma u_x(\boldsymbol{x}) m_1^{enc} \tag{4.22}$$

here m_1^{enc} is the velocity encoding of the measurement, which is defined by the strength and duration $2t_v$ of the bipolar gradients:

$$m_1^{enc} = \int^{2t_v} G_{x,1}(t)t\mathrm{d}t - \int^{2t_v} G_{x,2}(t)t\mathrm{d}t \tag{4.23}$$

Commonly, m_1^{enc} is set to obtain a phase difference of $\pm\pi$ for the highest absolute velocity v_{enc}

$$v_{enc} = \frac{\pi}{\gamma m_1^{enc}}. \tag{4.24}$$

Velocities higher than the v_{enc} will result in a phase aliasing. Alternatively to $\boldsymbol{m}_1$, the sensitivity of the measurement towards velocity is often considered by $\boldsymbol{k}_v$

$$\boldsymbol{k}_v = \gamma \boldsymbol{m}_1. \tag{4.25}$$

The velocity $u_x(\boldsymbol{x})$ is now obtained from

$$u_x(\boldsymbol{x}) = \frac{\Delta\Phi_x(\boldsymbol{x})}{\gamma m_1^{enc}} = \frac{\Delta\Phi_x(\boldsymbol{x})}{\pi} v_{enc} \tag{4.26}$$

At least two further measurements are required to capture all three components of the velocity vector, in which the bipolar gradient is changed analogously in the other two gradient axis. The first measurement is then considered the reference measurement that yields $\Phi_{ref}(\boldsymbol{x})$, and the other three measurements are velocity-sensitive in the i-th direction. The resulting phase differences $\Delta\Phi_i(\boldsymbol{x})$

$$\Delta\Phi_i(\boldsymbol{x}) = \Phi_{\mathrm{ref}}(\boldsymbol{x}) - \Phi_i(\boldsymbol{x}) = \gamma u_i(\boldsymbol{x}) m_1^{enc} \tag{4.27}$$

than yield all three components of the velocity vector

$$u_i(\boldsymbol{x}) = \frac{\Delta\Phi_i(\boldsymbol{x}) v_{enc}}{\pi}. \tag{4.28}$$

This encoding scheme is called 4-point encoding (Pelc et al., 1991).

4.3. Turbulence Quantification

Turbulence measurements using MRV share the same measurement principle as diffusion-weighted MRI and rely on the phase dispersion that arises from

velocity variations inside the voxel. The dephasing of the spins within the voxels results in a signal attenuation that can be related to the intensity of the velocity fluctuation. Kuethe (1989) introduced a method to quantify this so-called turbulent diffusion from an MRI measurement, and Gao and Gore (1991) derived a more theoretical expression that includes the complex statistics of turbulent flows from a Lagrangian point of view. In the following, their approach will be derived by considering velocity sensitivity and motion occurring in a single direction. The bipolar gradient considered here has an idealized shape with the strength G and the duration $2t_v$, resulting in a phase angle of the jth fluid element to be

$$\Phi_j = -\gamma G \int_0^{t_v} \left[x(t+t_v) - x(t)\right] dt \tag{4.29}$$

The ensemble average of the spins phase angles $\langle \Phi_j^2 \rangle$ then yields

$$\langle \Phi_j^2 \rangle = \gamma^2 G^2 \int_0^{t_v} \int_0^{t_v} \langle \left[x(t_1+t_v) - x(t_1)\right] \left[x(t_2+t_v) - x(t_2)\right] \rangle \mathrm{d}t_1 \mathrm{d}t_2 \tag{4.30}$$

Gao and Gore (1991) then considered the temporal Lagrangian autocorrelation function, similar as introduced in section 3.4 for a Gaussian velocity distribution

$$R(t) = \exp\left(\frac{-|t|}{T_L}\right). \tag{4.31}$$

with the Lagrangian integral timescale T_L to interpret the ensemble average $\langle \left[x(t_1+t_v) - x(t_1)\right] \left[x(t_2+t_v) - x(t_2)\right]$. From this, they reveal a general expression of the correlation between the signal of a velocity-sensitive measurement S to the signal without phase dispersion S_0:

$$S = S_0 \exp\left(\gamma^2 G^2 \langle u'^2 \rangle T_L \left[\frac{2}{3} t_v^3 - 2 t_v T_L^2 + T_L^3 (3 - 4 e^{-t_v/T_L} + e^{-2t_v/T_L}\right]\right) \tag{4.32}$$

Gao and Gore (1991) conclude that the signal intensity of a velocity-sensitive measurement relates to two characteristic parameters of turbulent flows: the Lagrangian integral time scale T_L and the variance of the velocity fluctuation $\langle u'^2 \rangle$. However, if T_L is much larger than t_v this expression can be simplified to:

$$S = S_0 \exp\left(-\frac{\langle u'^2 \rangle \gamma^2 G^2 t_v^4}{2}\right) \tag{4.33}$$

Rearranging this equation yields a linear dependency between $\ln(|S|/|S_0|)$ and the strength of the bipolar gradient G:

$$\ln\left(\frac{S}{S_0}\right) = \frac{1}{2} \langle u'^2 \rangle \gamma^2 G^2 t_v^4 \tag{4.34}$$

Thus, they proposed to perform several measurements with changed strength G of the bipolar gradient to find the slope p of this linear dependency and used that to calculate $\langle u'^2 \rangle$:

$$\langle u'^2 \rangle = -2\frac{p}{\gamma^2 t_v^4} \tag{4.35}$$

In a following study, Gatenby and Gore (1994) demonstrated this approach in a stenosis at Reynolds numbers 1340 and 2680 using 17 different velocity sensitivities to acquire the turbulence intensity. Kuethe and Gao (1995) compared the results of the approach to data from hot wire anemometry and other methods to quantify the turbulence from MRI measurements in a fully turbulent pipe flow at Reynolds numbers 12 000 and 55 000.

A decade later, Dyverfeldt et al. (2006) described a generalized mathematical expression to quantify the turbulence intensity from a PC MRI measurement. They considered the signal $S(k_v)$ of a voxel with the spin velocity distribution $s(u)$ at the velocity sensitivity k_v to be:

$$S(k_v) = C \int_{-\infty}^{\infty} s(u) \exp\left(-\mathrm{i} k_v u\right) \mathrm{d}u. \tag{4.36}$$

C is a scaling factor that will be eliminated later. They assumed the velocity distribution $s(u)$ within a voxel to be Gaussian distributed with the standard deviation σ:

$$s(u) = \frac{1}{\sigma\sqrt{2\pi}} \exp\left(-\frac{1}{2\sigma^2}(\langle u \rangle - u)^2\right) \tag{4.37}$$

equation 4.36 transforms to:

$$S(k_v) = C \exp\left(-\frac{\sigma^2 k_v^2}{2} - \mathrm{i}\langle u \rangle k_v\right). \tag{4.38}$$

If now considering the correlation between two measurements with changed velocity sensitivity $k_{v,1} \neq k_{v,2}$ to eliminate the effects that are not affected by the first gradient moment, they found that:

$$S(k_{v,1}) = S(k_{v,2}) \exp\left(-\frac{\sigma^2(k_{v,1}^2 - k_{v,2}^2)}{2} - \mathrm{i}\langle u \rangle (k_{v,1} - k_{v,2})\right) \tag{4.39}$$

As σ is in the real part of the magnitude of this expression and the authors recommend performing one of the measurements with $k_v = 0$ to improve the accuracy in the presence of noise, equation 4.39 results in:

$$|S(k_v)| = |S_0| \exp\left(-\frac{\sigma^2 k_{v,1}^2}{2}\right) \tag{4.40}$$

Assuming the velocity fluctuations as an ergodic process, in which the spatial, temporal, and ensemble average are similar, the variance of the intra-voxel

fluctuations σ^2 equals the autocovariance of the ensemble-averaged velocity $\langle u'^2 \rangle$ in equation 4.33 (Dyverfeldt et al., 2009).

More importantly, Dyverfeldt et al. (2006) suggested that according to equation 4.36, the signal from a voxel and its velocity distribution are a Fourier transform pair. It follows that for a Gaussian distributed velocity, the dependency of signal intensity on the velocity sensitivity is also Gaussian distributed. In contrast to the previously discussed approach by Gao and Gore (1991), the approach by Dyverfeldt et al. (2006) enables to calculate the standard deviation of the velocity u from only two measurements with $k_{v,1} \neq 0$ and $k_{v_2} = 0$ by fitting the measured signal intensity to a Gaussian distribution.

The different approaches of Gao and Gore (1991) and Dyverfeldt et al. (2006) are illustrated in Fig. 4.6. Both assume a Gaussian velocity distribution, which is shown in the left graph. In the approach of Gao and Gore (1991), several measurements with changed velocity sensitivities k_v are required to find the slope of the linear fit. The approach of Dyverfeldt et al. (2006) requires only a velocity compensated ($k_v = 0$) and a velocity sensitive measurement. The optimal k_v to choose for the measurements results in a signal attenuation of $|S|/|S_0| = 0.6$.

As a result, a conventional PC MRI measurement sensitive in all three spatial directions and for which the reference measurement is acquired with $\boldsymbol{k}_v = 0$ allows calculating the normal stresses of the RST, which was demonstrated in follow up studies by Dyverfeldt et al. (2008, 2009).

Elkins et al. (2009) extended the measurements of turbulence based on the approach of Gao and Gore (1991) by simultaneously applying velocity encoding gradients in two spatial directions with the velocity sensitivity $\sqrt{2}k_v$ which then

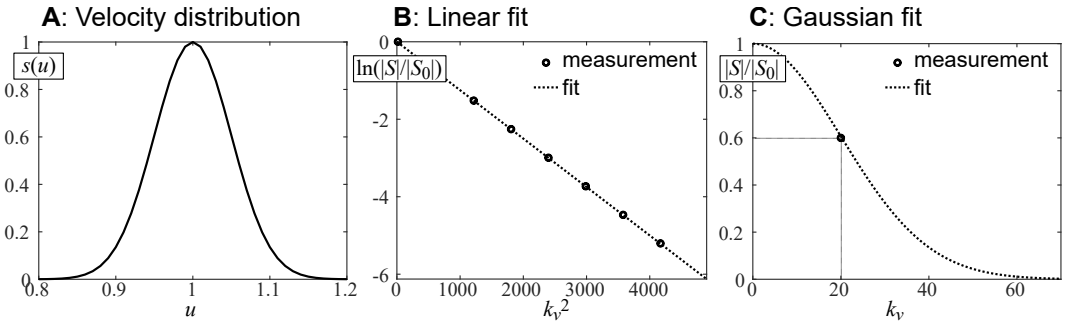

Figure 4.6.: Comparison of different approaches to find the standard deviation of a Gaussian distributed velocity (**A**). Gao and Gore (1991) acquired several measurements with changed velocity sensitivity k_v to find the slope of a linear fit in the measurement values (**B**). Dyverfeldt et al. (2006) made use of the Fourier transform pair and proposed to use a conventional PC MRI measurement and perform a Gaussian fit.

yields

$$\sigma_{i+j}^2 = \left\langle \frac{\left(u_i' + u_j'\right)^2}{2} \right\rangle = \frac{\langle u_i'^2 \rangle}{2} + \langle u_i' u_j' \rangle + \frac{\langle u_j'^2 \rangle}{2}. \tag{4.41}$$

Thus, extending a conventional PC MRI approach to six velocity-sensitive and one reference measurement enables to quantify the six Reynolds stresses. This encoding scheme is illustrated in Fig. 4.7**A**. A shortcoming of this approach is the high uncertainty in the Reynolds shear stresses as they are calculated from the fit of four measurements. In the study of Elkins et al. (2009) this led to a low quantitative agreement between the acquired Reynolds shear stresses using MRV and the reference data from PIV measurements.

To improve the acquisition of the entire RST, Haraldsson et al. (2018) used an extended motion encoding, initially designed for diffusion tensor imaging (Hasan et al., 2001), but a similar encoding had also been used to quantify the mean velocity vector (Zwart and Pipe, 2013), as it provides better SNR. The six-directional icosahedral flow encoding (ICOSA6) is performed as follows:

$$\boldsymbol{k_v} = \gamma m_1^{enc} \begin{Bmatrix} 0 & 0 & 0 \\ -1/\sqrt{(1+\psi^2)} & 0 & \psi/\sqrt{(1+\psi^2)} \\ 1/\sqrt{(1+\psi^2)} & 0 & \psi/\sqrt{(1+\psi^2)} \\ -\psi/\sqrt{(1+\psi^2)} & 1/\sqrt{(1+\psi^2)} & 0 \\ -\psi/\sqrt{(1+\psi^2)} & -1/\sqrt{(1+\psi^2)} & 0 \\ 0 & \psi/\sqrt{(1+\psi^2)} & 1/\sqrt{(1+\psi^2)} \\ 0 & -\psi/\sqrt{(1+\psi^2)} & 1/\sqrt{(1+\psi^2)} \end{Bmatrix} \tag{4.42}$$

with $\psi = (1+\sqrt{(5)}/2)$. The first row is the reference measurement followed by six velocity-sensitive measurements. The encoding is illustrated in Fig. 4.7**B**.

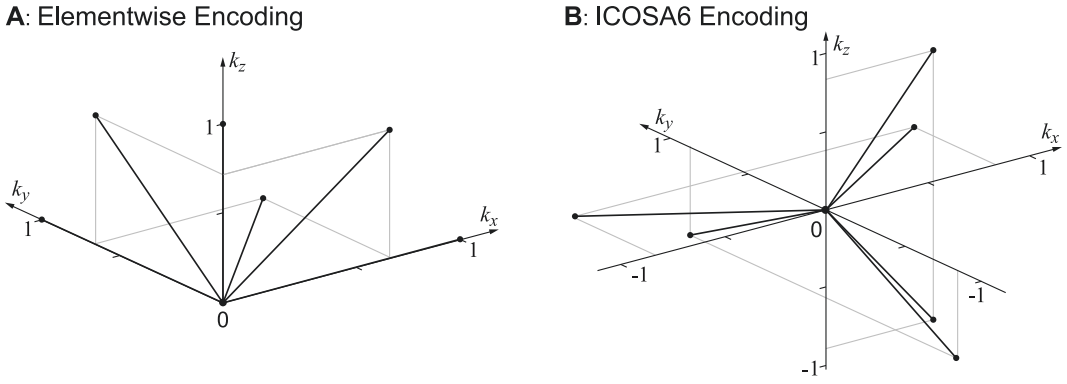

Figure 4.7.: Different concepts of the six velocity-sensitive encodings $\boldsymbol{k_v}$ and the reference measurement $\boldsymbol{k_v} = 0$ to obtain all six components of the Reynolds Stress Tensor. **A**: Element-wise encoding as proposed in Elkins and Alley (2007), and **B**: ICOSA6 encoding from diffusion-weighted imaging as proposed by Haraldsson et al. (2018) and Zwart and Pipe (2013).

The comparison to the encoding scheme as used by Elkins et al. (2009) reveals that lower $k_{v,i}$ in each encoding direction are required to reach the same velocity sensitivity in the measurement.

The RST $\tau_{i,j}$ is then obtained from (Haraldsson et al., 2018):

$$k_{i,v}\tau_{i,j}k_{j,v} = -2\ln\frac{S(k_v)}{S(0)}. \tag{4.43}$$

In a first study of Reynolds stress tensor measurements using MRV at the MRI Flow Lab, ICOSA6 encoding was used to quantify the flow in a periodic hill channel (Schmidt et al., 2020). In the flow field formed downstream of the hill, the turbulence intensity strongly varies in space. Thus, repeated measurements with various velocity sensitivities were acquired to increase the dynamic range of the acquisition.

Figure 4.8 illustrates this imaging concept for three velocity distributions $s(u)$ with different standard deviations. In a measurement, each velocity distribution would occur in a different voxel. The graph on the right shows the signal attenuation depending on the velocity sensitivity k_v and the Gaussian fit for the three considered cases based on equation 4.40. Additionally, the optimal signal attenuation $|S|/|S_0| = 0.6$ is highlighted, which is further discussed in chapter 5.2. This demonstrates that a k_v encoding suitable to perfectly capture one of the considered velocity distributions is not optimal for the others. Thus, ICOSA6 encoding with multiple velocity sensitivities as described in Schmidt et al. (2020) was identified as the most suitable method for the intended measurements in this thesis.

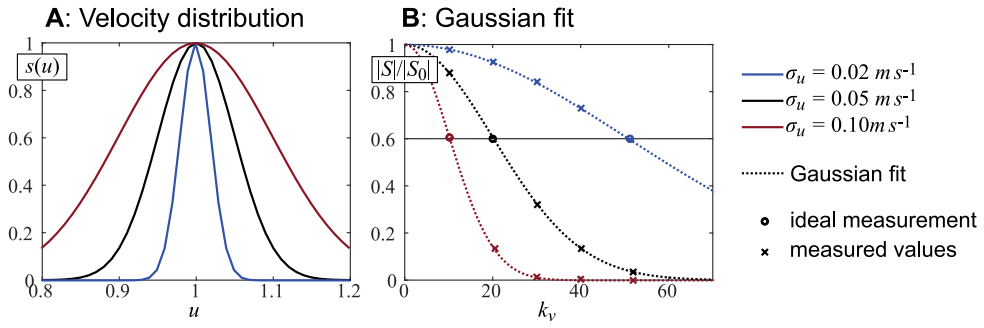

Figure 4.8.: Illustration of the concept of RST measurements with PC MRI with multiple velocity sensitivities to improve the dynamic range of the measurement. **A** shows different velocity distributions $s(u)$ which would refer to different voxels in the ROI. **B** illustrates the corresponding relative signal attenuation $|S|/|S_0|$ acquired at five velocity sensitivities k_v. The dotted line yields the Gaussian fit between the data points. The circles indicate the k_v values for which the optimal signal attenuation is reached.

5. Magnetic Resonance Velocimetry in Turbulent Flows

This chapter focuses on the peculiarities when investigating turbulent flows using MRV. First, the limitations of the measurement methods regarding the spatial and temporal resolution and the materials used inside the measurement system are discussed, followed by an analysis of random errors arising from noise and turbulent motion. More importantly, the moving fluid creates some systematic errors that must be attended to meet the stringent requirements of CFD-grade experiments. Finally, the chapter closes with a summary of imaging routines favorable for MRV data acquisition with low effect of errors.

5.1. General Limitations

The imaging concept used in MRV requires a homogeneous external magnetic field and fast-switching magnetic field gradients to measure the spatial frequency from the ROI. Thus, the achievable temporal resolution mainly depends on the available strength and slew rate of the magnetic field gradient. In recent MRV studies in technical flow systems performed on medical whole-body MRI systems similar to this study, the measurements are limited to time-averaged or phase-locked measurements. However, in the field of process engineering, applications of MRV towards time-resolved measurements to quantify transient effects in turbulent flows have been reported, for example by Tayler et al. (2011).

The imaging modulus used in MRV results in errors related to the Fourier transform and the finite size of the captured k-space matrix. The limited number of spatial frequencies creates Gibbs ringing effects at sharp edges. Theoretically, infinite spatial frequencies are required to capture them correctly. Additionally, the size of the captured k-space sets the spatial resolution, which is uniform within the encoded direction. As a result, voxels covering the boundary between different tissue, e.g., fluid and surrounding, suffer from partial volume effects. Their signal magnitude is an average of both materials, but the phase angle only holds the information of signal-providing tissue. Thus, near-wall velocities can be captured correctly, but the segmentation of the fluid-

filled volume from the background is biased. However, the ability of MRV to provide data from regions including different materials enables unique insights, for example, to porous structures (Bruschewski et al., 2021a) or particle-laden flows (Hogendoorn et al., 2022). In these applications, it is not required to resolve the entire structure to get information on the spatially averaged velocity distribution and the fraction of the fluid phase.

The MRI system used in this study provides an external magnetic field of 3 T, while the available magnetic gradient strength is $40\,\mathrm{mT\,m^{-1}}$. This illustrates that the described imaging method builds on minor changes in the local magnetic field strength, making it sensitive to any imperfections in the magnetic field. Several effects can cause these imperfections, illustrated in Fig. 5.1 and discussed in the following. All these effects are considered systematic errors.

First, the electromagnetic coils create magnetic field gradients with a limited linearity that decreases with rising distance to the scanner's isocenter. The non-linearity results in phase shifts which cause distortions at the outer edges of the FOV. The MRI system used in this study provides a spherical volume of approximately 200 mm diameter in which these errors can be neglected.

Additionally, the fast switching of the magnetic field gradients induces currents in conductive components of the MRI, also known as eddy currents. They create a magnetic field superimposing the desired gradient field. Consequently, the actual gradient waveform differs from the indented one, resulting in image artifacts and signal loss. The effect becomes especially significant if conducting material is used near the measurement region. In technical systems, phase offsets arising from eddy currents are robustly compensated by repeating the measurement without flow.

Lastly, not only the conductivity but also the magnetic susceptibility of tissue used inside or in the proximity of the ROI can cause distortions in the measurement results. The susceptibility describes the magnetization of a material in a strong magnetic field. At the boundary of tissues with a change

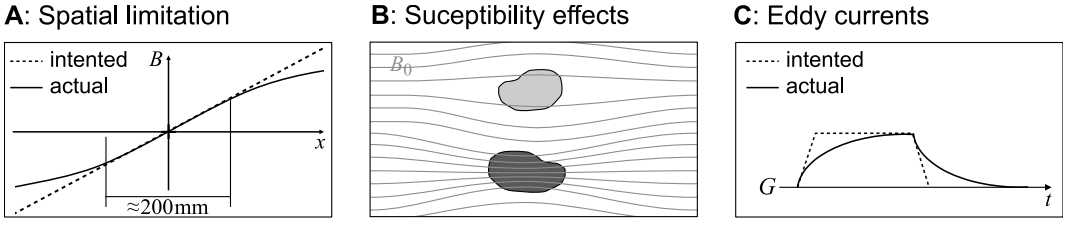

Figure 5.1.: Causes of magnetic field imperfections in MRI. **A**: Spatial limitation of the linearity of the magnetic gradients (G). **B**: Susceptibility differences of the materials used inside the ROI. **C**: Induced eddy currents due to fast switching magnetic field gradients result in undesired gradient waveform.

in susceptibility, this causes phase variation, which appears as distortions in the measurement data. Wapler et al. (2014) measured the susceptibility of different materials relevant for engineering studies to identify which have a similar susceptibility to the one of water, thus being the most suitable for experimental setups.

None of the recent studies using MRV in technical studies similar as intended in this study have reported one of these error sources to bias the measurements within the spatial and temporal limitations significantly. The experimental setups are commonly manufactured from materials with a similar susceptibility as the flow medium and without any metal parts to avoid an increasing effect of eddy currents. However, it was also demonstrated by Bruschewski et al. (2021c) that measurements with functional parts of copper are also feasible.

5.2. Random Errors

This section considers two measurement errors having a similar effect on the measurement results but different origins. First, measurement noise arises in the receiver chain and from dielectric and inductive losses in the sample (Hoult and Lauterbur, 1979). The noise N is assumed to occur normal distributed with zero mean and standard deviation in both real N_R and imaginary part N_I independently (Henkelman, 1985):

$$N(\boldsymbol{x}) = N_R(\boldsymbol{x}) + iN_I(\boldsymbol{x}). \tag{5.1}$$

Second, in the measurement of turbulent flows, the changes in the flow field due to the turbulent fluctuations results in changing phase deviations in the measured signal between the readouts. The effect is comparable to motion artifacts in medical imaging commonly associated with periodic motion from breathing or blood flow. Due to the periodic or continuous motion, this error appears as image ghosts spread over the FOV in the phase encoding direction (Wood and Henkelman, 1985). The nature of turbulence results in random displacements of the signal distributions from each readout, causing the motion artifacts to appear as a more noise-like effect in the phase encoding direction. The effects of these errors are illustrated in Fig. 5.2 showing the signal magnitude of a 2D velocity compensated measurement with flow in the out-of-plane direction.

In general, the SNR depends on the timing parameters and the strength of the excitation pulse, thus the flip angle. The relaxation time (T_1) limits the minimum required repetition time T_R to recover most of the magnetization for each new excitation. In contrast, T_2^* limits the maximum echo time T_E

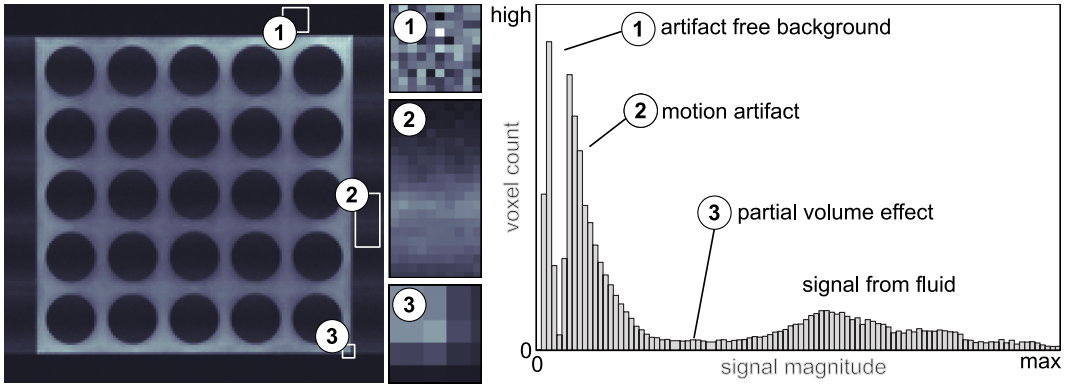

Figure 5.2.: The effect of random noise and turbulence-induced motion artifacts on the image magnitude. The magnitude distribution on the right side highlights regions of the image that yields the characteristic distribution of signal magnitude. The cutouts show (1) noise in the artifact-free background, (2) background with motion artifact, and (3) partial volume effects at the boundary of fluid and the channels wall. The contrast is adjusted for better visibility of the artifacts.

to get a measurable signal. In medical imaging, the timing of these parameters is used to generate contrasts between different tissue types. If only the flow medium generates the MR signal when considering single-phase flows in technical models, the focus is on realizing small T_R and T_E times to keep the acquisition time short and reduce the influence of measurement errors.

Considering a measurement where the timing parameters are set, the SNR mainly depends on the voxel volume V, the bandwidth per pixel bw, the number of measurement repetitions n_R, and the number of phase encoding steps n_{PE} (McRobbie et al., 2006):

$$SNR \propto V \frac{\sqrt{n_{PE} n_R}}{\sqrt{bw}} \tag{5.2}$$

The phase encoding direction is particularly susceptible to motion artifacts as the time scales to capture all phase encoding steps are in the order of seconds. Within this time, the fluid elements randomly change their velocity, causing frequency shifts that result in image fragments appearing in the wrong position. Thus, a higher number of phase encoding steps is not beneficial to reduce these artifacts, but increasing the number of averages significantly improves the signal quality (Stadler et al., 2007).

Different approaches exist to quantify the influence of noise, either by estimating it from the artifact-free background of the data (Constantinides et al., 1997) or using more complicated approaches based in the local statistics in the ROI (Aja-Fernandez et al., 2008). Bruschewski et al. (2016a) compared several of these approaches and found that ROI based estimators yield more reliable results for the uncertainty in MRV velocity measurements in the presence of

motion artifacts. Based on the findings from this study, the dual acquisition approach had been regularly used to quantify the uncertainty $\tilde{\sigma}_u$ in MRV mean velocity measurements (Bruschewski et al., 2016a):

$$\tilde{\sigma}_u = \frac{V_{enc}}{\pi}\sqrt{\frac{\left\langle \left({}^1\Delta\Phi\left(\boldsymbol{x}_{ROI}\right) - {}^2\Delta\Phi\left(\boldsymbol{x}_{ROI}\right)\right)^2\right\rangle}{2}} \tag{5.3}$$

Here ${}^1\Delta\Phi(\boldsymbol{x}_{ROI})$ and ${}^2\Delta\Phi(\boldsymbol{x}_{ROI})$ are the phase angles in the ROI of two measurement averages. The ROI refers only to the fluid-filled volume segmented from the background using the signal magnitude. The velocity measurements are commonly averaged several times to get a reasonable SNR and minimize the influence of turbulent motion artifacts. For each average, the velocity field is reconstructed to quantify the uncertainty.

In turbulence acquisition, however, a similar approach is not feasible as the least-square-fit strongly depends on the noise level in the data. As the signal magnitude needs to be considered in MRV turbulence quantification, the complex noise manifests as a non-zero offset, resulting in a limit of measurable velocity standard deviation σ_N at the velocity sensitivity k_v as pointed out by Dyverfeldt et al. (2009):

$$\sigma_N = \sqrt{\frac{2\ln\left(|S_0|/|S_N|\right)}{k_v^2}}. \tag{5.4}$$

Here, $|S_N|$ is the mean magnitude of noise. Thus, any σ higher than this value would result in a signal magnitude in the same order as the noise. To measure these fluctuations, k_v would need to be reduced. On the other hand, at low k_v, small velocity fluctuations will not lead to a notable signal loss between $|S_0|$ and $|S|$. Figure 5.3 illustrates the effect of noise on a generic signal with an SNR of 20. At inhomogeneous flow conditions, it is favorable to increase the dynamic range of the measurement by using different k_v, as emphasized

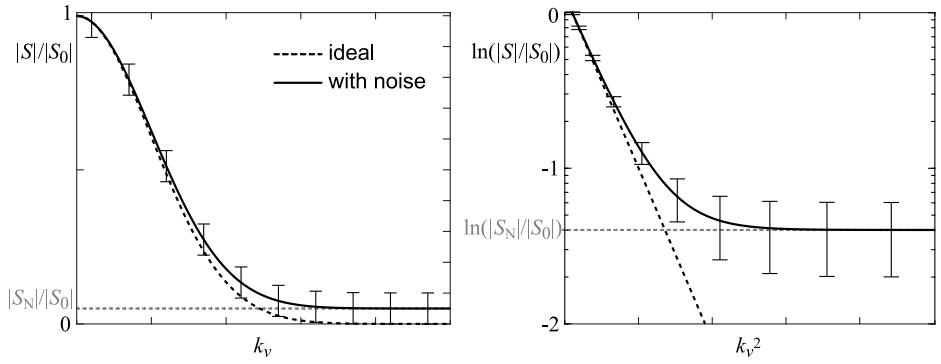

Figure 5.3.: The theoretical signal at an SNR of 20 yields the upper limit of k_v to obtain a signal higher than the noise level and the poor signal loss at small k_v values as described by Dyverfeldt et al. (2009).

by Dyverfeldt et al. (2009) and demonstrated by Schmidt et al. (2021b) using 12 m_1^{enc} encodings to capture the flow field in a periodic hill channel. To avoid data points with signal magnitudes close to the noise level to bias the data, previous studies either set a threshold (Gatenby and Gore, 1994; Schmidt et al., 2021b) or performed a weighted-least-square fit (Dyverfeldt et al., 2009) to lower the sensitivity against noise in the fit of the data points.

Additionally, Elkins et al. (2009) suggested quantifying the uncertainty $\tilde{\sigma}_{i,j}$ arising from the noise and the motion artifacts by estimating the effect of random errors from the background, which yields

$$\tilde{\sigma}_{i,j} = \frac{\sqrt{\left(\frac{|N_0|}{|S_0|}\right)^2 + \left(\frac{|N|}{|S|}\right)^2}}{\sigma_{i,j} k_v^2}. \tag{5.5}$$

Here $|N|$ and $|N_0|$ are the estimated magnitude from the background of velocity-sensitive and velocity-compensated measurements, respectively.

5.3. Flow Induced Errors

The encoding process in MRI takes a finite duration, and the encoding gradients are commonly not played out simultaneously. Both cause bias in the data acquisition if motion occurs in the ROI. The duration of the individual gradients results in a smearing of the signal from moving spins. The possibilities to reduce this error are limited as the maximum available gradient strength and gradient slew rate are restricted. Additionally, the time delays within the different encoding gradients cause more severe errors.

Figure 5.4**A** shows the effect of the encoding process in a conventional 2D GRE PC MRI sequence considering the path of a fluid particle moving through a contraction. The time of encoding is approximated as the center of each encoding process, and black dots indicate the position of the fluid particle at this time. Additionally, the gray highlighting of the path indicates the duration of each encoding event. At the end of the encoding process, the time stamps account for the same point in k-space but include information from different positions. In the presence of accelerated motion, the effect of this non-instantaneously encoding becomes apparent as distortions in the measured geometry and flow field. The effect is referred to as displacement or misregistration and has been observed and described as early as PC MRI has been developed (Larson 3rd et al., 1991; Frayne and Rutt, 1993).

The strength of this systematic error depends on the relation between temporal scales of motion and the duration of the encoding process. Part **B** of Fig. 5.4 shows the measured velocity in the contraction using conventional PC

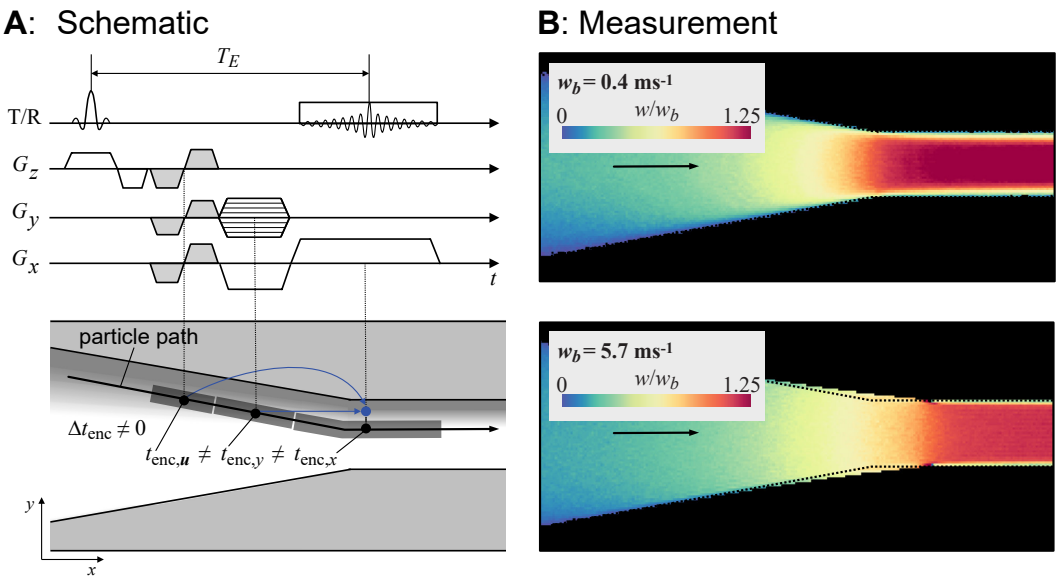

Figure 5.4.: Misregistrations illustrated for a conventional Cartesian PC MRI considering a particle moving through a continuous contraction (**A**). Black dots symbolize the encoding time, assumed at the center of the encoding gradients. The blue dot and arrows indicate the misalignment of the velocity and the spatial encoding. **B** shows the effect of misregistration at different velocities in measurements using conventional Cartesian PC MRI. The dotted line indicates the real geometry.

MRI at two different flow rates. At low bulk velocity w_b, no significant effects of misregistration are apparent. The velocities increase along the contraction, and the highest values coincide with the narrowest part of the geometry. If the flow rate increases significantly, the captured geometry strongly deviates, and the flow acceleration is captured too far downstream.

Figure 5.4A also reveals that the frequency-encoded direction is most susceptible to displacement since the delay between velocity and spatial encoding is the largest. For the slice selection and the phase encoding direction, the gradients are commonly combined to optimize the encoding process, which is discussed in more detail in section 5.5.

Detailed knowledge of the timing and shape of the encoding gradients and the flow field is required to calculate the systematic error from the encoding process exactly. A conservative estimate of the displacement Δx_{mis} can be made using T_E and a the bulk velocity u_{bulk} (Elkins et al., 2009; John et al., 2020):

$$\Delta x_{mis} = T_E \cdot u_{bulk} \tag{5.6}$$

This equation also yields two basic options to lower the effect of misregistration by either decreasing u_{bulk} or T_E.

5.4. Bias from Flow Characteristics

In the previous chapter, the principles of velocity-sensitive MRI were discussed. It was mentioned that the imaging technique presupposes characteristics of the velocity distribution inside a voxel to quantify the velocity and the RST:

- Phase variations due to higher orders of motion are negligible
- Normal distribution of the velocity inside the voxel
- Scales of turbulent motion

Whereas the velocity quantification is only affected by the first and the latter assumption, all three aspects must be considered when quantifying the RST.

As MRV is predestined to capture the flow in complex geometries, these structures naturally force changes in the velocity. The temporal derivative of the velocity are referred to as higher orders of motion, including acceleration ($a = \mathrm{d}^2x/\mathrm{d}t^2 = \mathrm{d}u/\mathrm{d}t$), jerk ($j = \mathrm{d}^3x/\mathrm{d}t^3 = \mathrm{d}a/\mathrm{d}t$) and so on. They can also be considered by mean values and fluctuations that cause additional phase dispersion in velocity-sensitive measurements. In terms of velocity measurement, the contribution of the higher order of motion can be eliminated by additional gradients. However, this extends the duration of encoding process, which promotes misregistration.

Since the magnetic moments of motion $\vec{m}_n$ results

$$m_n = \int_0^{T_E} G(\boldsymbol{x}, t) t^n \mathrm{d}t \tag{5.7}$$

the additional phase deviation arising from the nth order of motion is proportional to t^n. Shortening the encoding process reduces the integration time, which is simultaneously beneficial for minimizing misregistration artifacts.

Additionally, the velocity variations in regions of shear or boundary layers result in considerable variations of the mean velocity inside a voxel. The velocity distribution then deviates from a normal distribution. Dyverfeldt et al. (2009) derived an estimator to compensate for this effect in the measured standard deviation of the velocity σ_{meas} to obtain the purged standard deviation of the fluctuations σ:

$$\sigma = \sqrt{\sigma_{meas}^2 - \frac{2}{k_v^2} ln \left(\frac{|S_0|}{|S_{mvv}(k_v)|} \right)} \tag{5.8}$$

whereby they assumed that the signal loss arising from the mean velocity variation resulted from linear velocity gradients, which are calculated as

$$\frac{|S_0|}{|S_{mvv}(k_v)|} = |\mathrm{sinc} \left(\frac{g k_v}{2} \right)| \tag{5.9}$$

with g being the linear velocity difference over the voxel.

Lastly, the temporal scales of turbulent motion are relevant for the reliability of the results. On the one hand, the temporal averaging must cover a long enough duration to include the largest scales of turbulent motion and ensure that the measurements converge against the mean flow parameters. One the other hand, the duration of the velocity encoding needs to be significantly faster than the integral time scale to avoid a strong temporal filtering in MRV RST quantification.

However, without knowing the frequency spectrum of the turbulent fluctuations, the exact determination of time scales is cumbersome. In general, the time scales can be estimated by a characteristic length scale of the eddies l_E and a characteristic velocity scale u_E

$$T_E = \frac{l_E}{u_E}. \tag{5.10}$$

Gao and Gore (1991) considered their approach to be used for turbulence quantification measurements in a blood vessel. They estimated the Lagrangian integral time scale from the time scale of the mean eddy length, which they suggested to be one-third of a vessel's diameter. Furthermore, they used the turbulence intensity as the characteristic velocity scale of these eddies. They assumed the turbulence intensity to be 3 % to 6 % of the mean velocity.

Elkins et al. (2009) assumed that l_E corresponds to the size of the largest eddies. They suggested that this size is restricted by the width of the shear layer generated behind the backward-facing step they investigated. Furthermore, they considered two velocity scales to quantify the integral time scale: The measured axial velocity in the shear layer, which they referred to as the eddy advection velocity, and the calculated standard deviation.

Alternatively, the integral time scale can be calculated from another experimental measurement method, as done by Schmidt et al. (2021b), or from a scale-resolving numerical simulation. As additional measurements and numerical simulations are time-consuming, reference data from previous studies in fuel assembly models may also serve as an estimator.

5.5. Imaging Methods

Various imaging methods exist to capture the flow in non-medical applications, and the most favorable imaging technique strongly depends on the considered flow (Gladden and Sederman, 2013). Single-shot imaging methods such as echo-planar imaging (EPI) or spiral imaging enable very short acquisition times. The latter is illustrated in Fig. 5.5**A** and provides short T_E as the

readout starts directly in the center of the k-space. On the downside, complex image reconstruction is required, and the method is sensitive to magnetic field imperfections. EPI is more robust due to the Cartesian sampling, but it requires longer T_E, which promotes motion-induced errors. The advantage of these methods, in general, is that they allow capturing transient effects, for example, as demonstrated in the study by Tayler et al. (2011).

Very short T_E at low sensitivity to systematic errors are achieved in pure phase encoded single point imaging (SPI) methods such as SYNC SPI proposed by Bruschewski et al. (2019). In this imaging method, no magnetic field gradients are applied during readout, and the encoding events are aligned, making the method the most robust against motion-induced errors. John et al. (2020) showed that SYNC SPI allows capturing flow velocities up to $12\,\mathrm{m\,s^{-1}}$ on conventional medical whole-body MRI systems without significant effects of misregistration. On the downside, measurements are time-consuming as each k-space point is encoded individually. The general layout of SYNC SPI is illustrated in Fig. 5.5**C**.

Conventional GRE imaging as introduced in the previous chapter, holds a compromise of robust imaging, short echo times, and feasible acquisition times. PC MRI is commonly based on low flip angle excitation, known as fast low-angle shot (FLASH) (Haase et al., 1986), to enable short T_R. The multiple excitations required to capture the entire k-space commonly limit this imaging technique to time-averaged acquisition. For comparison with the previously mentioned methods, the GRE PCMRI is illustrated in Fig. 5.5**B**.

Besides the general principle of imaging, sensitivity to systematic errors also depends on the design of the gradient waveform. Different concepts on the combination of the spatial encoding and the velocity-sensitive gradients in the

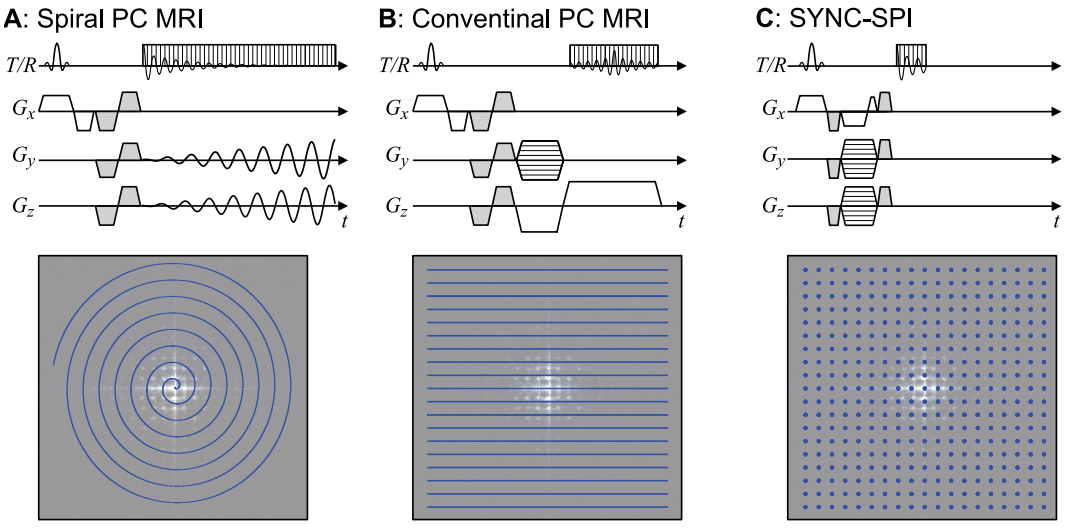

Figure 5.5.: Variety of imaging methods in PC MRI from single shot imaging (**A**), to line-wise sampling (**B**) and single point imaging (**C**).

slice- and phase-encoding direction are discussed by Schmidt et al. (2020). The encoding for fast gradients (FAST), based on the gradient waveform proposed by Bernstein et al. (1992), calculates the gradients to achieve the lowest possible encoding duration and T_E. On the downside, the changing gradients in each acquisition of different k-space lines result in a changed m_1 in the phase-encoded (PE) directions, intensifying the effect of spatial misregistration. On the contrary, the encoding with controlled displacement (ECHO) proposed by Nishimura et al. (1991) designs the gradient waveform to get the same m_1^{PE} and m_1^{SS} in each k-space line to reduce the effect of misregistration.

A schematic comparison of both methods in 3D PC MRI based on Schmidt et al. (2020) is illustrated in Fig. 5.6. The times t_{PE}, t_{SS}, and t_{FE} refer to the encoding times of phase, slice, and frequency encoding, respectively. In the case of FAST, these encoding times are assigned to different times. For the ECHO encoding, the extended gradients in the phase and slice encoding direction result in a controlled shift of moving particles along the velocity direction which equals an alignment of the encoding times. On the downside, the extended gradients increase the sensitivity to higher orders of motion, and displacement in the velocity field is still apparent (Schmidt et al., 2020).

Further reduction of T_E in conventional PC MRI is possible using an asymmetric readout (Schmalbrock et al., 1990; Richardson et al., 1994). The dephasing gradient in the readout direction is reduced so that the echo appears before the center of the readout gradient. Figure 5.7**A** and **B** illustrate the Cartesian PC MRI with symmetric and asymmetric readout, respectively.

An alternative sampling method that can have an asymmetric readout is a radial acquisition, illustrated in Fig. 5.7**C**. In contrast to Cartesian sampling with asymmetric readout, the radial trajectories enable symmetrical coverage of k-space while retaining the short TE time. Furthermore, the sampling can be inherently under-sampled to accelerate the acquisition (Markl et al., 2012; Untenberger et al., 2016), and is more robust against (turbulent) motion

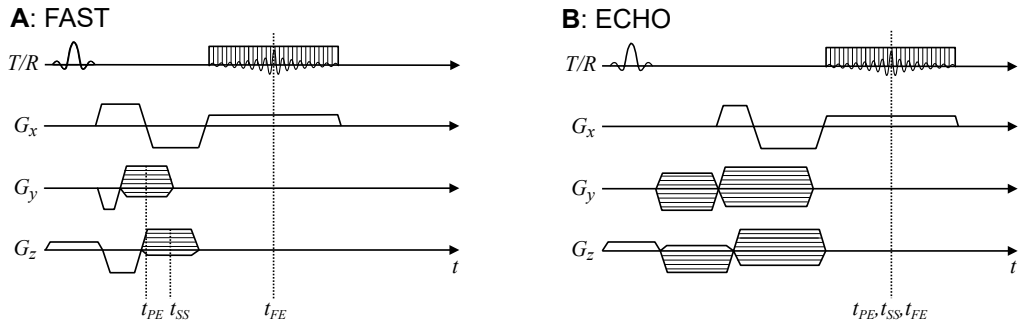

Figure 5.6.: Comparison of methods to combine velocity and spatial encoding gradients in 3D PC MRI based on the designs presented by Schmidt et al. (2020). The encoding times t_{PE}, t_{SE} and t_{RO} yield the sensitivity to spatial misregistration.

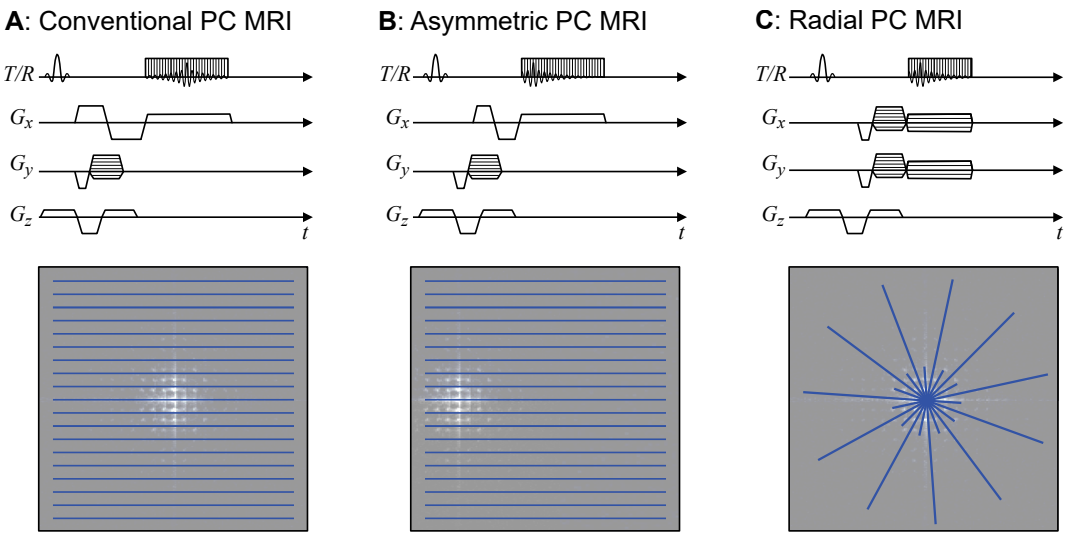

Figure 5.7.: Reduction of T_E using an asymmetric readout in Cartesian (**B**) or radial sampling (**C**) compared to the conventional PC MRI (**A**).

artifacts (McRobbie et al., 2006). However, radial sampling requires a more complex image reconstruction and is sensitive to magnetic field imperfections such as gradient delays.

Part III.

Measurements

The following part describes the measurements performed in an MRV compatible replica of the OECD/NEA-KAERI benchmark. The study aims to provide data at similar boundary conditions as in the initial benchmark exercise to allow for a comparison with the LDV reference study and to demonstrate the value of MRV measurements for such applications. The mean velocity vectors and the 6C RST are acquired in 2D slices at $z/d_h = 1$ and $z/d_h = 4$ downstream of the spacer grid. Whereby d_h is the hydraulic diameter as introduced in equation 3.2. These positions were also captured by Chang et al. (2014) and were found by Lee et al. (2014) to be the most interesting measurement positions out of the four distances considered in the LDV measurements. They constitute that at $z/d_h = 1$ the flow shows the most vigorous vortices while at $z/d_h = 4$ a certain decay of turbulence intensity is observed. Furthermore, 2D measurements are performed upstream of the spacer grid, which could serve as an inlet flow field for CFD calculations similar to the benchmark study.

An outstanding capability of MRV is the ability to capture the entire flow field in an 3D region of interest. Therefore, it can provide significantly more data than LDV, even inside the spacer grid where optical measurements are cumbersome. Measurements of the mean velocity vector are performed in a volume reaching from shortly upstream of the spacer grid up to approximately $z/d_h = 10$ downstream. This enables to visualize and quantify the development and decay of flow structures formed by the different designs of the mixing vanes but also allows for a more comprehensive validation of CFD methods. A more detailed discussion on the limited reliability of the assessment of numerical results based on only 1D profiles or limited 2D data is provided in the following part IV in which the MRV data is compared to the reference data from the OECD/KAERI-NEA benchmark.

Measurements are performed using conventional Cartesian PC MRI similar as in the previous studies by Schmidt et al. (2021b), Bruschewski et al. (2021b), and John et al. (2022). These earlier works demonstrated the potential of MRV but also identified the significant impact of systematic errors, particularly in the RST measurements. These established imaging routines are the starting point for commissioning the MRI-compatible fuel assembly model with the swirl-type spacer grid, presented in chapter 8. Two substantial aspects are identified to improve the results of a final measurement campaign with the split-type spacer grid presented in chapter 9. On the one hand, more precise identification of the required m_1^{enc} is needed following the findings of Dyverfeldt et al. (2009). On the other hand, the PC MRI is changed to FAST encoding and asymmetric readout to reduce the effect of flow-induced errors. These attempts focus, in particular, on the accuracy of the RST measurements. Nonetheless, the velocity measurement similarly benefits from improving the

imaging method and thus increases its reliability in assessing CFD methods.

Additionally, the reconstruction of RST is improved compared to the earlier studies by considering the suggestions from Dyverfeldt et al. (2009). The effect of random errors in the 3D Gaussian fit is controlled using a weighted-least square fit instead of a simple threshold. Furthermore, the correction of mean velocity variance is included.

The following chapters will first focus on the experimental setup and the facility used for the MRV measurements before analyzing the boundary conditions under which the data is acquired, including the measurements of the upstream flow field. Chapter 8 and chapter 9 focus on the measurements with the swirl-type and the split-type spacer grid, respectively. Particular emphasis is placed on the effect of systematic errors in these measurements to identify the reliability of the results and the effect of the improvements in the imaging method. The findings are summarized and discussed in the final chapter of this part before the measurements are compared to the reference data of the benchmark study in part IV.

6. Methods and Facilities

The experimental setup and the flow conditions follow the LDV experiments performed by Chang et al. (2014) to provide comparable but more comprehensive experimental data for the OECD/NEA-KAERI benchmark. However, some adjustments were required to make the setup compatible with the MRI system and take advantage of the capabilities of MRV. The design of the experiment is addressed in the first part of this chapter, followed by information on the machinery and equipment used for the measurements and to control the boundary conditions. Finally, the processing of the measurement data is summarized.

6.1. Fuel Assembly Model

In planning the experimental setup, possible sources of errors affecting the MRV measurements have been taken into account. First, the fuel assembly used in this study is scaled up by factor 2.1 compared to realistic dimensions, but this is smaller than in the LDV experiments by Chang et al. (2014). The size of the setup is a compromise between relative resolution, flow rate, and bulk velocity. The latter was kept below $2\,\mathrm{m\,s^{-1}}$ to limit the effect of flow-induced errors. As a result, the channel has a height of 134 mm, holding 5x5 rods of 20 mm. The hydraulic diameter d_h in this fuel assembly model is 19.81 mm, and the pitch P is 26.71 mm. Both are used to scale the dimensions for comparability with the initial study on this benchmark. It is assumed that the arrangement of the fuel assembly restricts the convective length l_0 of turbulent motion to 17.71 mm, which equals the free length on the diagonal

Table 6.1.: Characteristic dimensions of the fuel assembly

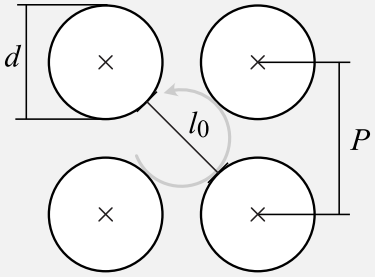

channel height		134.00 mm
channel length		3000.00 mm
rod diameter	d	20.00 mm
pitch	P	26.71 mm
hydraulic diameter	d_h	19.18 mm
convective length scale	l_0	17.71 mm

between two rods. The dimensions are summarized in Tab. 6.1.

Furthermore, errors due to susceptibility differences in the used materials are minimized by using materials with a similar susceptibility as water in the proximity of the measurement region. The study of Wapler et al. (2014) served as a reference to select the materials. The rods are made from grounded Polyoxymethylene (POM), the channel holding the fuel assembly model is made from acrylic glass (PMMA), and the spacer grids are additively manufactured using Polyamide (PA12). The manufacturing of the spacer grid is realized using Multi Jet Fusion (HP Development Company, L.P., 2018), which provides a mean surface roughness of $R_a = 11\,\mu\text{m}$ and a standard accuracy in the dimensions of the spacer of 0.3 %. As the surface roughness was believed to cause significant differences in the flow field in a previous study (Bruschewski et al., 2021b), chemical smoothing was applied to the spacer grids holding the mixing vanes to reduce the mean roughness to $R_a = 1\,\mu\text{m}$.

The materials suitable for MRI-compatible setups are plastics that are less rigid than the stainless steel components used in the benchmark study. Additional support spacer grids are installed, and the distance to the mixing grid is reduced to $22d_h$ to prevent the rods from bending and vibrating. An advantage of MRV is that the measurement region is significantly further upstream of the channel's end, minimizing the impact of the outlet design on the acquired flow field. In the LDV experiments, measurements were taken 10 mm (approx. $0.4d_h$) upstream of the outlet manifold to provide optical access. NEA (2013) annotate that some participants raised concerns about the effect of this outlet condition on the measurement results. The arrangement of the fuel assembly model for the MRV measurements is illustrated in Fig. 6.1.

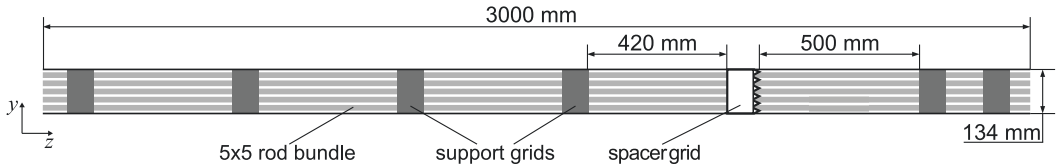

Figure 6.1.: Arrangement of support grids and spacer grid with mixing vanes in the MRV setup.

6.2. Experimental Setup

MRV measurements were performed at the MRI Flow Lab at the University of Rostock, which holds a conventional 3 T whole-body MRI scanner (Magnetom Trio, Siemens Healthcare GmbH, Erlangen, Germany). The gradient system enables a maximum gradient strength of $40\,\text{mT}\,\text{m}^{-1}$, which is reached at a slew rate of $200\,\text{mT}\,\text{m}^{-1}\,\text{s}^{-1}$. The MRI machine is located in the examination room

that is screened against electromagnetic noise and interference. A piping system is guided through waveguides in the walls to connect the pumps outside of the examination room with the fuel assembly model.

The entire setup is depicted in Fig. 6.2. Two parallel switched radial pumps provide the flow medium from a 1000 L water reservoir. The flow medium is purified water with $1\,\mathrm{g\,kg^{-1}}$ copper sulfate ($CuSO_4$) added to enable a faster magnetization of the flow medium and a lower T_R. A filter is installed upstream of the test section to avoid any dirt or foreign particles to disturb the measurements or lead to a blockage in the fuel assembly model. The filter is followed by a flow straightener, a 2 m straight pipe, and a settling chamber to destroy unwanted flow structures in the inlet flow field.

The flow rate is supervised by an ultrasonic flow meter (systec Controls, Puchheim, Germany) at an uncertainty of 1 %. The temperature is captured shortly downstream of the pumps and at the inlet of the water reservoir to verify that the fluid temperature does not significantly change when passing the flow circuit and the fuel assembly model. The pressure is acquired downstream of both pumps (Labom, Hude, Germany) and is monitored at several positions along the flow circuit with analog gauges. The position of the instruments is

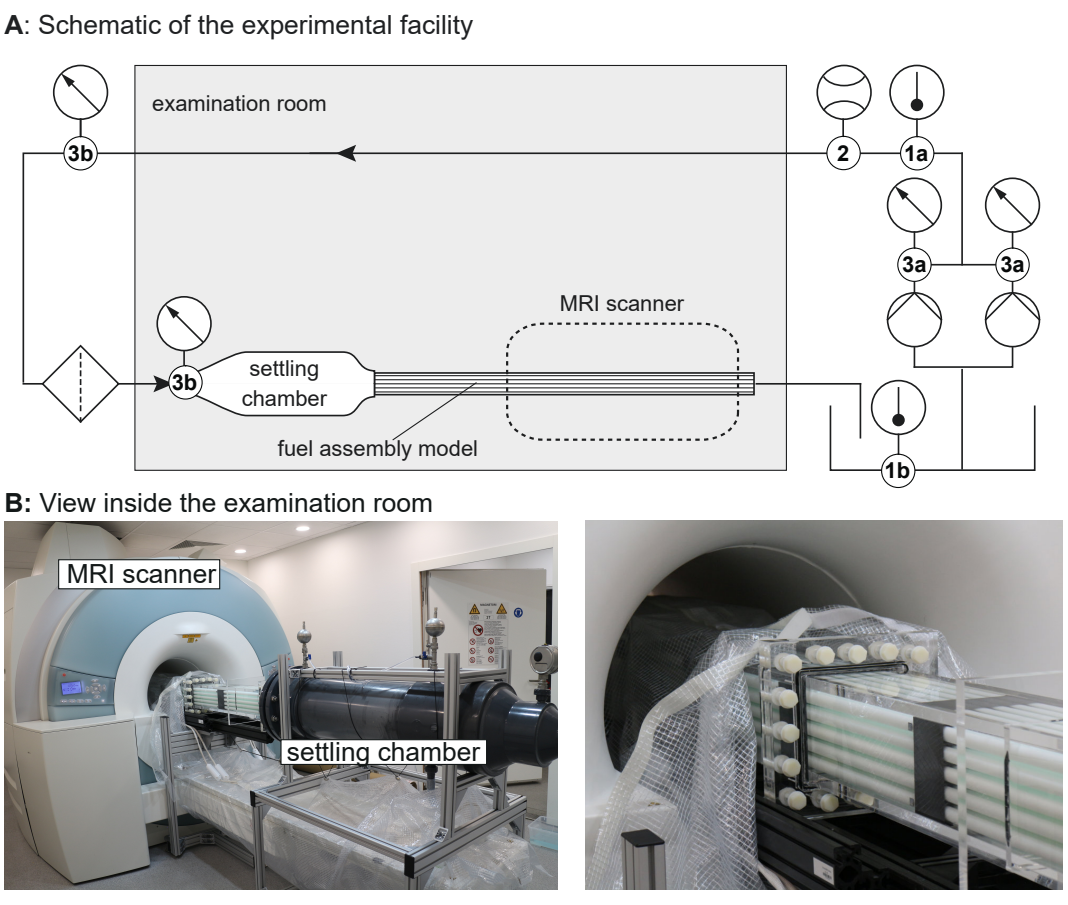

Figure 6.2.: Experimental setup

Table 6.2.: Instruments to monitor the flow conditions. Numbers indicate the positions as shown in Fig. 6.2.

Instrument		Range	Accuracy
Temperature θ			
(1a)	Labom, MiniTherm, GA2700 with PA2430	0 °C to 100 °C	0.25 °C
(1b)	H-TRONIC, TS125	−55 °C to 125 °C	0.5 °C
Flow rate Q			
(2)	systec Controls, deltawaveC, XUC-FW-F21	0 L min^{-1} to 2500 L min^{-1}	1 %
Pressure p			
(3a)	Labom, COMPACT ECO, CA1110	0 bar to 6 bar	0.5 %
(3b)	Bourdon, MEX5	0 bar to 6 bar	

indicated in 6.2, and their specifications are listed in Tab. 6.2. The flow properties of the sensors (1a), (2), and (3a) were acquired using Labview (Nationsal Instruments Corp., Austin, TX, USA), while all other sensors were recorded analog.

6.3. Data Processing

For the 2D measurements, all results are processed from raw data using MATLAB (R2022a, The MathWorks Inc., Natick, Massachusetts, USA). The raw data files are read using 'rdMeas' (version 2012.06.14 for MATLAB, Auerbach, E., Center for Magnetic Resonance Research University of Minnesota, USA). The data is averaged in the frequency domain before applying the Fourier transform. The coil signals are combined with coil sensitivity maps obtained using ESPIRIT (Uecker et al., 2014). On the contrary, analysis of the 3D data is done from the images processed by the scanners software (syngo MR B17, Siemens AG, Healthcare, Germany) to use the distortion correction filter provided in the scanners software. Here, SOS is utilized to combine the coil signals. The data obtained from the scanner are the magnitude and the phase difference images, which are then averaged in the image domain.

Having performed the Fourier transform and combined the coil signals, the mean velocity components $\langle u_i(\boldsymbol{x})\rangle$ are obtained via:

$$\langle u_i(\boldsymbol{x})\rangle = \angle(S_i(\boldsymbol{x})S_0(\boldsymbol{x})^*)\frac{v_{enc}}{\pi}. \tag{6.1}$$

S_0^* is the conjugate of the complex signal of reference measurement, and S_i is the measurement sensitive to velocity in the ith direction. Phase angle offsets from induced eddy currents are removed by fitting the velocity distribution in

the measurements without flow onto second-order Legendre polynomials. The resulting velocity distribution is then subtracted from the velocity obtained in the measurement with the flow.

The accuracy of the velocity measurements is calculated by adapting the dual acquisition approach from equation 5.3 for the standard deviation of all image pairs resulting from the n repetitions of the measurement:

$$\tilde{\sigma}_{u_i} = \frac{1}{\sqrt{2n}} \cdot \sum_{k=1}^{n} \frac{2\sqrt{\langle (^{2k-1}u_i(\boldsymbol{x}_{\mathrm{ROI}}) - ^{2k}u_i.(\boldsymbol{x}_{\mathrm{ROI}}))^2 \rangle}}{n}, \tag{6.2}$$

In this calculation, only fluid-filled voxels, thus the voxels of the ROI, are included, which have been previously segmented by the signal magnitude. The uncertainty $\tilde{\sigma}$ corresponds to the 68 % confidence interval in the entire ROI. The coil sensitivity maps used to reconstruct the velocity distribution of the individual measurements are calculated from the mean data.
In 3D velocity measurements, the flow rate Q indicates systematic errors. It is calculated from the axial velocity w and the voxel's cross-section with dx and dy being the measurement resolution perpendicular to the mean flow direction z.

$$Q(z) = \mathrm{d}x\mathrm{d}y \sum_x \sum_y w(\boldsymbol{x}_{\mathrm{ROI}}) \tag{6.3}$$

Again, only the voxels in the ROI are considered. According to the conservation of mass for an incompressible fluid, the flow rate must be constant along the z-direction that aligns with the channel's axis. Thus, any deviation occurring in $Q(z)$ indicates the influence of systematic errors.

The RST is calculated by fitting the image magnitudes of all ICOSA6 encoded measurements on a three-dimensional Gaussian distribution as proposed by Schmidt et al. (2020). As random errors from noise and motion artifacts affect the measurements, an offset c in the 3D Gaussian distribution is allowed:

$$\underbrace{\frac{|S(\boldsymbol{k}_v)|}{|S_0|}}_{Y} \stackrel{!}{=} \underbrace{(1-c)\exp\left(-\frac{1}{2}\boldsymbol{k}_v^T \boldsymbol{\tau}^{-1} \boldsymbol{k}_v\right) + c}_{f(\boldsymbol{k}_v, \boldsymbol{\tau}, c)}. \tag{6.4}$$

The left term of this equation holds the measured values Y, while the right side is the fitted function $f(\boldsymbol{k}_v, \boldsymbol{\tau}, c)$.

Dyverfeldt et al. (2009) suggested a weighted least square fit to find the RST $\boldsymbol{\tau}$. They defined the weighting function W as a normal distribution with an expected value of 0.6 and a standard deviation of 0.2:

$$W_i = \exp\left(\frac{-(Y_i - 0.6)^2}{2 \cdot 0.2^2}\right). \tag{6.5}$$

As a result, the contribution of measurements stronger affected by random errors from noise and turbulent motion artifacts is limited. In each ith voxel of the ROI, the RST $\boldsymbol{\tau}$ and the offset c are optimized to find the minimum residual of the weighted sum of square of all n measured velocity sensitivities:

$$\arg\min_{\boldsymbol{\tau},c} \sum_{k=1}^{n} {}^{k}W_i \cdot ({}^{k}Y_i - f({}^{k}\boldsymbol{k}_v, \boldsymbol{\tau}, c))^2. \tag{6.6}$$

Here, ${}^{k}(...)$ indicates the metrics of the kth velocity-sensitive measurement. The initial values for $\boldsymbol{\tau}$ are found from the 1D fit of the individual encoding in the ICOSA6 encoding scheme, while the initial value for the offset c is designated as 0.05. The residuum r of this fit is

$$r = \sum_{k=1}^{n} {}^{k}W_i \cdot ({}^{k}Y_i - f({}^{k}\boldsymbol{k}_v, \boldsymbol{\tau}, c))^2. \tag{6.7}$$

The effect of random errors in the measured values Y is calculated from the estimated level of the noise and motion artifact in reference measurement S_0 and the velocity sensitive measurement S in each of the ith voxels:

$$\tilde{\sigma}_{Y,i} = \sqrt{\left(\frac{|N_0|}{|S_{0,i}|}\right)^2 + \left(\frac{|N|}{|S_i|}\right)^2}. \tag{6.8}$$

$|N_0|$ and $|N|$ are the mean magnitudes of the background of the fuel assembly model in the reference and the velocity-sensitive measurement, respectively. The background is defined as the five outer voxels at each edge of the image matrix, as illustrated in Fig. 6.3. Due to the effect of turbulence, it was not always feasible to identify the Ricardian distribution of noise, as it is described in the literature (Gudbjartsson and Patz, 1996). Therefore, the mean value of the background magnitude is used to estimate the impact of random errors, as illustrated in Fig. 6.3. The uncertainty in the final RST values is then calculated from the difference between the conventional reconstruction and a weighted least square fit, where the estimated level of noise is subtracted from the measurement values. Nonetheless, this is only a conservative approximation of the measurement uncertainty. Future efforts will be placed on more accurate quantification of the random error.

Lastly, the effect of mean velocity variance on the measurement results is investigated following the approach of Dyverfeldt et al. (2009). The velocity gradient is assumed to be linear over the voxel. For the 2D measurements, velocity gradients are calculated from the 2D mean velocity measurements to avoid errors from a misalignment of the different imaging orientations. Consequently, only the in-plane variations are considered for all three components

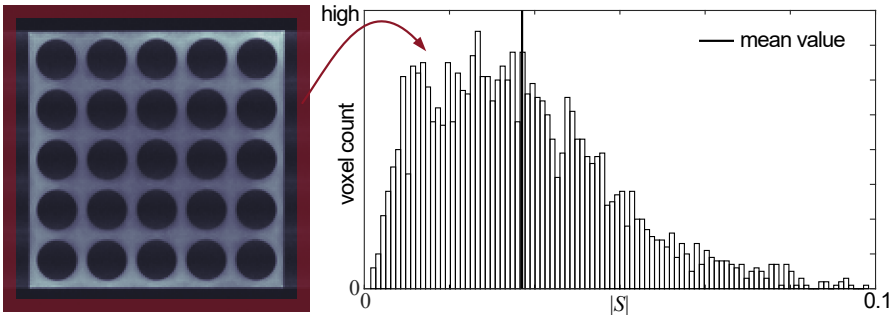

Figure 6.3.: Quantification of random noise and motion artifacts to estimate their effect on the RST quantification. The red area on the left indicates the voxels taken into account to calculate the mean signal magnitude of the background. The histogram shows the signal intensities of the selected voxels and their mean magnitude.

u_i of the mean velocity vector:

$$g_i = \sqrt{\left(\frac{\mathrm{d}u_i}{\mathrm{d}x}\right)^2 + \left(\frac{\mathrm{d}u_i}{\mathrm{d}y}\right)^2} \tag{6.9}$$

For the kth encoding of the six velocity-sensitive encoding in the ICOSA6 scheme, the effect of the velocity gradient $\boldsymbol{g} = (g_x, g_y, g_z)$ over the voxel is calculated for the specific direction of velocity sensitivity ${}^k\boldsymbol{k}_v = \langle {}^k k_{v,x}, {}^k k_{v,y}, {}^k k_{v,z} \rangle^T$ as follows

$$|\boldsymbol{g}\,{}^k\boldsymbol{k}_v| = \sqrt{(g_x \cdot {}^k k_{v,x})^2 + (g_x \cdot {}^k k_{v,y})^2 + (g_z \cdot {}^k k_{v,z})^2}. \tag{6.10}$$

From this, the relative signal magnitude $|S_{MVV}({}^k\boldsymbol{k}_v)|/|S_0|$ resulting from the mean velocity variation is calculated according to equation 5.9 and is then used to correct the measured signal before performing the weighted least square fit.

The entire post-processing of the results is realized using MATLAB (R2022a, The MathWorks Inc., Natick, Massachusetts, USA). Additionally, 3D3C results can be analyzed using the same imaging routines as numerical results. Thus, using ParaView (5.9.0-RC1, Kitware Inc., NY, USA), streamlines, vorticity, and Q-criterium are depicted.

7. Experimental Conditions

This chapter summarizes the conditions under which the measurements in chapter 8 and 9 are taken. Besides the supervision of flow rate, temperature, and pressure, an analysis of time scales of the turbulence statistics is undertaken, and the results of MRV measurements of the inlet flow field are presented.

7.1. Flow Properties

The flow properties in all measurements aimed to reach the same Reynolds number 50 250 as in the LDV reference study by Chang et al. (2014). The flow medium is purified water with $1\,\mathrm{g\,kg^{-1}}$ of $CoSO_4$ added as a contrast agent. For the swirl-type spacer, the target flow conditions were set to $\theta = 35\,^{\circ}\mathrm{C}$, resulting in a flow rate of $Q = 1150\,\mathrm{L\,min^{-1}}$ and a viscosity of $\nu = 0.723\,\mathrm{mm^2\,s^{-1}}$ (Kestin et al., 1978). In the final measurement campaign, in which the upstream flow field and the flow field behind the split-type were acquired, the target flow conditions were set to $\theta = 40\,^{\circ}\mathrm{C}$, resulting in a flow rate of $Q = 1045\,\mathrm{L\,min^{-1}}$ and a viscosity of $\nu = 0.658\,\mathrm{mm^2\,s^{-1}}$(Kestin et al., 1978). In preliminary tests, the added contrast agent did not show a measurable impact on the viscosity at $20\,^{\circ}\mathrm{C}$, which is why the viscosity of purified water is considered here.

The swirl-type spacer grid was assembled during the commissioning of the entire experimental setup, where it was found that the heating system was too slow to reach the target temperature in the available time frame, and the target Reynolds number was not met in all measurements. For the upstream and the split-type measurements, the heating was optimized, and the target conditions were reached in all measurements.

The values shown in Fig. 7.1 were acquired in four measurement cycles with the split-type spacer grid. The results indicate that the experimental conditions were reproduced reliably. In general, measurements were performed within cycles of up to 60 min not to overheat the MRI system. In the shown example, the mean flow rate deviated from the target value by up to $3\,\mathrm{L\,min^{-1}}$ on average and fluctuated about $3\,\mathrm{L\,min^{-1}}$, which is within the sensor's measurement uncertainty of 1 %, or $10.45\,\mathrm{L\,min^{-1}}$. The maximum differential pressure acquired downstream of the pumps was (0.86 ± 0.06) bar.

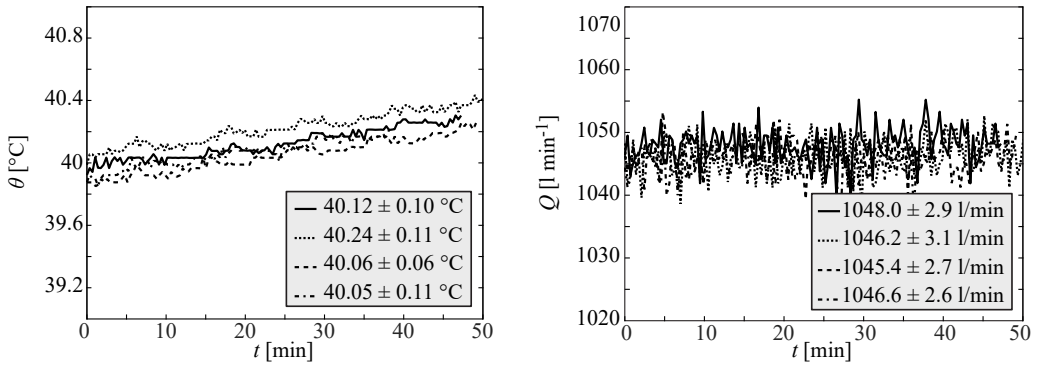

Figure 7.1.: Measured temperature and flow rate of four MRV measurement cycles in the final measurement campaign with the split type spacer.

7.2. Upstream Flow-Field

Chang et al. (2014) performed measurements corresponding to a distance of $z/d_h = 10$ upstream of the spacer grid to provide the upstream flow field to the participants of the blind benchmark exercise. For the MRV measurements, the mean velocity vector and the Reynolds stresses were captured in a 2D slice at $z/d_h = 2.3$ upstream of the spacer grid. The imaging parameters are summarized in Tab. 7.1. The data was acquired by moving the entire channel with the fuel assembly model without disassembling it to have the measurement plane in the isocenter of the MRI system. The distance between

Table 7.1.: Imaging parameters for velocity and turbulence quantification upstream of the spacer grid.

	2D velocity	**2D RST**
FOV x, y, z [mm^3]	$320 \times 160 \times 3.4$	$320 \times 160 \times 3.4$
Resolution x, y, z [mm^3]	$1.0 \times 1.0 \times 3.4$	$1.0 \times 1.0 \times 3.4$
Matrix size x, y, z	$320 \times 160 \times 3.4$	$320 \times 160 \times 3.4$
Readout direction	x	x
T_E [ms]	3.2	4.9
T_R [ms]	6.0	6.6
Flip angle [°]	15	15
Slab selective	yes	yes
Pulse Duration [µs]	800	800
Pulse BWT	2.7	2.7
Echo asymmetry	0.5	0.5
Receiver bandwith per pixel [Hz]	950	950
Encoding scheme	4-point	ICOSA6
Gradient design	FAST	FAST
Velocity encoding [m s^{-1}]	4	0.14 to 0.69
No. of velocity encodings	1	5
Averages flow on	100	100
Averages flow off	30	-
Total acquisition time [min]	8	60

the acquired FOV and the spacer grid results from the maximum available shift in the position of the receiver coils, which was limited by the supports of the channel. Measurements further upstream or without the spacer grid are also feasible but require disassembling of the fuel assembly.

Figure 7.2 depicts the measurement results of the axial velocity w, the normalized secondary flow SFI, and the turbulent kinetic energy TKE calculated from the MVV corrected RST in the four gaps between the rods and in the entire cross-section. The results yield a very regular distribution of the flow properties and a high uniformity of w and TKE within the different gaps. There are no flow characteristics apparent that are likely to impact the downstream measurements.

Upstream of the spacer grid, the flow is assumed to be fully developed with low secondary flow intensity and low turbulence level. Errors due to fluid motion can be considered negligible. The velocity measurement yields an uncertainty of 0.6 % in all three components of the velocity vector related to the

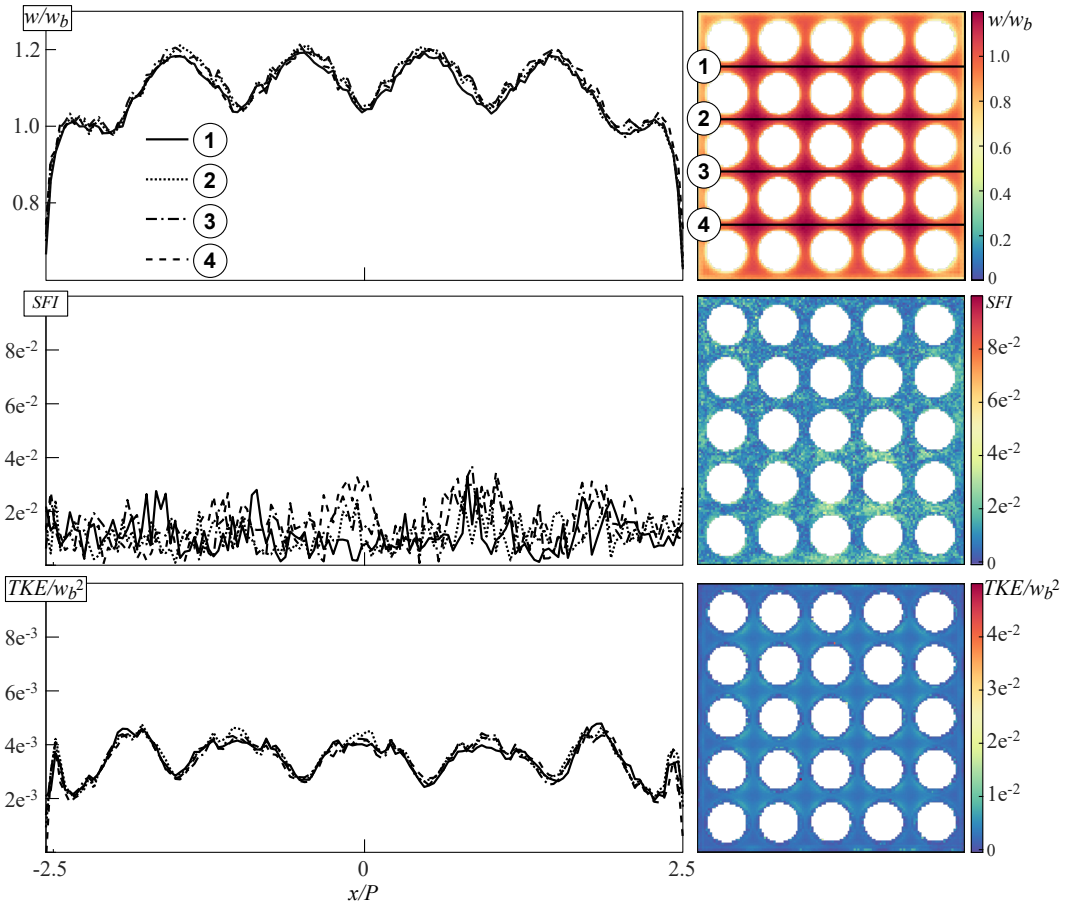

Figure 7.2.: Inlet flow conditions measured with MRV in a 2D slice at $z/d_h = 2.3$ upstream of the spacer grid. Results are shown as profiles in the four gaps between the fuel rods as indicated in the top right by numbers (1) to (4), and contour plots in the entire fluid-filled cross-section of the fuel assembly for the axial bulk velocity w_b, the secondary flow intensity SFI, and the turbulent kinetic energy TKE

bulk velocity. Calculating the flow rate from the MRV measurement yields $1022\,\mathrm{L\,min^{-1}}$, which is 2.2 % lower than the target value. This deviation is higher than the uncertainties of the flow rate sensor and the measurement accuracy. Due to the complex geometric structure inside the fuel assemblies cross-section, partial volume effects are expected to be responsible for the remaining difference. The normalized secondary flow is 1.2 % of the bulk velocity, which coincides with the combined measurement uncertainty from both lateral velocity components. The mean measured turbulence intensity is 5.3 % for the axial and 4.6 % for the lateral velocity, which is in the same range as described in the LDV reference study (Chang et al., 2014). A detailed comparison to the upstream flow field with data provided to the participants of the initial OECD/NEA-KEARI benchmark is given in 12.1.

7.3. Turbulence Statistics

The available temporal resolution of the used MRV methods and imaging system enables only time-averaged measurements of the velocity field and the Reynolds stress tensor. When imaging the flow, different time scales need to be considered to verify the significance of the experimental study. On the one hand, the measured values only represent the mean flow if the acquisition times are significantly higher than the time scales of the largest eddies. On the other hand, the velocity encoding must be fast enough to capture the effect of fluctuations in MRV RST measurements.
In the fuel assembly model, the largest eddies are assumed to occur in the center of the subchannel with the length scale l_0 and are moving with the axial bulk velocity w_b. This results in a time scale of about 10 ms for the measurements with the swirl-type spacer grid and 11 ms for the measurements with the split-type spacer grid. The deviation arises from the lowered bulk velocity in the latter measurement campaign.

A very conservative estimator of the total sampling time in MRV is only to consider the number of repetitions and the duration of the readout gradient, which is in all measurements approximately 1.1 ms. Considering this, the sampling time in all 2D measurements is at least 10 times higher, but for the 3D measurements, the statistical convergence would be questionable. However, it is also feasible to take the phase encoding step into account, as each measured spatial frequency holds information on all voxels inside the ROI. This calculation then yields that the sampling time in all measurements is at least three orders of magnitude higher than the time scales of the largest eddies, so statistical convergence is expected in all results.

For the quantification of the RST, the integral time scale of the turbulent

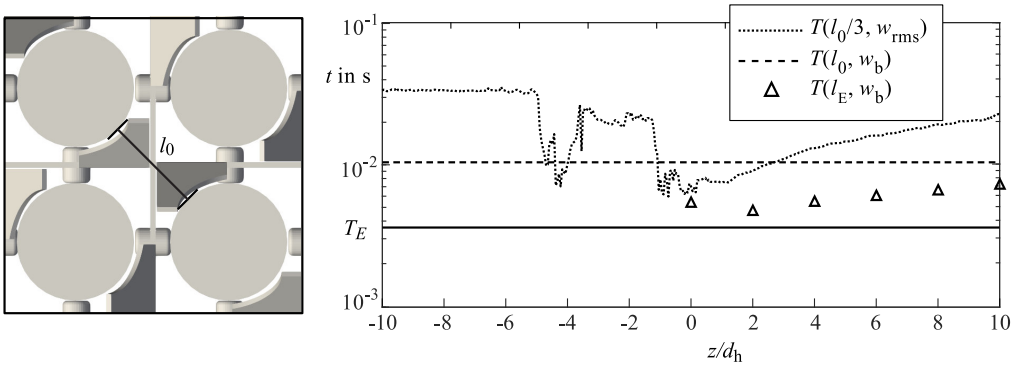

Figure 7.3.: Estimators of the integral time scale along the axial direction. The estimators are calculated from the measured axial turbulence intensity w_{rms} and the mean eddy length $l_0/3$ following Gao and Gore (1991), from the bulk velocity w_b and size of the largest eddies l_0 similar as in Elkins et al. (2009), and from integral length scales l_E obtained by Matozinhos et al. (2021) using PIV in a similar experimental setup.

fluctuations needs to be greater than the duration of the velocity encoding gradient to avoid significant temporal filtering. However, the integral time scale cannot be quantified from the time-averaged data captured by MRV, and different estimators have been used in previous studies to estimate it. Following the approach presented by Gao and Gore (1991), the integral time scale T are estimated from the turbulence intensity and the mean eddy size, which they assumed to be one-third of a vessel's diameter. For the fuel assembly, T is derived from the largest value of the axial turbulence intensity w_{rms} obtained from a measurement in a gap between two layers of rods along the channels axis (see section 9). For the length scale, one-third of the largest available space for eddy motion l_0 is considered. Elkins et al. (2009) referred in their estimation of T to the largest eddy size, which is here assumed to be l_0, and the advection velocity, which is here assumed to be the bulk velocity w_b. They also used the standard deviation of the velocity, but this estimator would result in higher integral time scales and is thus not the most conservative estimator for this analysis. Lastly, the T is estimated from the integral length scale L quantified using PIV in a fuel assembly with a split-type spacer grid by Matozinhos et al. (2021) at Reynolds number 28 000 at the center of a subchannel.

Figure 7.3 compares the different approaches to verify the relation between the time scales and velocity encoding. As the exact duration of the velocity encoding gradients is unknown, the T_E is considered a conservative estimate of the velocity encoding duration. All three estimators yield integral time scales larger than the T_E. The approaches based on the turbulence intensity w_{rms} and the reference data from another experimental study reveal increasing scales with further distance to the spacer grid. Thus, stronger spatial filtering can be expected in the proximity of the mixing vanes. The lowest integral time

scale of $T = 4.6\,\mathrm{ms}$ is obtained based on the experimental study by Matozinhos et al. (2021).

8. Swirl-Type Spacer

The initial measurement campaign in the previously described MRV-compatible replica of the OECD/NEA-KAERI benchmark were carried out with the swirl-type spacer grid installed in the fuel assembly model. The design is based on the details published by NEA (2013). In the main body of the spacer grid, each rod is supported by eight supports, four at each end of the spacer grid. Four mixing vanes angled by 35° are positioned at the downstream side in each crossing of the grid to enhance the mixing inside the subchannels. They are assembled as either right- or left-rotating, as shown in the computer aided design (CAD) illustration of the fuel assembly model in Fig. 8.1.

It should be noted that the measurements presented in the following were carried out within the first commissioning of the fuel assembly model. During this process, it became apparent that the heating rate of the flow medium was too slow to complete all measurements at the target temperature within the available timeframe. Thus, the Reynolds number was not reached entirely, which is discussed in more detail in section 8.2. Nonetheless, the obtained results can serve as a reference for simulations with adjusted boundary conditions, as demonstrated at the recent 'CFD4NRS' conference (John et al., 2023). Furthermore, experimental studies conducted on fuel rod bundles indicate that the flow field at these conditions is not significantly influenced by the Reynolds number (Qu et al., 2019).

Additionally, the data enables insights into the effect of improvements in the imaging routine when compared to the results obtained in the split-type

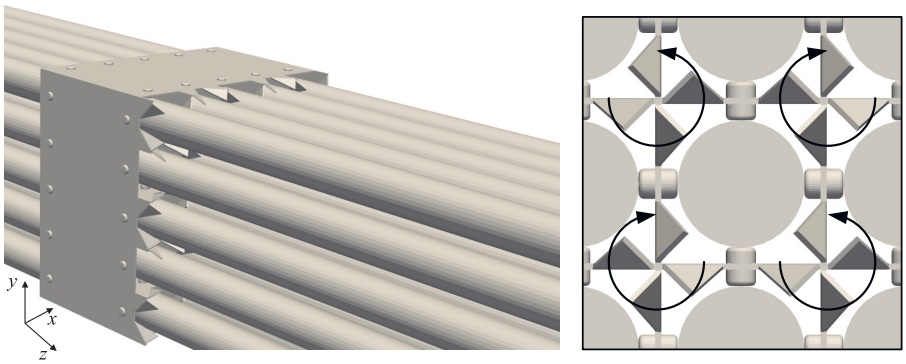

Figure 8.1.: CAD of the swirl-type spacer grid based on the details published by NEA (2013). The arrows indicate the orientation of the mixing vanes.

spacer (see chapter 9). For the latter, the imaging method was optimized as the initial measurements indicated a notable sensitivity to systematic errors in some regions of the flow.

The imaging methods validated by Schmidt et al. (2020) against LDV were used for the swirl-type spacer. The mean velocity vectors were captured in a 3D FOV reaching from shortly upstream to $z/d_h = 10$ downstream of the spacer grid. Additionally, 2D measurements similar to the positions in the initial benchmark study were performed. The Reynolds stresses were measured at the two distances that Lee et al. (2014) identified to be the most interesting.

8.1. Imaging Protocol

The imaging routine proposed by Schmidt et al. (2021b) is a Cartesian GRE PC MRI based on the 4D Flow sequence by Markl et al. (2003). To control the displacement artifacts, the gradient waveform is optimized following the ECHO encoding scheme described by Schmidt et al. (2020). The imaging parameters are presented in Tab. 8.1. In general, they were optimized to the lowest possible T_E to lower the sensitivity to flow-induced errors. The readout duration is shortened by maximizing the bandwidth, which moves

Table 8.1.: Imaging parameters for velocity and turbulence quantification in measurements with the swirl-type spacer grid.

	3D velocity	**2D velocity**	**2D RST**
FOV x, y, z [mm^3]	$216 \times 158.4 \times 432$	$320 \times 160 \times 5$	$320 \times 160 \times 5$
Resolution x, y, z [mm^3]	$0.9 \times 0.9 \times 0.9$	$1.0 \times 1.0 \times 5.0$	$1.0, 1.0, 5.0$
Matrix size x, y, z	$240 \times 176 \times 480$	$320 \times 160 \times 1$	$320 \times 160 \times 1$
Readout direction	z	x	x
T_E [ms]	3.3	3.4	3.8
T_R [ms]	6.0	5.0	5.3
Flip angle [°]	10	10	10
Slab selective	no	yes	yes
Pulse Duration [µs]	800	730	730
Pulse BWT	4.0	4.0	4.0
Echo asymmetriy	0.5	0.5	0.5
Receiver bandwith per pixel [Hz]	920	950	950
Encoding scheme	4-point	4-point	ICOSA6
Gradient design	ECHO	ECHO	ECHO
Velocity encoding [m s^{-1}]	4	4	0.31 to 4.21
No. of velocity encodings	1	1	7
Averages flow on	9	128	100
Averages flow off	1	32	-
Total acquisition time [min]	170	10	70

the echo closer to the encoding gradients. As this is disadvantageous for the SNR and to avoid significant motion artifacts from turbulent fluctuations, the measurements are averaged up to 128 times. T_R is decreased to a minimum to shorten the acquisition time. The flip angle was optimized in preliminary scans to get the highest SNR at the given timing parameters.

The mean velocity vector was captured in a 3D volume with 0.9 mm isotropic resolution covering a ROI from shortly upstream to $z/d_h = 10$ downstream of the spacer grid. Additionally, 2D measurements at 5 mm slice thickness and 1 mm in-plane resolution were taken in each of the four downstream positions as it was done in the LDV measurements by Chang et al. (2014) for the initial benchmark study. This data is also used to correct the effect of mean velocity variance in the RST measurements. It should be noted that it is also possible to calculate the velocity vectors from the ICOSA6 encoded turbulence measurements (Zwart and Pipe, 2013; Haraldsson et al., 2018). However, the velocity sensitivities optimized for the turbulence quantification require an extended T_E compared to measurement optimized for velocity quantification. Thus, acquiring the velocity in a separate measurement seemed more practical. Even though 4-point encoding yields a lower SNR, it is less time-consuming than ICOSA6, which allows for more measurement averages to reduce turbulent motion artifacts.

The v_{enc} was set to $4\,\mathrm{m\,s^{-1}}$, which is about two-fold higher than the axial bulk velocity. A lower v_{enc} would have yielded a higher sensitivity to low velocities but also increased T_E and the risk of phase aliasing. The effect of eddy currents on the phase angle is corrected by reference measurements taken without flow.

The RST is acquired in 2D measurements at $z/d_h = 1$ and $z/d_h = 4$ with 5 mm slice thickness and 1 mm in-plane resolution. At both positions, ICOSA6 with seven velocity sensitivities m_1^{enc} ranging from $1.5\,\mathrm{mT\,m^{-1}\,ms^2}$ to $20\,\mathrm{mT\,m^{-1}\,ms^2}$ was used. These values correspond to a velocity encoding v_{enc} of $4.12\,\mathrm{m\,s^{-1}}$ to $0.31\,\mathrm{m\,s^{-1}}$. The timing parameters T_E and T_R were set for the highest m_1^{enc} and are maintained for all lower velocity sensitivities.

8.2. Measurement Accuracy

As mentioned in the introduction to this chapter, measurements with the swirl-type spacer grid were undertaken within the first commissioning of the fuel assembly setup. It turned out that the heating of the flow medium was too slow to perform all measurements at the target conditions in the given time frame. Table 8.2 lists the actual reached boundary conditions captured by the

sensors installed in the flow circuit as presented in section 6.2. The mean flow rate calculated from the 3D3C MRV measurements is also presented. The value is calculated within the region of low systematic errors, which is discussed in more detail in the following. For now, this comparison focuses on emphasizing the good agreement between the sensor values and the flow rate calculated from MRV.

The lowest Reynolds number of approximately 38 000 was reached for the 3D measurements, and the Reynolds number in the RST measurement at $z/d_h = 1$ was about 10 % below the target value. All further measurements were conducted at the desired Reynolds number of 50 250. Uncertainties in the boundary conditions arise from the provided flow rate and temperature, also listed in Tab. 8.2. The deviation in the Reynolds number is expected to not significantly affect the acquired flow field. Similar observations were made based on PIV measurements in a fuel assembly model by Qu et al. (2019). They found strong similarities in the flow field downstream of a spacer grid for Reynolds numbers from 13 200 to 39 600. The differences became apparent only at a significantly smaller Reynolds number of 6600. Furthermore, Tab. 8.2 lists the sensitivities achieved in the measurements that result from the influence of random noise and turbulent motion artifacts. The relative values are related to the axial bulk velocity w_b.

Furthermore, it is important to investigate the impact of systematic errors

Table 8.2.: Accuracy of the boundary conditions and sensitivities of the measurements for the swirl-type spacer grid design. For the MRV results, the range of Q, w_z and the Reynolds number are calculated using twice the measurement uncertainty $\tilde{\sigma}_w$ of the axial velocity, which corresponds to the 95 % confidence interval.

Boundary Conditions				
		target	sensor	MRV
Flow rate Q in $\mathrm{L\,min^{-1}}$		1150	1150.0 ± 11.5	1166 ± 100
Bulk velocity w_z in $\mathrm{m\,s^{-1}}$		1.90	1.89 ± 0.02	1.92 ± 0.16
Temperatur in °C		35	35.0 ± 0.5	
Reynolds number		50 250	$50\,250 \pm 1230$	$51\,070 \pm 4260$
Temperatur in °C (3D MRV)			22.7 ± 2.2	
Reynolds number			38 570	
Temperatur in °C (2D RST, $z/d_h = 1$)			30.0 ± 0.6	
Reynolds number			45 430	
MRV measurement accuracy (68 % confidence)				
			absolute	relative to w_{bulk}
2D	velocity u_i		$0.04\,\mathrm{m\,s^{-1}}$	2.0 %
	turbulence intensity u_{rms}		$0.12\,\mathrm{m\,s^{-1}}$	6.1 %
	shear stress $\langle u_i' u_j' \rangle$		$0.03\,\mathrm{m^2\,s^{-2}}$	0.8 %
3D	velocity u_i		$0.09\,\mathrm{m\,s^{-1}}$	4.5 %

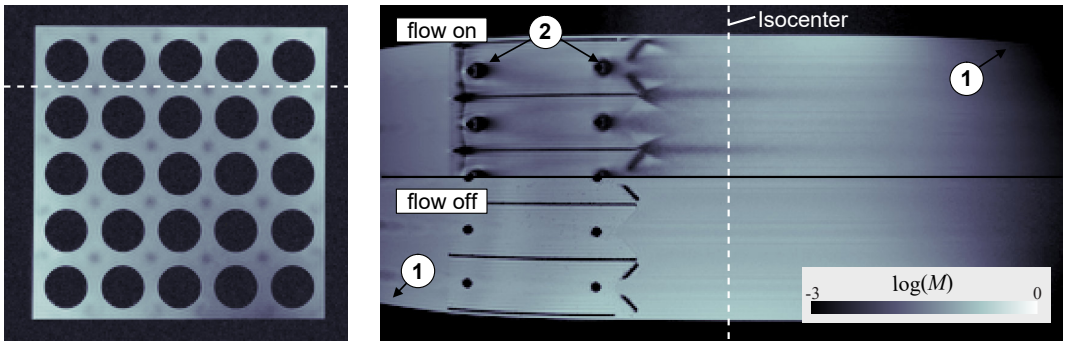

Figure 8.2.: Signal magnitude in two planes of the 3D3C velocity measurements. On the right, results from measurements with and without flow illustrate the effect of flow-induced errors. ① indicates the effect of non-linearity in the magnetic field gradients, which is present regardless of the fluid motion. ② highlights the effect of the flow on the signal quality in the proximity of the supports inside the spacer grid.

that arise from flow-induced errors. Previous studies have shown that such errors can cause significant quantitative deviations in the measurement results(Bruschewski et al., 2019; Schmidt et al., 2020). A qualitative impression of their effect is shown in Fig. 8.2. Here, the magnitude of the signal obtained from 3D measurements is depicted by two planes: one perpendicular to the channel axis at the isocenter, and the other along the center line between two layers of rods. The latter illustrates the measurements with flow in the upper half and without flow in the lower half to reveal the impact of the flow on the signal quality.

The distortions at the outer edges of the FOV are independent of fluid motion and result from the rising non-linearity of the magnetic field gradients, indicated by ①. The data obtained with flow yields substantial signal attenuation in the center of the subchannels and inside the spacer grid, in particular at the supports ②. Susceptibility differences or other magnetic field imperfections are unlikely to cause these artifacts since they do not appear in the reference measurement without flow. Therefore, the signal attenuation can be attributed to significant phase deviations from higher orders of motion.

A more quantitative analysis of the effect of systematic errors is obtained by considering the flow rate. Following the conservation of mass of incompressible fluids, Q is constant along the channel axis (z-direction). However, Fig. 8.3 reveals significant deviations of up to 50 % to the target flow rate. At the outer edges of the FOV, again indicated by ①, the rising non-linearity of the magnetic field gradients generates distortions that result in an underestimation of the fluid-filled volume and a bias in the measured velocity. When the flow enters the spacer, the deviations increase again. On the one hand, more voxels are affected by partial volume effects due to the thin walls and the complex structure of the spacer grid. On the other hand, the redirection of the flow

results in misregistration and increased phase deviations due to higher orders of motion. This becomes especially apparent at the supports, indicated by ② in Fig. 8.2. Finally, the effect of misregistration results in a displacement of the flow field that becomes apparent in the overestimated flow rate downstream of the spacer grid, marked by ③. Despite these local deviations, the flow rate is in good agreement with the target value in a downstream region from $z/d_h = 1$ to $z/d_h = 7$. Here, the velocity measurements are expected to be only influenced by random errors and uncertainties in the flow properties.

The effect of systematic errors for the turbulence quantification, is visualized in 8.4. The signal intensity $|S_0|$ of a reference measurement with $\boldsymbol{k}_v = 0$ already yields a significant signal attenuation in the center of the subchannels, similar to the velocity measurements. Additionally, the profiles of the lateral Reynolds normal stresses $\langle u_i'^2 \rangle$ are shown. Due to the rotational symmetry of the mixing vane configuration, it is expected that $\langle u(y)'^2 \rangle = \langle v(x)'^2 \rangle$. While this is confirmed at $z/d_h = 4$, stronger deviations occur closer to the spacer grid, especially in the center of the subchannels at $|x_i/P| = 0.5, 1.5$. Additionally, high variations in the data occur, which are more likely to be considered outliers resulting from a low measurement accuracy.

The effect of systematic errors is further illustrated in figur 8.5, where the results of the Gaussian fit in three different voxels for the second and the last velocity-sensitive encoding in the ICOSA6 encoding scheme are depicted. The accuracy of this fit is affected by two systematic errors: On the one hand, the signal attenuation from higher orders of motion results in low sensitivity to turbulent fluctuations. On the other hand, the native velocity distribution may not follow a Gaussian distribution. Therefore, deviations between measured values and fitted curves indicate the impact of systematic errors on the measurement results. The results obtained from three voxels are considered, representing regions of low (blue), medium (black), and (red) turbulence

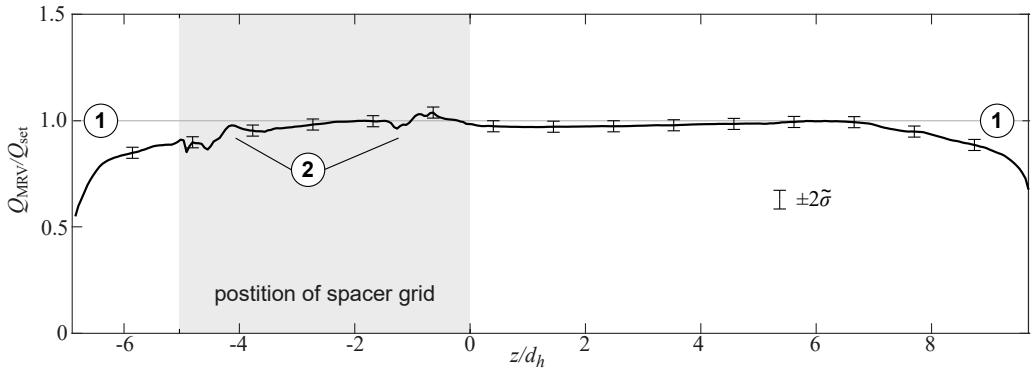

Figure 8.3.: Flow rate from 3D3C velocity measurements with indicators of systematic errors: ① magnetic field non-linearity, ② increased sensitivity to flow-induced errors, and ③ misregistration.

intensities.

The most significant deviations occur for the voxel in the center of the subchannel. The calculated 3D Gaussian distribution strongly deviates from the measured data points at both distances to the spacer grid. Additionally, the 6th encoding at $z/d_h = 1$ reveals that the last encodings $m_1^{enc} = \{10, 15, 20\}$ in the red curve are highly affected by the signal attenuation due to higher orders of motion. Their signal ratio is close to the ideal value of 0.6, and their contribution to the Gaussian fit is thus not adjusted by the weighting function. Lower deviations are apparent for the black curve representing medium turbulence intensity, and the low turbulent region shows a reasonable agreement in all considered graphs.

Figure 8.5 also yields that at least the first two velocity sensitivities $m_1^{enc} = 1$ and $m_1^{enc} = 2.5$ are not creating a measurable signal attenuation compared to the reference measurement. At the same time, the other measured data points rarely coincide with the ideal ratio of $|S|/|S_0| = 0.6$. Thus, the dynamic range achieved with the selected m_1^{enc} is not optimal.

To analyze the quality of the Gaussian fit in the entire ROI, the residuum r of the weighted least square fit is illustrated in Fig. 8.6. A high residuum indicates a strong deviation between measured values and calculated Gaussian distribution. As before, the strongest deviations arise in the center of the subchannels, and with distance to the spacer grid, the fit seems to perform much better. The voxels analyzed in Fig. 8.5 are highlighted to point out that the deviations observed in the individual encodings are related to the residuum of the entire 3D fit.

A significant deviation from a Gaussian velocity distribution arises in the presence of variations in the mean velocity inside the voxel. The effect is here

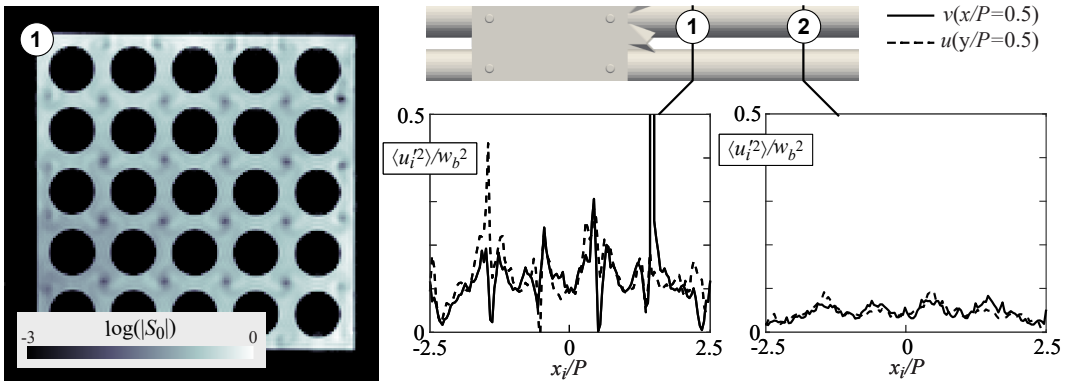

Figure 8.4.: Indicators of systematic errors in the RST measurements. The reference measurement $|S_0|$, shown on the left, yields significant signal attenuation in the center of the subchannels. The graphs on the right side yield the lateral Reynolds normal stresses $\langle u'^2 \rangle$ and $\langle v'^2 \rangle$. Due to the rotational symmetry of the fuel assembly, they should be similar. However, the results at $z/d_h = 1$ appear to be strongly affected by errors.

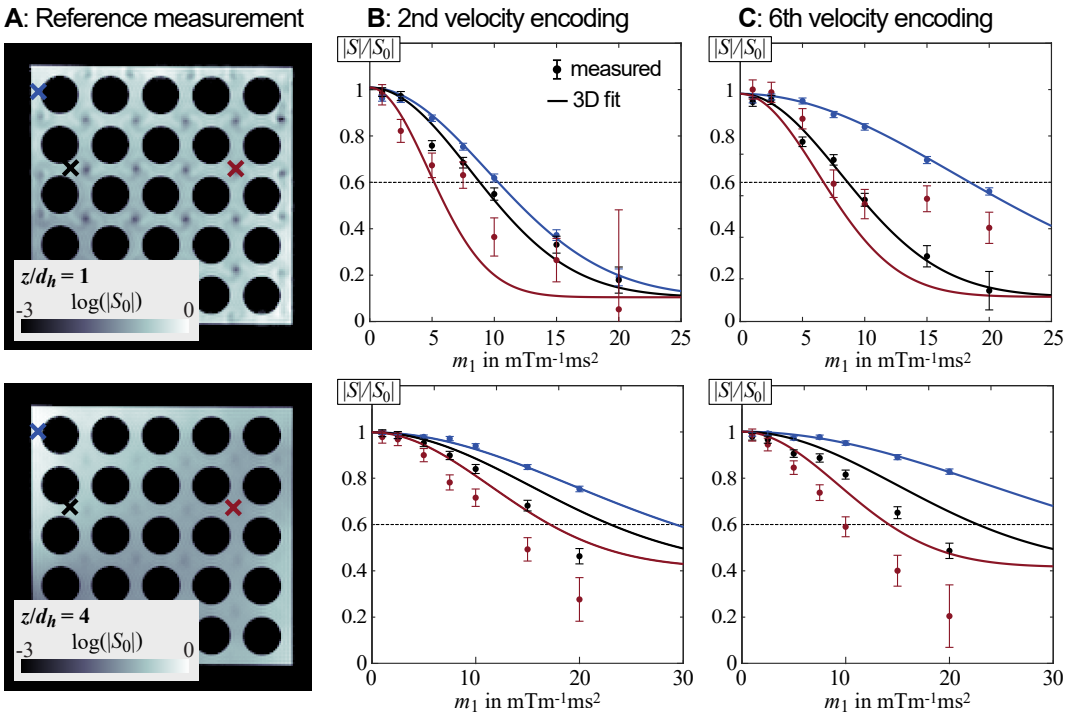

Figure 8.5.: Examples of 3D Gaussian fit in different voxels at both distances to the spacer grid. **A** shows the signal magnitude of the reference measurement $|S_0|$ and the selected voxels are higlighted by colored crosses. They represent regions with low (blue), medium (black), and high (red) turbulent kinetic energy. The graphs in **B** and **C** depict the measured signal intensities $|S|/|S_0|$ for all velocity sensitivities m_1^{enc} for two encodings of the ICOSA6 scheme. The fitted lines result from the entire 3D weighted least square optimization.

corrected using the 2D velocity measurements and the approach proposed by Dyverfeldt et al. (2009) assuming a linear gradient of the mean velocity. Figure 8.7 illustrates the deviation in the turbulent kinetic energy, calculated from a regular reconstruction of the RST and with previously correcting the relative signal intensities by the effect from the mean velocity variance. Additionally, profiles of the lateral turbulence intensities are shown. However, the correction does not significantly affect the results.

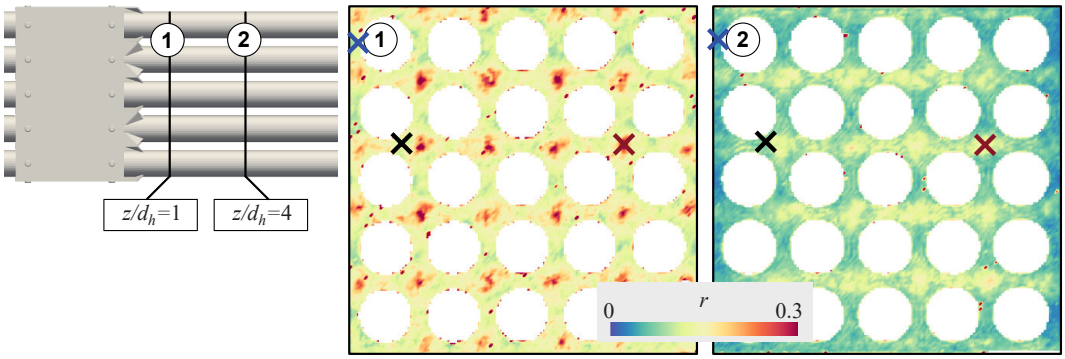

Figure 8.6.: Residuum of the 3D Gaussian fit at $z/d_h = 1$ and $z/d_h = 4$.

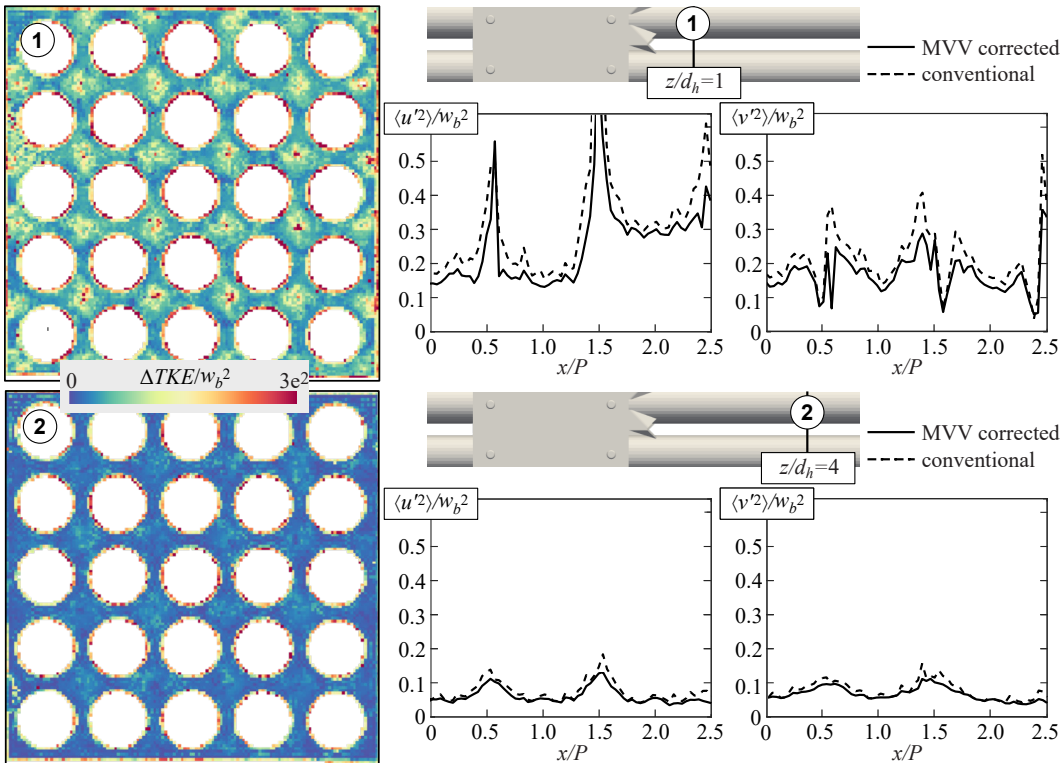

Figure 8.7.: Effect of mean velocity variance (MVV) on the turbulent kinetic energy TKE and the turbulence intensities $\langle u_i'^2 \rangle$ at $z/d_h = 1$ and $z/d_h = 4$.

8.3. Results

Having analyzed the effect of systematic errors in the swirl-type measurements, this section focuses on visualizing the results to get a qualitative impression of the data obtained from MRV. Figure 8.8 shows the magnitude and the vector field of the mean velocity in two slices. The structure of the spacer grid is included from CAD, but the rods are not shown for better visibility. The spacing of the vectors corresponds to the measurement resolution. The enlarged section visualizes the effect of flow-induced errors on the measured flow field that caused significant deviations in the flow rate. Behind the supports inside the spacer grid, a recirculation exits. Thus, the flow is strongly affected by acceleration and higher orders of motion, resulting in the previously observed systematic errors.

Nonetheless, the streamlines calculated from the measurement data in Fig. 8.9, indicate that the measurement is still capable of capturing the characteristic flow structure formed by the swirl-type spacer grid: The mixing vanes create a swirl in the center of the subchannel without substantial mixing to the neighboring subchannels. The streamlines were calculated from 100 points within a sphere of 10 mm radius located shortly behind the mixing vanes and centered in the middle of the subchannel.

Figure 8.10 shows the measured components of the Reynolds stress tensor and

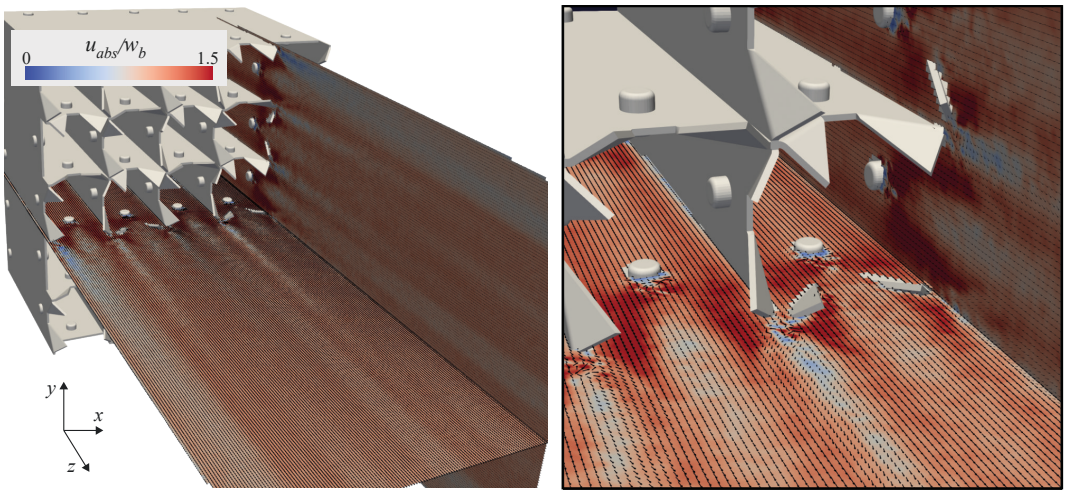

Figure 8.8.: Magnitude and vectors of the mean velocity from 3D measurements in the swirl-type spacer. The spacing of the vectors represents the native resolution of the experimental data. The geometry of the spacer grid is included from CAD for orientation.

the turbulent kinetic energy TKE calculated from the normal stresses at both distances to the spacer grid. Additionally, in-plane velocity vectors from 2D measurements illustrate the direction of the flow. The size of the vectors corresponds to the SFI to show the decay of secondary flow with further distance to the spacer grid. For better visibility, only the flow field in the four subchannels around the center of the fuel assembly is shown.

The lateral components $\langle u'^2 \rangle$ and $\langle v'^2 \rangle$ yield a poor symmetry that indicates the influence of systematic errors. It is anticipated that the low values of $\langle v'^2 \rangle$ in the center of the subchannels are more likely a result of systematic errors rather than an accurate representation of the natural flow field. This component aligns with the readout direction, reinforcing the effect of higher orders

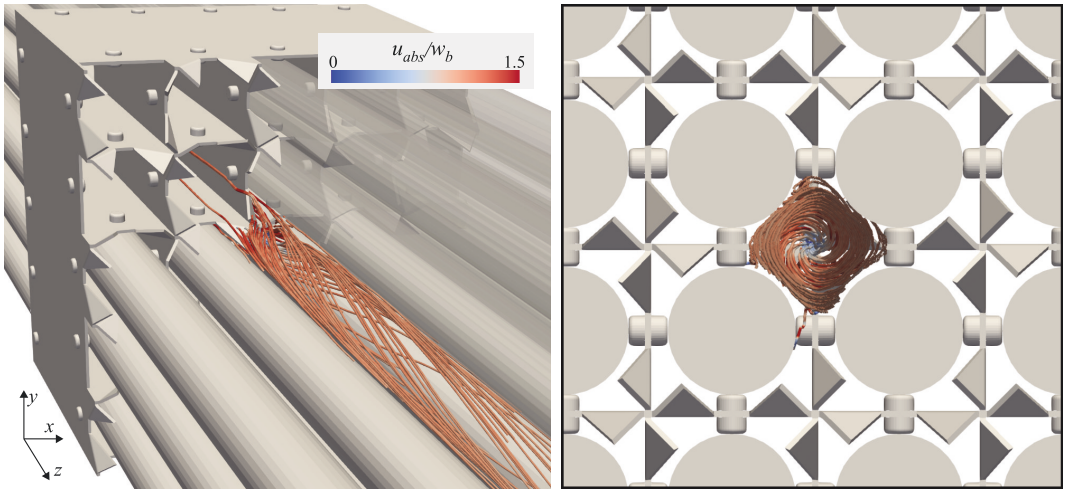

Figure 8.9.: Streamlines in a subchannel calculated from 3D mean velocity MRV results in the swirl-type spacer grid.

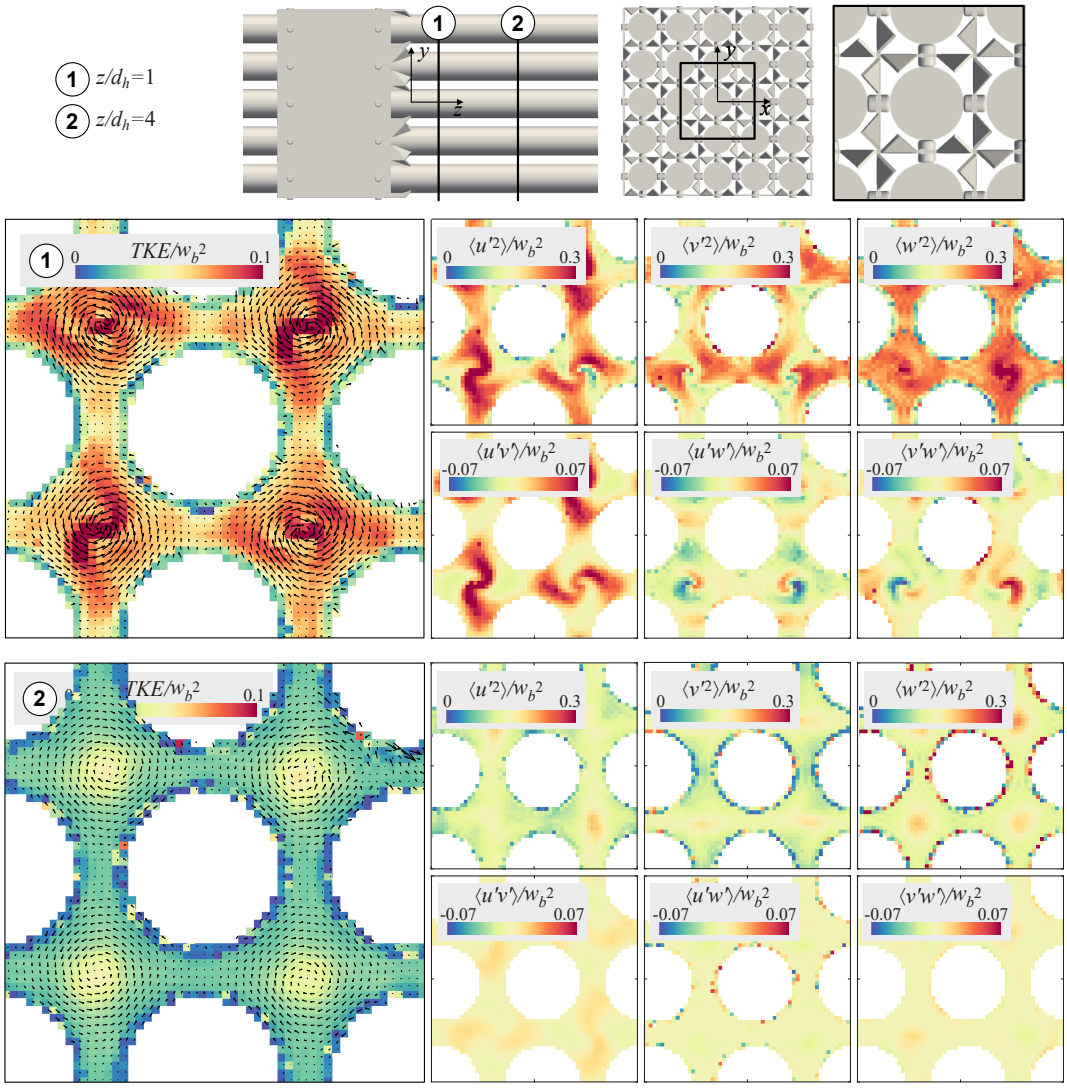

Figure 8.10.: Turbulent kinetic energy TKE and all components of the Reynolds stress tensor $\boldsymbol{\tau}$ measured at $z/d_h = 1$ (top) and $z/d_h = 4$ (bottom) distance to the swirl-type spacer grid. The in-plane velocity vectors are also shown in the TKE to illustrate the flow motion.

of motion. Similarly, the peak values of the axial turbulence intensity vary considerably within the different subchannels. Both effects are significantly reduced at $z/d_h = 4$ where the decay of turbulence and the secondary flow intensity lowers the effect of flow-induced errors.

At both measurement positions, the effect of correcting the mean velocity variance becomes apparent in the reduced turbulent kinetic energy toward the rods and the channel wall. However, the individual Reynolds stresses yield substantial variations in these regions. It is most likely that the correction further reduces the accuracy of the Gaussian fit due to poor sensitivity to low turbulence intensities in the selected m_1^{enc}.

9. Split-Type Spacer

In a final measurement campaign, the flow field behind the split-type spacer grid is investigated. As the previous spacer grid, it is designed on the dimensions published by the NEA (2013). The main part that supports the rods is formed identically, but only two mixing vanes bend by 30° are positioned at each crossing of the grid. These mixing vanes are either orientated up and down or left and right, as illustrated by the black arrows in Fig. 9.1.

Different optimizations in the experimental setup and the imaging routine resulted from the first measurements to improve the reliability of the measurements. Additional heating was implemented to reach the target flow condition faster. As a result, all measurements conducted within this second measurement campaign were performed at the intended Reynolds number of 50 250. It was also possible to increase the target fluid temperature to lower the bulk velocity from $w_b = 1.9\,\mathrm{m\,s^{-1}}$ to $w_b = 1.7\,\mathrm{m\,s^{-1}}$ which is favorable to reduce the sensitivity to flow-induced errors. More importantly, the imaging routine was revised to minimize further the impact of these errors on the measurement results. The encoding gradients were optimized following the FAST scheme instead of ECHO, and an asymmetric readout is implemented. Both shorten the magnetic field gradients applied previously to the readout, which decreases T_E and reduces phase variations from higher orders of motion.

Besides acquiring the 3D3C mean velocity vector field and the 2D6C Reynolds stresses as in the initial measurement, measurements were conducted in a 2D FOV in a $y-z$-plane aligned with the gap between two layers of rods. This

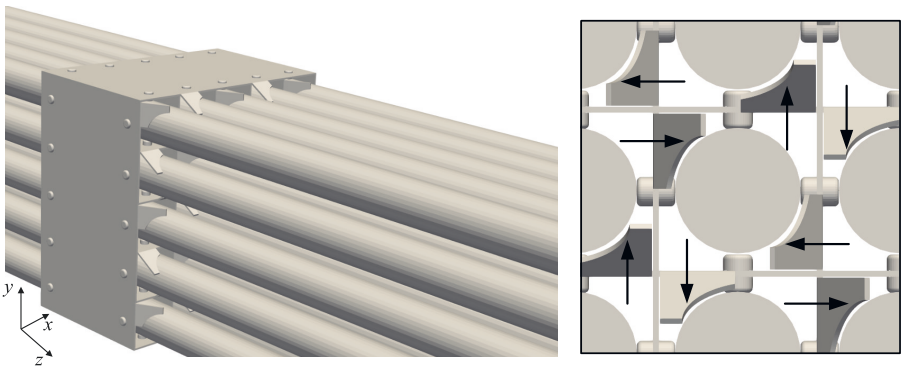

Figure 9.1.: CAD of the split-type spacer grid based on the details published by NEA (2013). The arrows indicate the orientation of the mixing vanes.

measurement was repeated after moving the fuel assembly to capture the upstream velocity field. Combining the results from both acquisitions provides insights into the evolution of turbulent kinetic energy at an axial length of about 400 mm, which equals 20 times the hydraulic diameter d_h.

9.1. Imaging Protocol

The measurements are again performed using Cartesian GRE PC MRI based on the 4D Flow. The gradient waveform design is now optimized following the FAST encoding scheme as originally intended by Markl et al. (2012). This minimizes the T_E, but m_1^{PE} changes with each phase encoding step, resulting in an uncontrolled displacement. The difference towards the ECHO encoding is illustrated in section 5.5 and is discussed in more detail by Schmidt et al. (2020). Additionally, an asymmetric readout is used to shorten the encoding process and move the echo closer to the encoding gradients, which is expected to reduce systematic errors further. The readout is not changed to keep the size of the k-space, and the data is reconstructed by the inverse Fourier transform without zero-filling or estimating the lower sampled part of the k-space.

The imaging parameters are summarized in Tab. 9.1. T_R and T_E are again kept to a minimum, and the flip angle is optimized to obtain the highest signal

Table 9.1.: Imaging parameters for acquiring mean velocity vector and Reynolds stresses downstream of the split-type.

	3D velocity	**2D velocity**	**2D RST**
FOV x, y, z [mm^3]	160×160×320	320×160×3.4	320 × 160 × 3.4
Resolution x, y, z [mm^3]	1.0 × 1.0 × 1.0	1.0 × 1.0 × 3.4	1.0 × 1.0 × 3.4
Matrix size x, y, z	160×160×320	320 × 160 × 1	320 × 160 × 1
Readout direction	z	y or z	y or z
T_E [ms]	1.3	2.5	3.4 to 3.6
T_R [ms]	5.0	6.0	6.0
Flip angle [°]	10	15	15
Slab selective	no	yes	yes
Pulse Duration [µs]	100	800	800
Pulse BWT	2.7	2.7	2.7
Echo asymmetry	0.1	0.1	0.1
Receiver bandwith per pixel [Hz]	920	950	950
Encoding scheme	4-point	4-point	ICOSA6
Gradient design	FAST	FAST	FAST
Velocity encoding [m s^{-1}]	4	4	0.26 to 2.3
No. of velocity encodings	1	1	10 to 12
Averages flow on	20	200	200
Averages flow off	5	60	-
Total acquisition time [min]	213	18	225 to 270

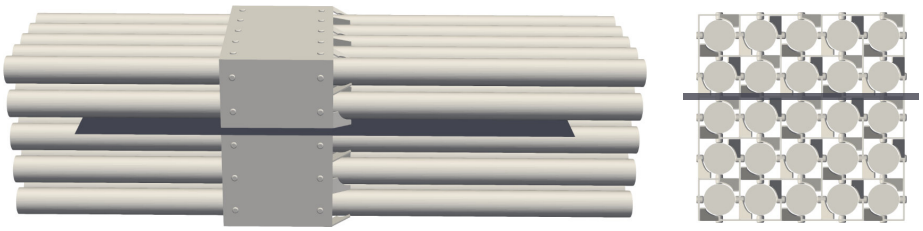

Figure 9.2.: Position of acquired data matrix from 2D6C RST and 2D3C measurements in a gap between two layers of rods. The results are combined from two measurements between which the setup was moved to extend the width of acquired data to approximately 400 mm.

intensity. The reduced SNR from increasing the bandwidth is compensated through a high number of averages which is increased compared to the first measurements. The asymmetry of the echo is set to 10 %, whereas 50 % corresponds to a symmetric readout. Additionally, adjustments in the design of the pulse profile lowered the duration of the slice selection to further reduce T_E and to shorten the magnetic field gradients, which reduced the distinction of the slice selection.
The mean velocity vector is acquired in a 3D volume with 1 mm isotropic resolution covering a ROI from shortly upstream to approximately $z/d_h = 10$ downstream of the spacer grid. The adjustments in the sequence design resulted in a significant decrease in T_E from 3.3 ms down to 1.3 ms. Additionally, the number of averages was increased to 20 and the v_{enc} is slightly decreased to $3.91\,\mathrm{m\,s^{-1}}$.

The RST was acquired in the same 2D FOVs at $z/d_h = 1$ and $z/d_h = 4$ but also in a $y-z$-plane aligned with the gap between two layers of rods at $y/P = 0.5$. The latter measurement was repeated while the setup was positioned for the upstream measurements. Combining these measurements yields a FOV of about 400 mm as illustrated in Fig. 9.2. As the minimal distance between the surface of the rods is 6.71 mm, it was required to reduce the slice thickness to 3.4 mm.

For the turbulence quantification, the dynamic range was improved by increasing the number of m_1^{enc}. Additionally, the values were adapted depending on the distance to the spacer grid. At $z/d_h = 1$, 12 different sensitivities are acquired ranging from $3\,\mathrm{mT\,m^{-1}\,ms^2}$ to $20\,\mathrm{mT\,m^{-1}\,ms^2}$, while only 10 m_1^{enc} were captured at $z/d_h = 4$. For the latter, the sensitivities were increased to $6\,\mathrm{mT\,m^{-1}\,ms^2}$ to $27\,\mathrm{mT\,m^{-1}\,ms^2}$ to account for the expected decay of turbulence intensity. Moreover, the selected m_1^{enc} were more equally distributed to increase the number of measurements conducted with a high velocity sensitivity. This adjustment resulted from the observation in the swirl-type measurement that most of the selected m_1^{enc} were too low to correctly quantify

the RST in the entire ROI. Again, 2D velocity measurements were performed at each position of turbulence quantification to correct for the effect of mean velocity variance.

9.2. Measurement Accuracy

Table 9.2 lists the uncertainties in the boundary conditions resulting from the measurement instruments to control the flow rate and the temperature, as well as the mean flow rate calculated from the measured axial velocity w_z in regions of low systematic errors. Again, the MRV results are in good agreement with the sensor values. Furthermore, the accuracy resulting from random noise and turbulent motion artifacts is listed. The relative values refer to the axial bulk velocity w_z. All values have improved compared to the swirl-type measurements, but the uncertainty in the turbulence measurement remains fairly high.

As for the swirl-type spacer, the signal magnitude in two planes of the 3D measurement is depicted in Fig. 9.3 for a first impression of the effect of systematic measurement errors. Again, the signal magnitude obtained from the measurements without flow is shown in the lower half of the slice along the axial direction to illustrate the effect of the fluid motion on the data. Unlike the previous measurements with the swirl-type spacer, the signal attenuation inside the spacer grid is significantly reduced, resulting in almost no differences between the measurements with and without flow. Slight distortions can be found at the mixing vanes that can be contributed to misregistration. In ad-

Table 9.2.: Accuracy of the boundary conditions and the measurements for the split-type spacer grid design. For the MRV results, the range for Q, w_z and the Reynolds number are calculated using twice the measurement uncertainty $\tilde{\sigma}_w$ of the axial velocity, which corresponds to the 95 % confidence interval.

Boundary Conditions				
		target	sensor	MRV
Flow rate Q in $\mathrm{L\,min^{-1}}$		1045	1048 ± 3	1027 ± 40
Bulk velocity w_z in $\mathrm{m\,s^{-1}}$		1.72	1.73 ± 0.01	1.69 ± 0.06
Temperatur in °C		40	40	-
Reynolds number		50 250	$50\,250 \pm 1430$	$49\,460 \pm 1900$
MRV measurement accuracy (68 % confidence)				
			absolute	relative to w_{bulk}
2D	velocity u_i		$0.02\,\mathrm{m\,s^{-1}}$	1.1 %
	turbulence intensity u_rms		$0.07\,\mathrm{m\,s^{-1}}$	4.3 %
	shear stress $\langle u_i' u_j' \rangle$		$0.02\,\mathrm{m^2\,s^{-2}}$	0.7 %
3D	velocity u_i		$0.03\,\mathrm{m\,s^{-1}}$	1.9 %

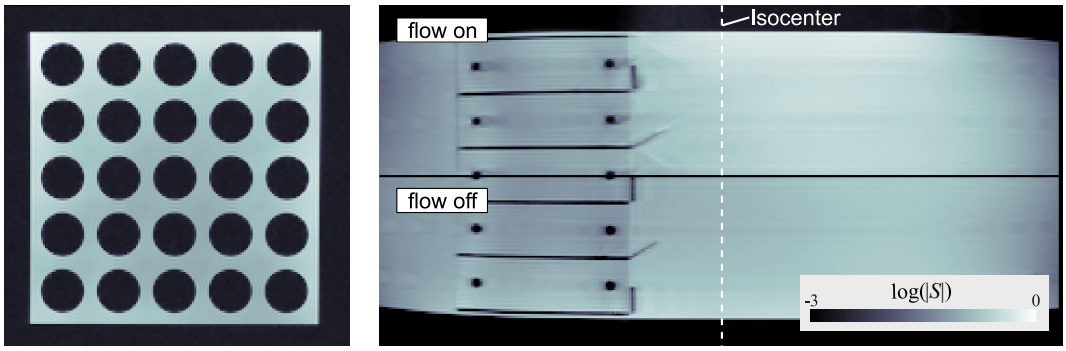

Figure 9.3.: Signal magnitude in two planes of the 3D3C velocity measurements. On the right, results from measurements with and without flow are shown. Compared to the swirl-type measurement, only minor changes in the signal intensity are visible, which indicates a significantly reduced sensitivity toward systematic errors.

dition, the asymmetry in the k-space becomes apparent through smearing in the contours independently of the fluid motion.

The improvements in the signal magnitude also appear in the calculated flow rate shown in Fig. 9.4. The distortions at the outer edges of the FOV ① due to the rising non-linearity of the magnetic gradients remain. Still, the effects inside the spacer grid are significantly reduced. Deviations in the proximity of the supports ② and the mixing vanes are primarily caused by partial volume effects that affect the separation of the fluid-filled volume.

Similar improvements in the measurement results are obtained for the turbulence quantification. The signal quality and the symmetry of the lateral turbulence intensities are depicted in Fig. 9.5. The signal magnitude yields a uniform distribution, and the profiles of u_{rms} and v_{rms} are in good qualitative agreement at both distances to the spacer grid. Deviations at $z/d_h = 1$ in the quantitative values can be attributed to the different sensitivity of frequency and phase encoding direction towards higher orders of motion.

Figure 9.6 shows the quality of the Gaussian fit at similar positions as for

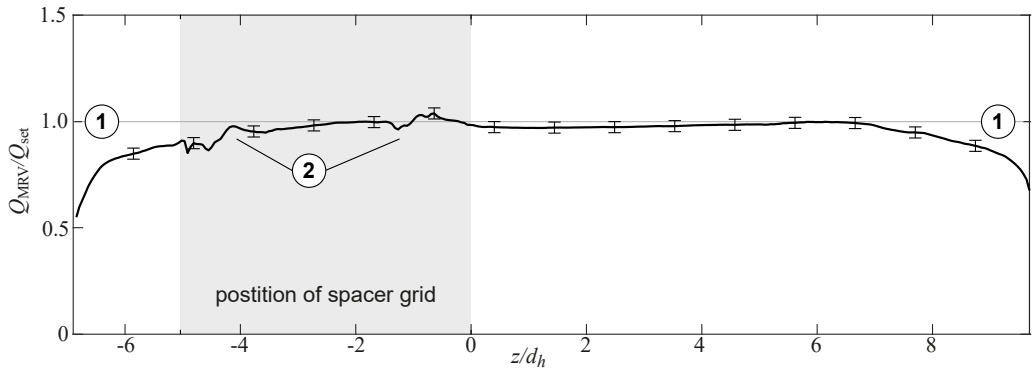

Figure 9.4.: Flow rate from 3D3C velocity measurements with indicators of systematic errors: ① magnetic field non-linearity and ② increased sensitivity to systematic errors.

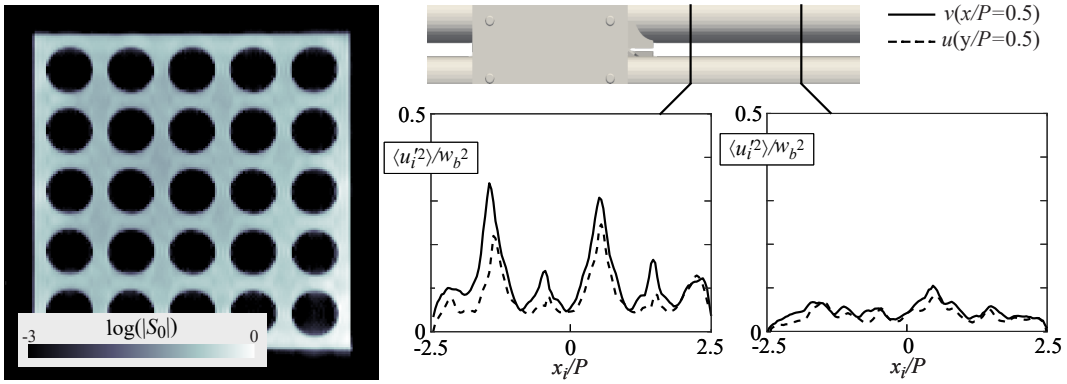

Figure 9.5.: Indicators of systematic errors in the RST measurements. The reference measurement $|S_0|$, shown on the left, yields no significant signal attenuation. The graphs on the right compare the lateral Reynolds normal stresses $\langle u'(x)^2 \rangle$ and $\langle v'(y)^2 \rangle$, which should be similar due to the rotational symmetry of the spacer grid design. Some minor deviations are apparent, but the results have significantly improved compared to the first measurement with the swirl-type spacer grid.

the swirl-type spacer. The voxels are again selected to represent regions with high (red), medium (black), and low (blue) turbulence intensity. The improved selection of velocity sensitivities m_1^{enc} results in measured values close to the

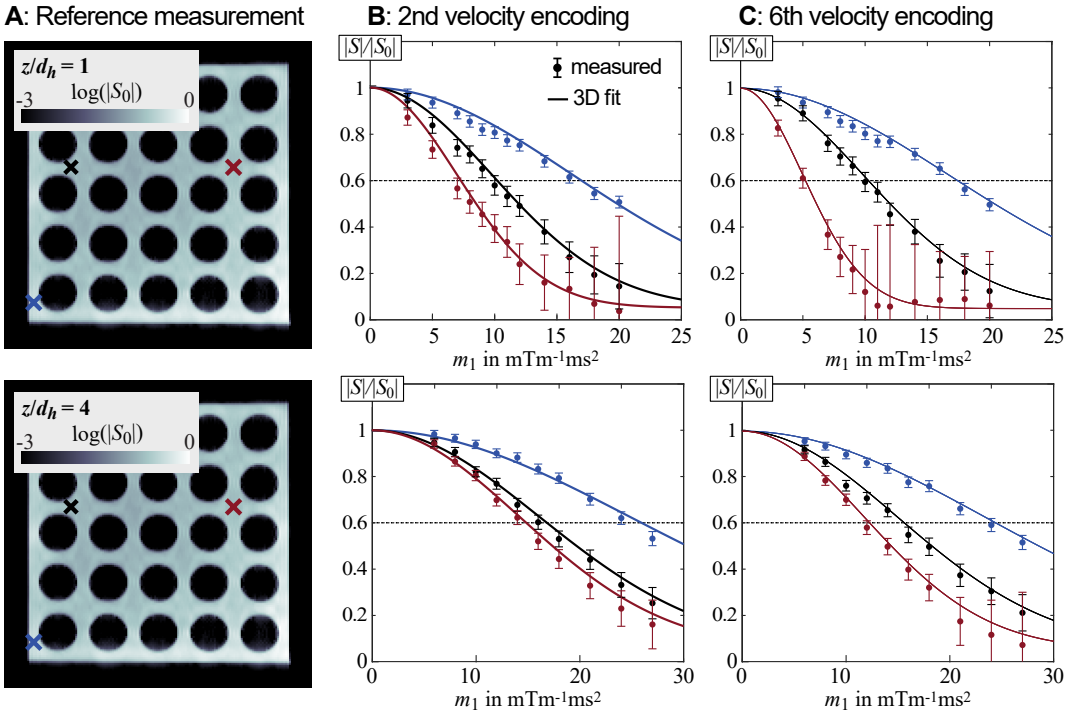

Figure 9.6.: Examples of 3D Gaussian fit in different voxels at both distances to the split-type spacer grid. **A** shows the signal magnitude of the reference measurement $|S_0|$ and the selected voxels are higlighted by colored crosses. They represent regions with low (blue), medium (black), and high (red) turbulent kinetic energy. The graphs in **B** and **C** depict the measured signal intensities $|S|/|S_0|$ for all velocity sensitivities m_1^{enc} for two encodings of the ICOSA6 scheme. The fitted lines result from the entire 3D least square optimization.

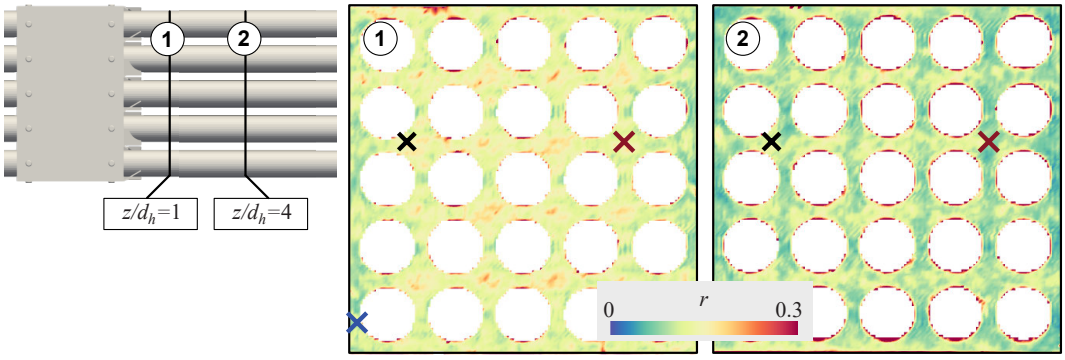

Figure 9.7.: Residuum r of 3D Gaussian fit at $z/d_h = 1$ and $z/d_h = 4$. The colored crosses yield the position of the voxels analyzed in Fig. 9.6

ideal signal ratio $|S|/|S_0|$ in all considered cases. All velocity sensitivities result in a measurable signal attenuation compared to the reference measurement. Especially in the center of the subchannel, the lower limit of resolvable signal attenuation due to random errors is below 0.1, which is significantly lower than the target ratio. Thus, the weighting function limits their contribution to the Gaussian fit. Additionally, the alignment of the fits with the measurement data is significantly improved compared to the measurements with the swirl-type spacer, even for the voxel at the center of the subchannel.

This impression is reinforced when considering the residual of the fit for all m_1^{enc} and encoding directions, illustrated in Fig. 9.7. A direct quantitative comparison with the previous measurements is not feasible since different m_1^{enc} and flow fields are captured. However, the residuum appears much more uniform. Again, the fit at $z/d_h = 4$ seems to perform better due to the decreased turbulence and secondary flow intensities. However, larger residuals are obtained in the voxels in the boundary layers, which are expected to be caused by the smearing that results from the asymmetric k-space.

Due to the improvements in the measurements, the effect of the correction for mean velocity variance (MVV) inside the voxels becomes more distinct, as shown in Fig. 9.8. Effects on the turbulent kinetic energy are observed in the subchannels and towards the walls. For comparison, the colormap has the same limits as in the analysis of the swirl-type spacer. For the split-type spacer, the correction has a lower effect on the results. This is likely not only due to variances in the strength of the mean velocity gradient but also due to the optimization in the imaging routine that increased the general accuracy of the fit. Furthermore, the overall effect of this correction is comparatively low, which corresponds to the observation by Dyverfeldt et al. (2009). The axial turbulence intensity w_{rms} is mainly affected at the boundary layer towards the walls, for example, at $x/P \approx 2.5$. For the lateral component v_{rms}, the swirl formed by the mixing vanes results in overestimating the peak values

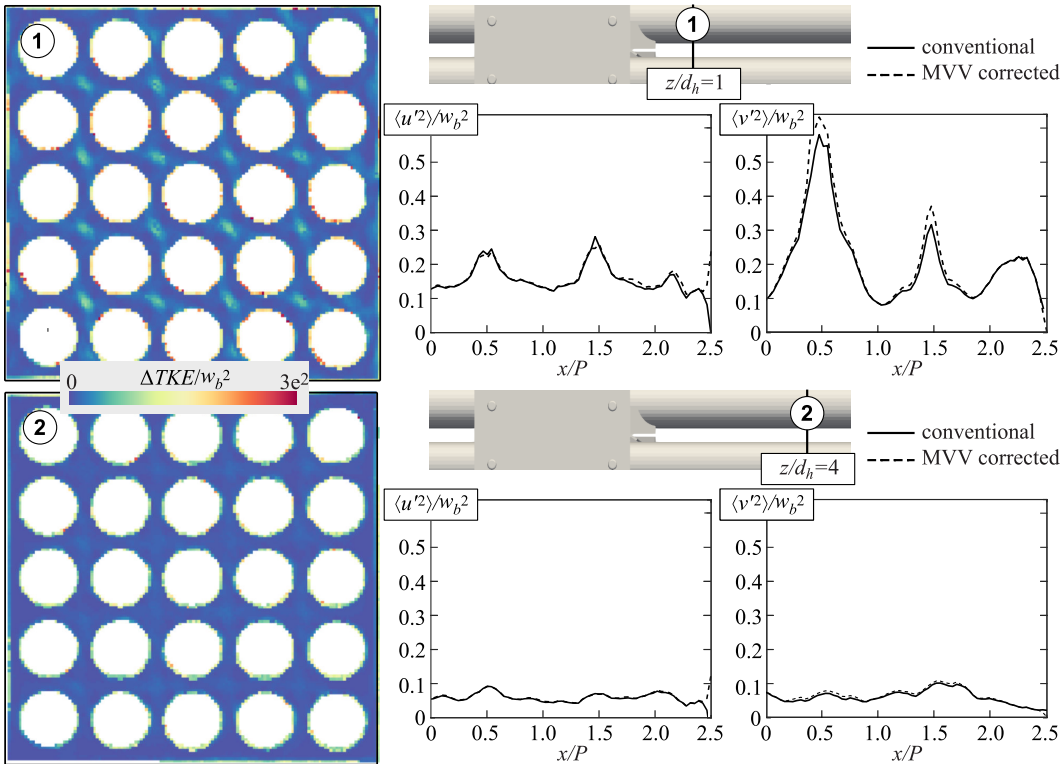

Figure 9.8.: Effect of mean velocity variance on the turbulent kinetic energy TKE and the turbulence intensities $\langle u_i'^2 \rangle$ at $z/d_h = 1$ and $z/d_h = 4$. The

at the center of the subchannel. As the turbulence intensity and the swirl decays downstream of the spacer grid, the effect of the mean velocity variance decreases at $z/d_h = 4$.

9.3. Results

The analysis of the measurement accuracy and the influence of systematic errors yields that reliable data quality can be expected from the measurements of the split-type spacer. Figure 9.9 illustrates the absolute velocity and the vectors of the mean velocity inside two planes in the 3D measurement volume. The cutout focuses on the velocity field inside the spacer grid, which was substantially affected by systematic errors in the swirl-type measurements. The velocity field in the split-type spacer appears much smoother, and the flow field around the supports and the mixing vanes seems the be accurately captured.

The streamlines calculated from the measurement data in Fig. 9.10 indicate the characteristic flow structure formed by the mixing vanes. They are again calculated from 100 points within a sphere of 10 mm radius shortly downstream of the mixing vanes. As for the swirl-type design, a swirl is generated in the center of the subchannel, but the split-type mixing vanes create a significant

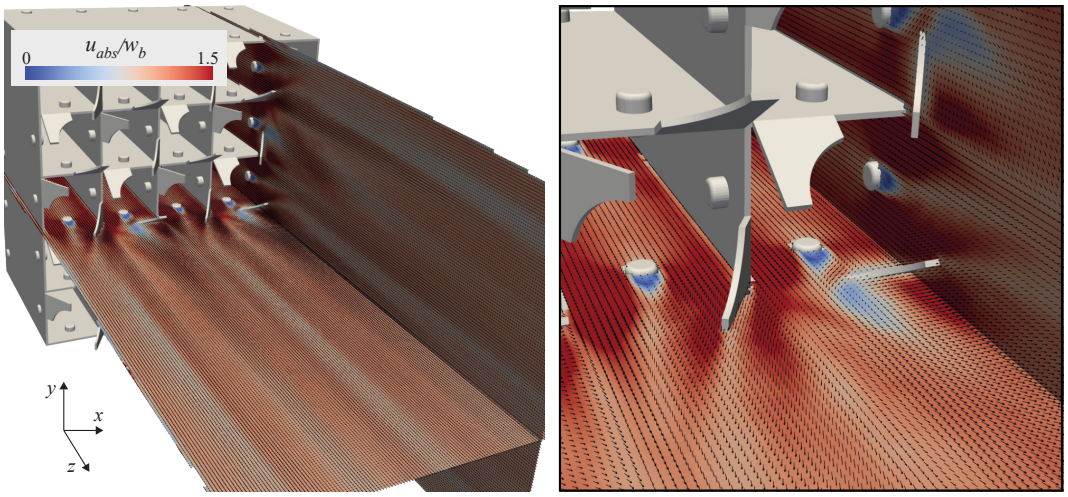

Figure 9.9.: Magnitude and vectors of the mean velocity from 3D measurements in the split-type spacer. The spacing of the vectors represents the native resolution of the experimental data. The geometry of the spacer grid is included from CAD for better orientation.

mixing towards the neighboring subchannels.

The high accuracy reached in these measurements also allows for calculating the Q-criterion Q_{crit} and the vorticity, providing a more quantitative visualization of the created flow structures. Figure 9.11 illustrates the isosurface of high positive Q_{crit} to identify the core of the vortices formed by the mixing vanes. They are colored with the vorticity to display their direction of rotation. This analysis also reveals some secondary flow structures in the gaps between the subchannels and at the backside of the mixing vanes.

Figure 9.12 depicts the results of the turbulence quantification corrected for mean velocity variance at both distances to the spacer grid. The turbulent kinetic energy with the in-plane velocity vector and all six components of the

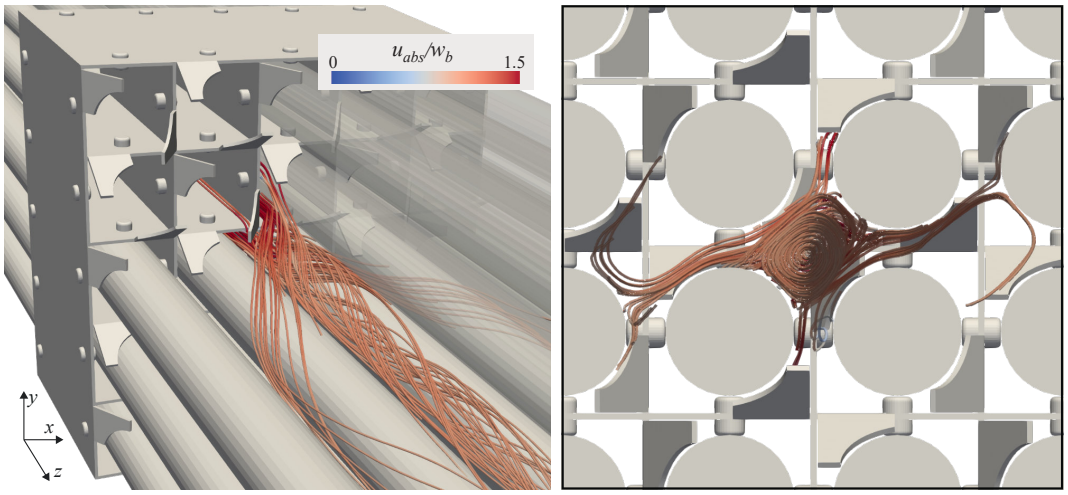

Figure 9.10.: Streamlines in a subchannel calculated from 3D mean velocity MRV results in the split-type spacer grid.

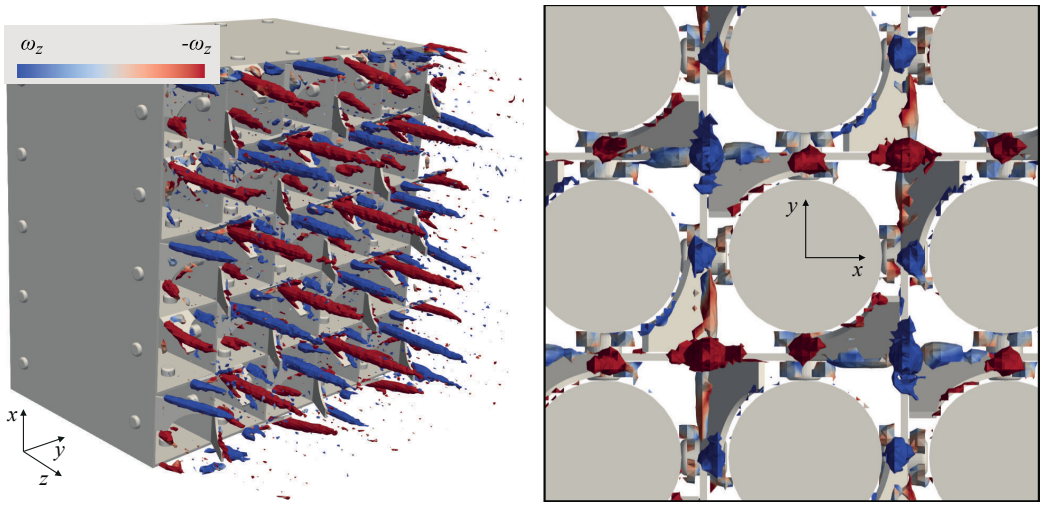

Figure 9.11.: Isosurfaces of high positive Q-criterion colored with vorticity to identify stationary vortices based on the 3D3C measurement data from MRV.

measured Reynolds stress tensor are depicted for the four subchannels at the center of the fuel assembly model. The data appears much smoother than for the swirl-type measurement. However, some differences in the rotational symmetry of the lateral turbulence intensities are present at $z/d_h = 1$, indicating the influence of systematic errors. Further downstream, the symmetry is more distinct.

Moreover, the RST was acquired in a 2D FOV at $y/P = -0.5$ along the axial direction. The combined results of the measurements upstream and downstream of the spacer grid are presented in Fig. 9.13. The contour plots show the residuum r of the 3D Gaussian fit and the TKE. The graph illustrates the averaged TKE_{cor} obtained in the FOV in the $y-z$-plane. At the intersection with the $x-y$-planes upstream, at $z/d_h = 1$ and $z/d_h = 4$, mean values TKE_{tra} at $y/P = -0.5$ from these measurements are plotted for comparison. The residuum is only a qualitative estimator of the accuracy of the RST quantification. Nonetheless, it reveals insights into the effect of errors in the results. Inside the spacer grid, the values are comparatively high. Here the slice thickness of the FOV covers the entire wall of the spacer grid, which has a size of approximately 1 mm. As a result, the boundary layers strongly affect the measurements, which cannot be corrected with the previously applied method. However, this illustrates the capability of MRV to provide measurement data across tissue boundaries. The low residuum upstream and from $z/d_h = 1$ downstream of the spacer indicates a low impact of systematic errors. These results are expected to provide reliable qualitative insight into the evolution of turbulence along the fuel assembly. The TKE substantially increases when the flow enters the spacer and reaches its peak at the mixing vanes. Behind the spacer grid, the turbulence level decays smoothly. The dotted lines in Fig. 9.13

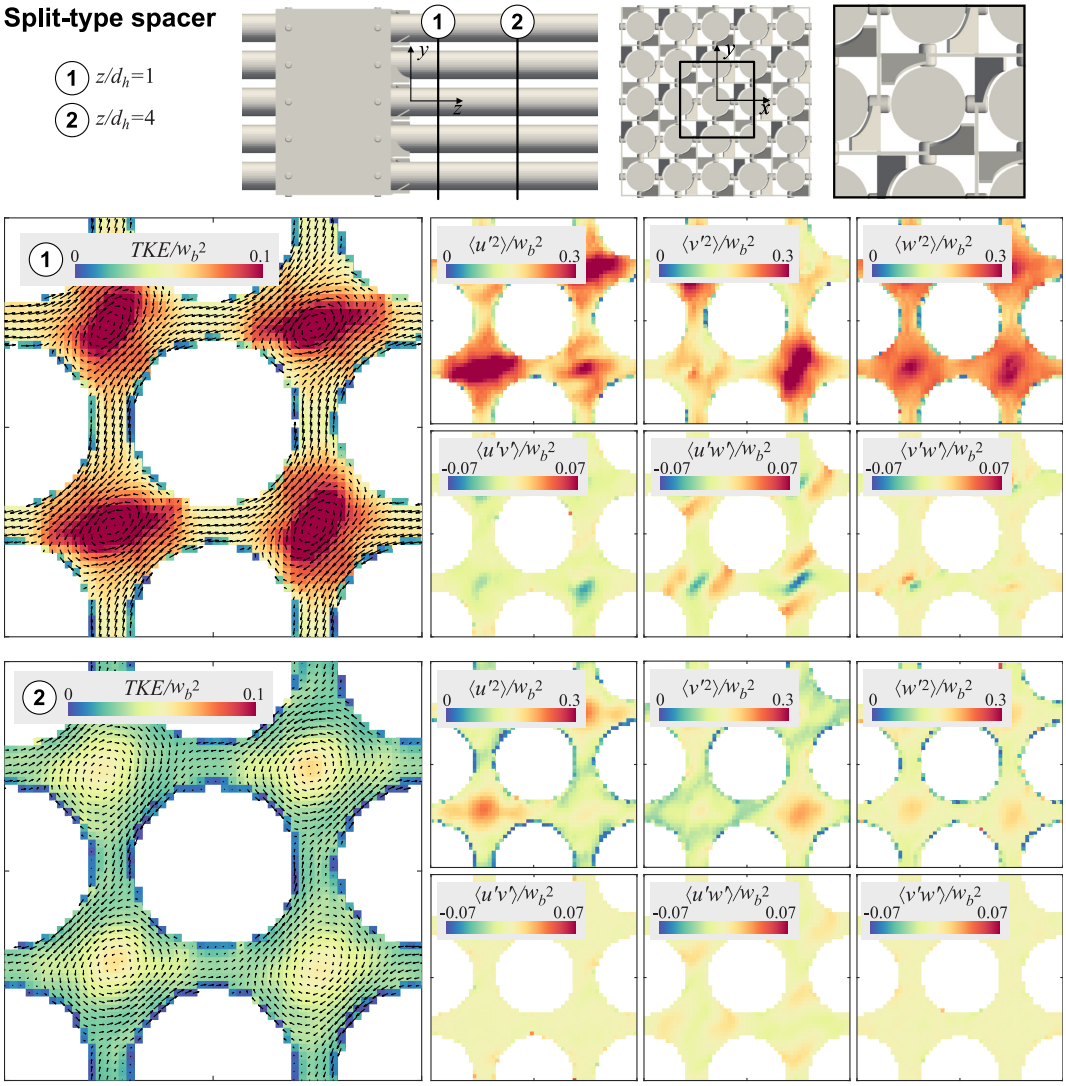

Figure 9.12.: Turbulent kinetic energy and all components of the Reynolds stress tensor measured at $z/d_h = 1$ and $z/d_h = 4$ distance to the split-type spacer grid.

indicate the relation between the contour plot and the graph. Upstream and at $z/d_h = 4$, the results obtained from the different measurement orientations compare well, but deviations occur at $z/d_h = 1$. In the proximity of the mixing vanes, the sensitivity towards flow-induced systematic errors increases, and their intensity depends on the imaging direction. For the coronal measurements, the mean flow direction aligns with the readout direction, which is expected to cause a stronger overestimation of turbulence shortly downstream of the spacer grid. This also compares well with the increased residuum at $z/d_h = 1$.

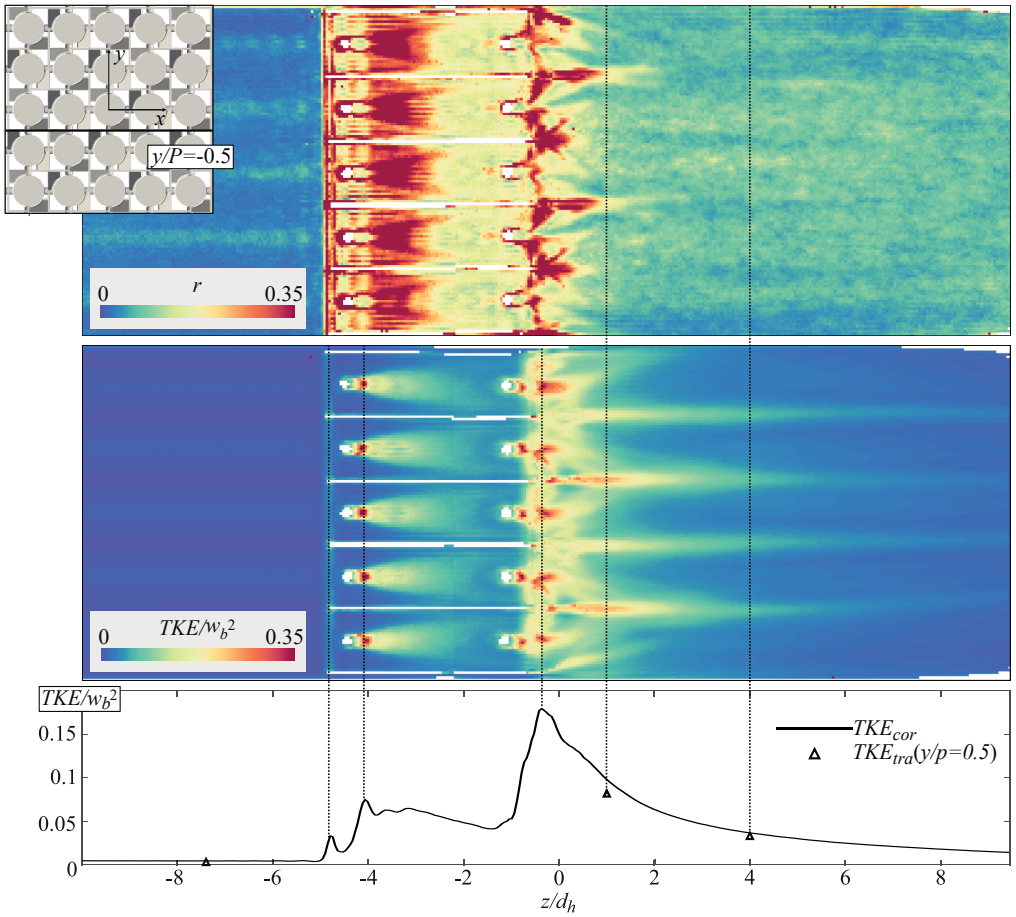

Figure 9.13.: Turbulent kinetic energy TKE in a slice along the channels axis at $y/P = 0.5$ combined from measurements upstream and downstream of the spacer grid. The top shows the residuum of the Gaussian fit, which yields an increased sensitivity to systematic errors inside the spacer grid. The middle shows the calculated turbulent kinetic energy TEK, and the bottom yields its mean along the channel's axis. Additionally, the averaged TKE at $y/P = 0.5$ obtained from the measurements upstream, at $z/d_h = 1$ and $z/d_h = 4$ are shown. At $z/d_h = 1$ the results of the different imaging orientations deviate due to the effect of systematic errors. Here, the residuum is higher than further downstream at $z/d_h = 4$ at which both measurements agree well.

10. Conclusive Remarks on the Measurement Campaign

This part summarized the MRV measurements in a replica of the OECD/NEA-KAERI benchmark. The requirements and advantages of MRV resulted in differences in the fuel assembly configuration compared to the MATIS-H setup used by Chang et al. (2014). A detailed comparison of their results is provided in the following part. This chapter summarizes the results of the measurements and the conclusions to be drawn from them.

The 3D3C velocity measurements, in particular, offer unique insights into the flow structure created by the mixing vanes, allowing for a comparison of their impact on the flow field. Figure 10.1 shows the secondary flow intensity (SFI) obtained from the entire cross-section of the fuel assembly and the lateral flow rate between two subchannels for both spacer grid designs. This comparison reveals the enhanced secondary flow and subchannel mixing generated by the split-type design, which reflects the findings by Chang et al. (2014). Thus, MRV yields persuasive data to quantify the effect of different spacer grid designs on the flow field.

However, the analysis of the measurement accuracy also identified the effect

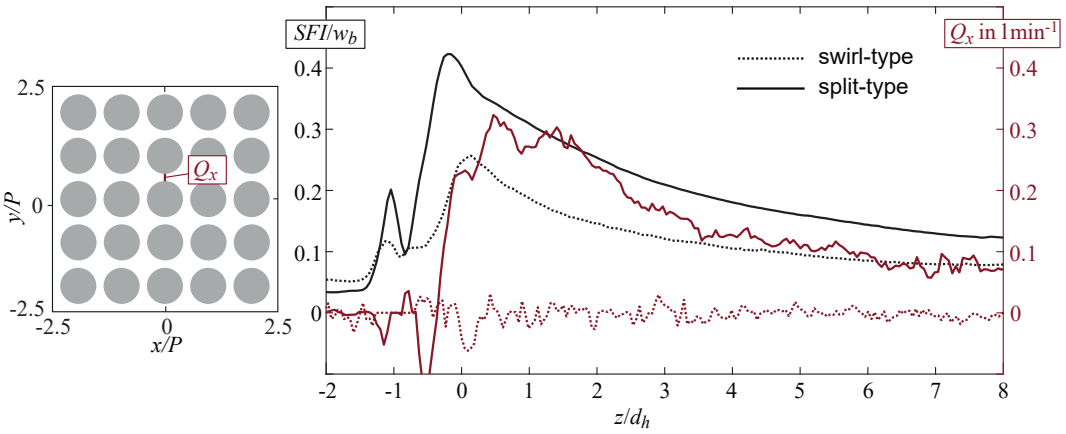

Figure 10.1.: Comparison of the flow field created by the different spacer grid designs based on the 3D3C mean velocity measurements. The secondary flow intensity SFI is calculated in the entire cross-section of the channel, while Q_x is the flow rate between two subchannels calculated along the red line as indicated in the channel's cross-section on the left.

of systematic errors, which were particularly present in the initial measurements with the swirl-type spacer. Here, the results of the 3D3C mean velocity measurements are found to only provide reliable results from $z/d_h = 1$ to $z/d_h = 7$ downstream of the mixing vanes. For the turbulence quantification, solely the data at $z/d_h = 4$ appears to provide accurate results. Improvements in the measurement routine resulted in much lower effects of these errors in the final measurements with the split-type spacer grid. This data is assumed to provide reliable insight into the flow field in the entire region of interest. Minor effects of systematic errors on turbulence quantification are expected at the center of the subchannels in the proximity of the mixing vanes.

It should be mentioned that the lower impact of systematic errors observed in the split-type measurements is unlikely to be related to the change in the mixing vanes designs. The LDV measurements conducted by Chang et al. (2014) showed that this spacer-grid design generates higher turbulence and secondary flow intensity than the swirl-type spacer, which would result in a higher proneness to flow-induced errors. Additionally, the flow inside the spacer grid is not affected by the mixing vanes design but also yields significantly lower effects of systematic errors.

Besides changing the imaging method, the m_1^{enc} selection varied between measurement campaigns. For the split-type measurement, twelve velocity sensitivities were acquired, making the RST measurement comparatively time-consuming. Lowering the number of acquired velocity sensitivities reduces the acquisition time, but identifying the ideal m_1^{enc} can be cumbersome without prior knowledge of turbulence intensity.

In the final measurements, m_1^{enc} was identified from prior measurements with fewer averages. Figure 10.2 shows that low qualitative differences arise when calculating the RST using only 50, 25, and 10 of the 200 repetitions in the

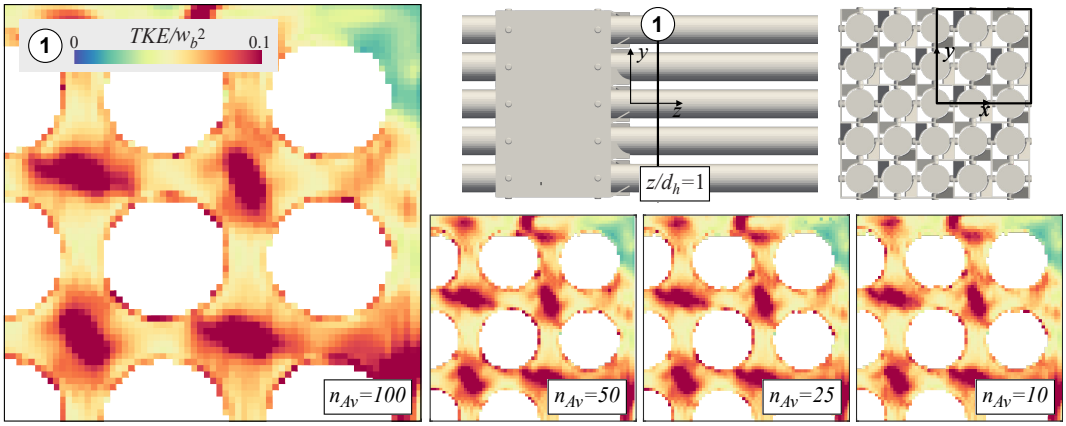

Figure 10.2.: Effect of the number of averages on the results in the RST quantification. The results are obtained by calculating the RST from fewer averages of the measurements with the split-type spacer at $z/dh = 1$.

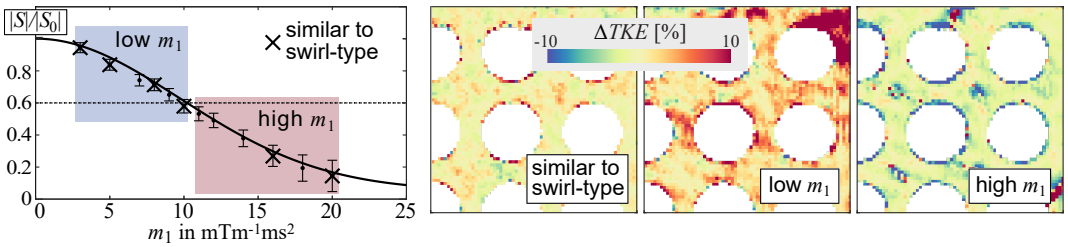

Figure 10.3.: Effect of the selected m_1^{enc} on the turbulence quantification. The results are obtained by omitting data points of the full measurement with the split-type spacer at $z/d_h = 1$. The graph on the left illustrates the fit with 12 m_1^{enc}. On the right, the deviations in the TKE when only half of them are used to calculate the RST are shown. Three cases are considered: similar m_1^{enc} as for the swirl-type spacer (marked with 'X'), only the lowest m_1^{enc} (blue box), and only the highest m_1^{enc} (red box).

full reconstruction. Thus, a measurement with low averages prior to the final measurements assists in the ideal selection of m_1^{enc}. The effect of the chosen m_1^{enc} is illustrated in Fig. 10.3. Here, the relative local difference to the RST quantified from all m_1^{enc} is depicted. Three cases are considered: six of the twelve sensitivities similar to the swirl-type measurements, the six lowest, and the six highest values. The lowest deviations are observed in the first case. Thus, the low accuracy in the swirl-type measurement is mainly driven by flow-induced errors rather than the selection of m_1^{enc}. Substantial variations occur for the other results. The lowest values provide good sensitivity to high turbulence, which results in strong deviations in low-turbulence regions. The turbulent kinetic energy, in this case, appears to be generally overestimated. In contrast, the results calculated from the highest m_1^{enc} yield small deviations in regions of low turbulence but are significantly underestimated in regions of high turbulence intensities, such as in the center of the subchannels. It should be reminded that in the current approach, the highest m_1^{enc} set T_E and, thus, they define the sensitivity to flow-induced errors. Lowering the sensitivity may be reasonable if low turbulent regions are not of great importance.

Compared to the previous studies at the MRI Flow Lab by Schmidt et al. (2020) and John et al. (2022), the reconstruction of the RST was optimized. On the one hand, a weighted least square fit was used in the 3D Gaussian fit. On the other hand, the effect of mean velocity variance inside the voxel was corrected. Both were implemented following the suggestions of Dyverfeldt et al. (2009) and strengthened the reliability of the results. Nonetheless, the changes in the imaging method have a more significant effect on the accuracy of the results.

Part IV.

Synthesis with the Benchmark Study

The previous chapters highlighted the advantages of MRV in providing experimental validation data for nuclear reactor safety studies but also identified possible sources of errors. Several studies have compared experimental results from MRV to data from optical measurements to prove the reliability of this measurement technique. In most studies, the velocity acquisition using conventional Cartesian PC MRI on medical whole-body MRI systems is robust against systematic errors at velocities up to $2\,\mathrm{m\,s^{-1}}$. In contrast, only a limited number of studies have investigated the accuracy of MRV turbulence acquisition in technical applications at high velocity and turbulence levels but also identified regions with a significant influence of flow-induced errors (John et al., 2022; Schmidt et al., 2021b).

Measurements in the fuel assembly model aimed to optimize the experimental setup and the measurement routines to obtain data that is less affected by these errors to meet the requirements of experimental data intended to be used in the validation of numerical methods. In part III, detailed analyses of the measurement results and the possible impact of systematic errors are discussed. The swirl-type spacer measurements suffer from more significant uncertainty and systematic errors. However, regions in which the data provide reliable results are also determined. For the split-type spacer, improvements in the measurement routine and the experimental setup resulted in promising data with an imperceptible influence of systematic errors in most results. A notable bias is here only expected in the proximity of the mixing vanes. To confirm these impressions, this part compares the MRV results with the findings from the initial benchmark study.

In the OECD/NEA-KAERI benchmark study, LDV measurements served to validate the numerical results. The experiments were carried out at KAERI, for which Chang et al. (2014) published all the details on the experiments. The authors state that the LDV data is subject to systematic influences, which are given as 4.8 % to 5.1 % for the velocity components, and a random error between 0.2 % and 1.8 % for the turbulence intensity. The values are normalized to the axial bulk velocity w_{bulk}.

Lee et al. (2014) used this experimental data as a reference to investigate the reliability of CFD results handed in by the participants of the blind benchmark exercise. In this evaluation, the results were ranked based on their agreement with the experimental data in the following metrics:

- time-averaged mean velocity components $\langle \boldsymbol{u} \rangle = [\langle u \rangle, \langle v \rangle, \langle w \rangle]^T$
- time-averaged mean turbulence intensities $\boldsymbol{u}_{rms} = [u_{rms}, v_{rms}, w_{rms}]^T$
- circulation in a single subchannel $\Gamma_z = \int_A \omega_z \mathrm{d}A$

All these parameters are time-averaged metrics and can likewise be provided from the MRV measurements presented in part III. However, the measurement techniques place very different requirements on the experimental setup, which are compared and discussed in chapter 11. Considering these differences, the following chapters compare the outcomes of the MRV measurements with the reference data from the OECD/NEA-KAERI benchmark. This not only proves the reliability of the MRV results but also identifies the substantial benefit MRV measurements can provide in the assessment of single-phase CFD methods.

11. Comparison of the Experimental Methods

MRV and LDV place very different restrictions on the experimental setups arising from their dissimilar measurement principles. The functionality of MRV was introduced in chapter 4. The concept of LDV is only briefly summarized here to highlight the differences to MRV. A more detailed introduction to its functionality is, for example, provided by McKeon et al. (2007). The chapter focuses on the data available from the LDV measurements by Chang et al. (2014), as well as on the differences in the experimental setups resulting from the characteristics of each technique.

11.1. Available Reference Data

LDV is an optical measurement method based on the Doppler effect. In the intersection of two laser beams with monochromatic light, an interference pattern occurs, commonly referred to as fringes. A moving particle passing through this focal point reflects the light with varying intensity. The frequency is directly proportional to the velocity component parallel to the plane of the two laser beams. Thus, LDV is a single-point imaging method, that requires visual access to the flow field and tracer particles added to the flow medium.

Three pairs of laser beams are required to acquire the entire three-component velocity vector. Capturing the time-averaged spatial distribution of the velocity field is only feasible by moving the focus of the laser beams. However, as LDV detects the velocity of several thousands of passing particles individually at a single spatial position, it allows for quantifying further parameters of the turbulent statistics, such as the integral time scale.

Chang et al. (2014) used a dual-beam configuration with a measurement volume of 6.76 mm length and 0.18 mm diameter from which the scattered light of the passing particles is captured. The measurement volume is illustrated in Fig. 11.1**A**. In the proximity of walls, the LDV acquisition is biased, which limited the acquisition in the experimental study of Chang et al. (2014) as illustrated in Fig. 11.1**B**.

Chang et al. (2014) took measurements of the lateral velocities at 4173

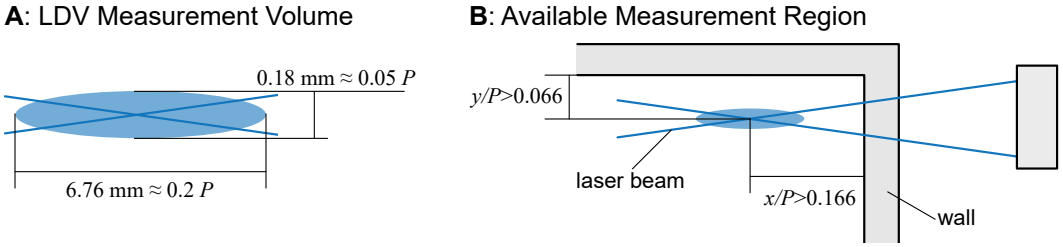

Figure 11.1.: LDV measurements performed by Chang et al. (2014). **A**: indicates the elliptical volume in which LDV is sensitive to particle motion at each measurement position. Due to the shape of the measurement volume, measurement errors arise close to the wall, which limits the near-wall measurements as indicated in **B**.

positions, each being measured for 20 s. They acquired 2000 samples per second in the open flow region and 100 samples per second in the proximity of walls. After each acquisition, the focus of the laser beams was moved to the next measurement position at 0.75 mm increments.

Figure 11.2 compares the resolution of the experimental data from LDV and MRV related to the pitch P of the fuel assembly model. The dotted line indicates the position of the suggested position of the measurement plane. It becomes apparent that LDV has a precise spatial accuracy in the in-plane direction. In contrast, a higher spatial averaging is expected in the through-plane direction due to the length of the spherical volume. Compared to the resolution in the MRV measurements, the distance of the measured data points is lower. The MRV is affected by a stronger spatial averaging in the in-plane direction but has no gaps between the data points.

As LDV requires visual access to the flow field, acquiring the axial velocity components w in the fuel assembly model is limited to the gaps between the rods. The lateral components could be acquired in the entire fuel assemblies but Chang et al. (2014) only captured data in one-eighth of its cross-section at four distances $z/d_h = 0.5, 1, 4, 10$ to the end of the spacer grid mixing vanes.

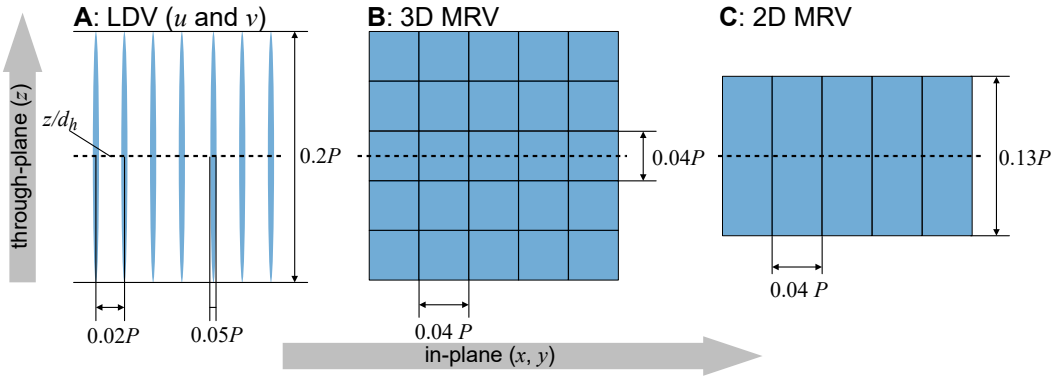

Figure 11.2.: Relative resolution and spatial averaging in LDV (**A**), 3D MRV (**B**), and 2D MRV (**C**) measurements. The dashed line indicates the designated axial position z/d_h.

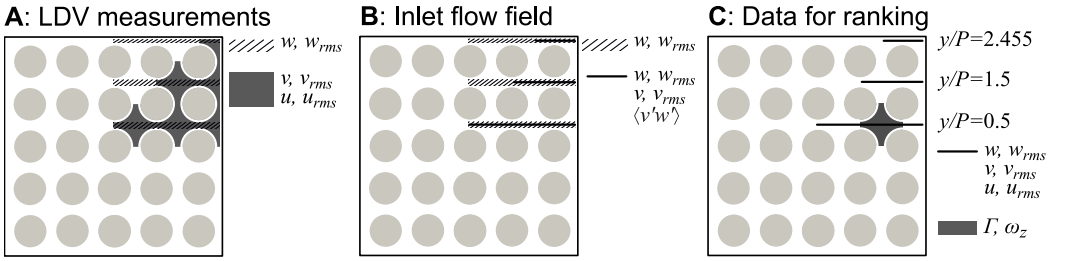

Figure 11.3.: Available data from the initial experimental study on the OECD/NEA-KAERI benchmark. **A**: measurements performed using LDV as described by Chang et al. (2014), **B**: inlet flow conditions provided by NEA (2013), and **C**: data used for synthesis and ranking of the numerical results by Lee et al. (2014)

Furthermore, measurements without the spacer grid were taken to provide the inlet flow conditions.

Figure 11.3**A** illustrates the region of LDV measurements conducted by Chang et al. (2014). From these measurements, the inlet field is provided in NEA (2013), but the data for the lateral components is reduced to the v component in three centerlines at $y/P = 0.5$, $y/P = 1.5$, and $y/P = 2.455$ (see Fig. 11.3**B**). Finally, Fig. 11.3**C** illustrates the data used by Lee et al. (2014) to assess the CFD results. Velocity and turbulence intensities are compared at the three lines mentioned previously, while only the vorticity and circulation are compared for an entire subchannel.

11.2. Experimental Setups

The requirements of the measurement methods result in significant differences in the experimental setups used to quantify the flow inside the fuel assembly models. Figure 11.4 contrasts the different fuel assembly models.

For the LDV measurements performed by Chang et al. (2014), the entire fuel assembly model was manufactured from stainless steel except for the viewing windows required to provide optical access for the laser beams. The axial velocity w was measured from a window at the side, and the lateral components u and v were acquired through a viewing window perpendicular to the fuel assemblies axis at the end of the channel. Due to the latter, the measurement plane is located 10 mm upstream of the end of the fuel assemblies, followed by an outlet manifold. The distance between the measurement plane and outlet manifold corresponds to a relative length of $z/d_h = 0.4$. This also made it necessary to move the spacer grid and the upstream flow straightener to adjust the distance between the end of the mixing vanes and the measurement plane. NEA (2013) and NEA (2022) noted that these outlet conditions are not optimal.

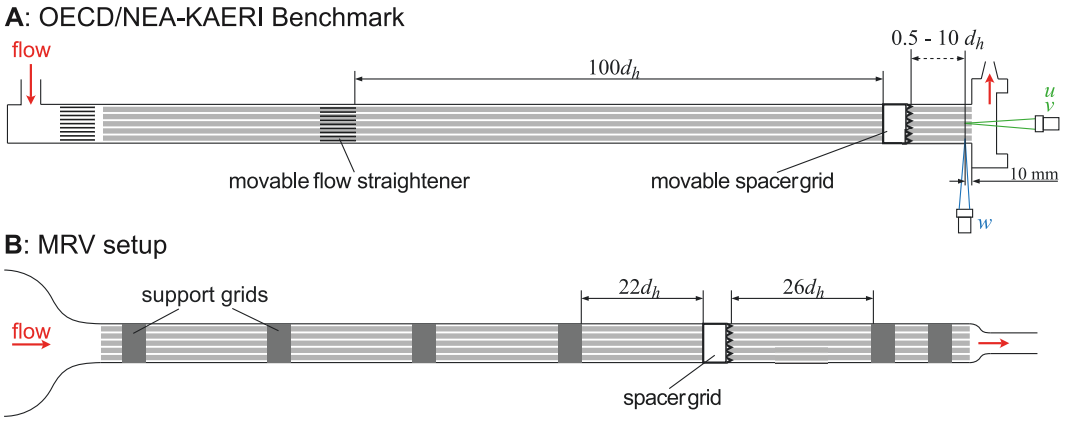

Figure 11.4.: Comparison of the arrangement of the fuel assembly model. **A**: The OECD/NEA-KAERI benchmark study (NEA, 2013; Chang et al., 2014), and **B**: The setup used for the MRV measurements.

In contrast, MRV does not require optical access to the flow field but restricts the used materials. Thus, the fuel assembly is completely manufactured from different plastics. Additional support grids are included in the assembly to prevent the fuel assembly from bending or vibrating. The spacer grids are made from additive manufacturing, which gives the spacer grid a higher surface roughness. In return, the flow behind the spacer grid can develop over a significantly longer distance that remains the same for all measuring positions.

Additionally, the scaling of the models differs. The setup for the MRV measurements was adjusted to find a compromise between relative resolution and bulk velocity. This resulted in a scaling factor of about 2.0 compared to the dimensions in a realistic fuel assembly. For the reference data from LDV, the dimensions are even stronger enlarged. Thus, to compare the results of MRV with the LDV data from Chang et al. (2014), all measured quantities are scaled to the axial bulk velocity w_b, the lateral dimensions are scaled to the pitch P and the axial dimension is scaled to the hydraulic diameter d_h. For the vorticity ω_z this results in

$$\frac{d_{h,LDV}}{w_{b,LDV}}\omega_{z,LDV} = \frac{d_{h,MRV}}{w_{b,MRV}}\omega_{z,MRV} \tag{11.1}$$

12. Comparison of the Measurement Results

The MRV measurements presented in this work aimed to provide experimental data at similar boundary conditions as the LDV measurements conducted for the initial benchmark exercise. Thus, first, the focus is comparing the inlet flow field realized in the different experimental setups. Afterward, the measurements downstream of the swirl- and the split-type spacer grid are compared to the data available from NEA (2013) and Lee et al. (2014). Contour plots are digitized from the publications directly, while data points from graphs are extracted using the Engauge Digitizer Software (Mark Mitchell, 2019).

The comparison will also include some of the numerical results to point out difficulties in assessing CFD methods based on the metrics considered in the benchmark study. The aim is to identify the reliability and the potential of MRV compared to optical measurements such as LDV, not to discuss the most suitable CFD methods. Best practices guidelines for the latter are discussed by Lee et al. (2014). If numerical results are mentioned in the following, their identifiers refer to the designation by Lee et al. (2014) and NEA (2013). Their studies also provide further details on each method, such as the turbulence models, the inlet conditions, and the mesh.

12.1. Upstream Measurements

Detailed upstream flow conditions were provided to all participants of the blind benchmark and released by NEA (2013), which some participants used as inlet conditions in their CFD simulation. The experimental data for the three gap centerlines is provided, as shown in Fig. 11.3. In the LDV measurements, the spacer grid was removed, and the movable flow straightener was placed at $z/d_h = 90$ upstream of the measurement plane, which corresponds to a measurement at $z/d_h = 10$ upstream of the spacer. For the MRV measurements, the whole channel was moved to capture the inlet flow conditions at $z/d_h = 2.3$ upstream of the spacer grid at the scanner's isocenter. For both measurement methods, the inlet flow was acquired at Reynolds number 50 250.

The different outlet conditions are illustrated in Fig. 12.1. The LDV mea-

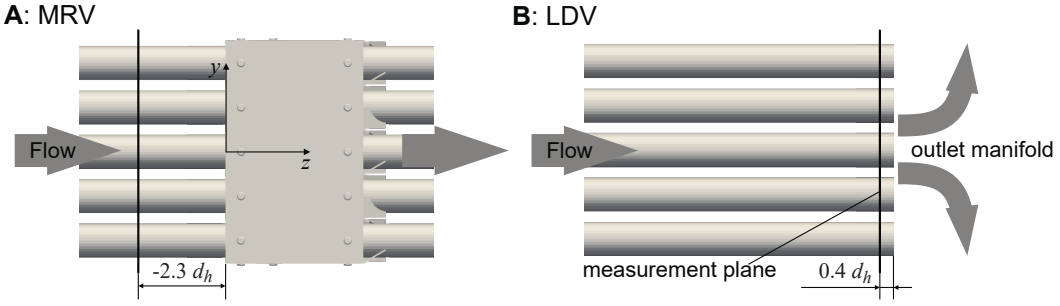

Figure 12.1.: Position of the measurement plane to acquire the inlet flow field in MRV and LDV.

surement plane is at a distance of $z/d_h = 0.4$ towards the outlet manifold. According to the NEA (2013), moving the measurement plane up to a distance of 40 mm ($z/d_h = 1.6$) to the outlet has no significant effect on the captured flow. Thus, the MRV measurements at a distance of $z/d_h = 2.3$ to the beginning of the spacer grid should be sufficient to capture the undisturbed upstream flow field.

Figure 12.2 compares the results of both measurement techniques in the centerline of a rod gap at $y/P = 0.5$. The results generally compare well, but some minor deviations are apparent. The lateral component v shows slightly negative values in the LDV results, while for the MRV, it is distributed around zero within the measurement's uncertainty. Further deviation occurs in the axial velocity w. Here, the results of the third gab located between the last layer of rods and the channels wall are additionally depicted to show that the axial velocity in the LDV results seem to increase towards the center of the fuel

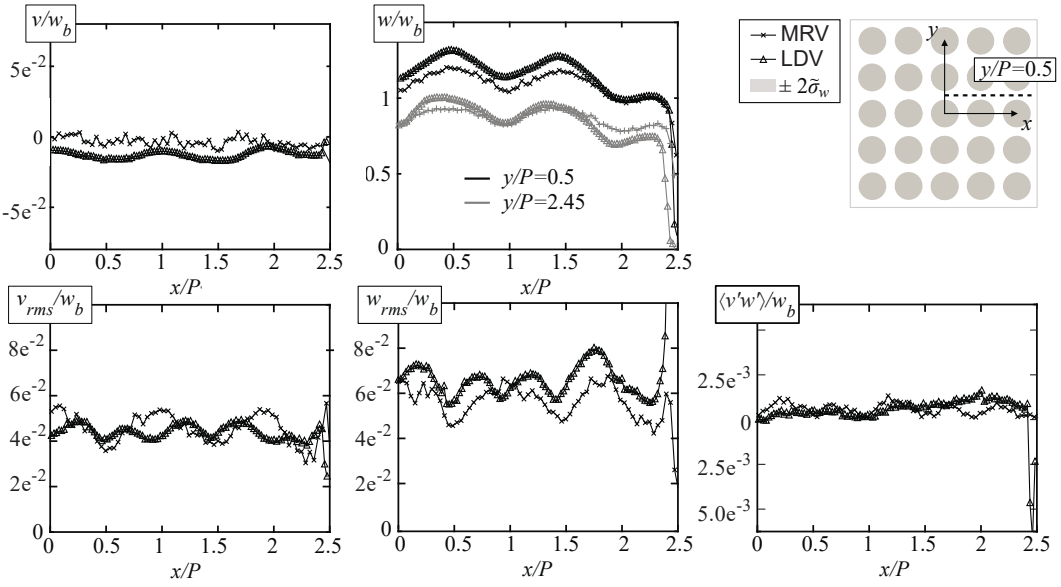

Figure 12.2.: Inlet flow field acquired by MRV and LDV. The MRV data was captured at $z/d_h = 2.3$ upstream of the spacer grid, and the LDV data corresponds to a distance of $z/d_h = 10$ to the spacer grid.

assembly. Both profiles align perfectly for the third centerline at $y/P = 1.5$, which is not shown for clarity.

Regarding turbulence, both techniques yield a higher axial velocity intensity than the lateral component. A minimum of turbulence intensities is equally captured in the subchannel at $x/P = 0.5$ and $x/P = 1.5$, but deviations occur in the gaps between the subchannels at $x/P = 1$ and $x/P = 2$, where MRV detects an increase and LDV a decrease of turbulence intensity.

Despite these minor differences, both upstream flow fields are similar without any significant flow statistics likely to affect the comparability of the results downstream of the spacer grid.

12.2. Swirl-Type Spacer

The MRV results considered in the following are obtained from the 2D MRV measurements of the mean velocity vector and Reynolds stress tensor, as the 3D measurements were captured at Reynolds number 38 570 instead of 50 250. First, the vorticity and the circulation in a single subchannel are considered, see Fig. 12.3. The contour plots of the LDV measured vorticity, and the data in the circulation plot are digitized from NEA (2013).

The vorticity reveals the core of the vortex created behind the spacer grid, which is centralized in the subchannel at all measured planes. This behavior was captured in both experimental studies. Additionally, at the positions close to the spacer grid, both measurement methods capture slightly positive vorticity towards the rods. However, the LDV data show a more circular shape of the vortex core, while the MRV data yields a more elliptical shape. Similar variations can be observed in the numerical results, for example, for the results of an LES simulation with the identifier *Sw02* displayed in the circulation plot. With further distance to the spacer, these differences vanish.

In terms of circulation, also depicted in Fig. 12.3, the experimental results compare well. The gray elements in the graph illustrate selected CFD results presented by NEA (2013). *Sw02* modeled the downstream flow using LES and is among the top-ranked methods when comparing the mean velocity profiles at the centerline. *Sw04* gets a lower ranking for the velocity profiles but appears to predict the flow field in the entire subchannel much better. The contour plot given by NEA (2013) for the vorticity distribution indicates that *Sw02* predicts secondary flow structures with positive vorticity close to the rods, which is neither captured by the experiments nor by the CFD simulation *Sw04*. This indicates the discrepancy between the rankings of numerical results based on single 1D profiles or taking 2D distributions into account.

The profiles of mean velocity components and turbulence intensities are com-

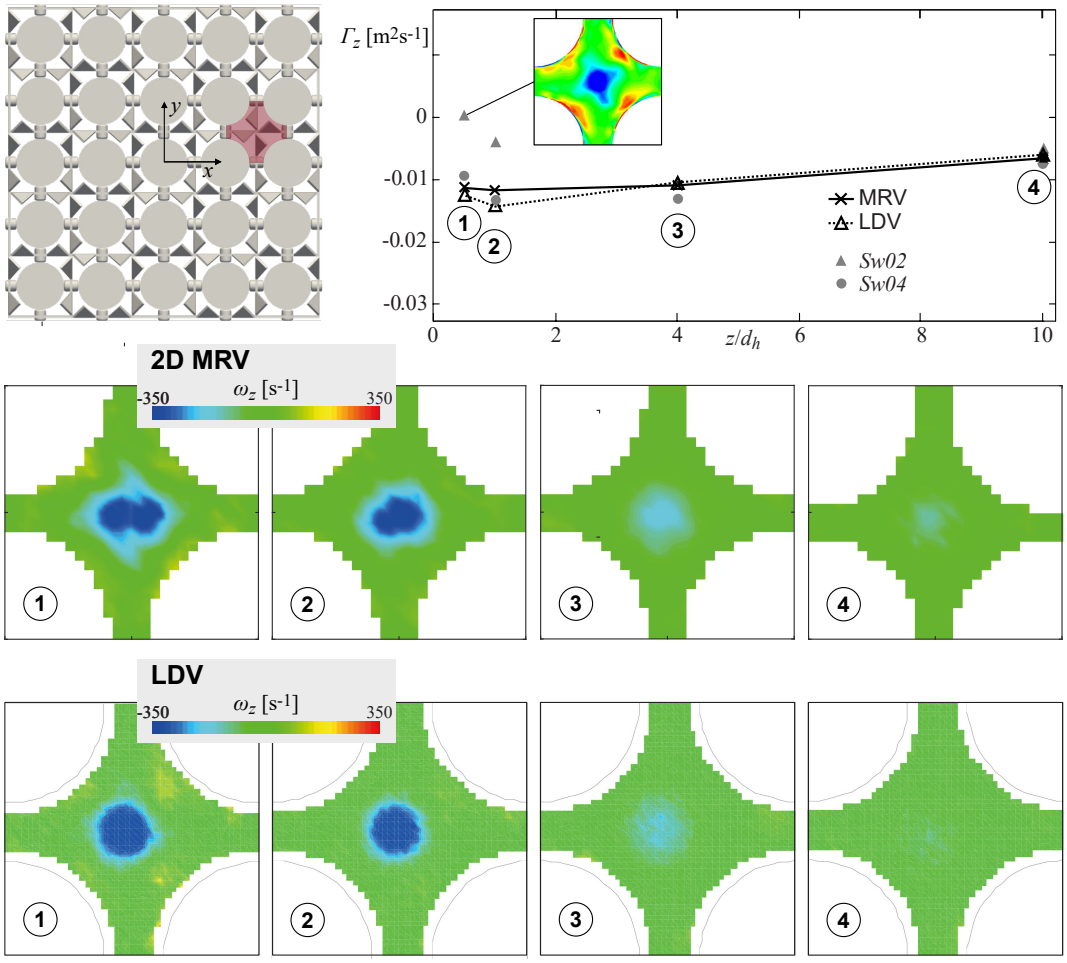

Figure 12.3.: Vorticity and circulation in a single subchannel downstream of the swirl-type spacer grid. Results are calculate from the 2D MRV data. The LDV results, the numerical data, and the contour plots originate from NEA (2013).

pared in Figs. 12.4 and 12.4 at $z/d_h = 1$ and $z/d_h = 4$, respectively, with the LDV and CFD results published by Lee et al. (2014). The results obtained from three LES-based CFD methods (*Sw02, Sw07, Sw12*) that reached the highest rankings in terms of mean velocity are summarized in the gray area. For the velocity, both measurement results agree well. Deviations in the u component arise from the higher spatial averaging in the MRV data. As expected from the analyses of the measurement accuracy in MRV in chapter 8.2, the turbulence quantification shows higher deviations to the reference data, especially towards the center of the subchannels. Furthermore, some data points in the gaps between the subchannels step out significantly, for example, w_{rms} at $z/d_h = 1$. The latter can be attributed to difficulties in the Gaussian fit arising from the chosen m_1^{enc}. In contrast, the differences in the subchannels arise from the poor SNR due to higher orders of motion. Nonetheless, the level of turbulence is captured quite similarly with some overestimation from flow-induced errors, while some CFD methods have underestimated the turbulence

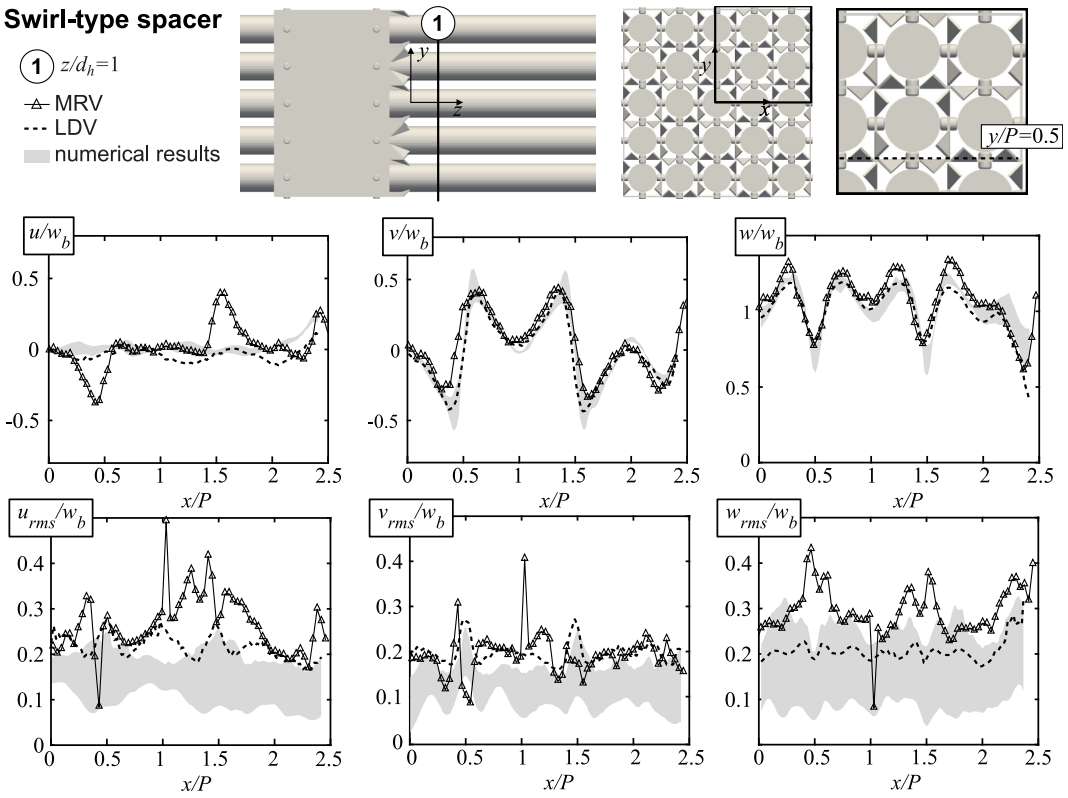

Figure 12.4.: Comparison of MRV with the results published by Lee et al. (2014) in the swirl-type configuration at $z/d_h = 1$ in the gap centerline $y/P = 0.5$.

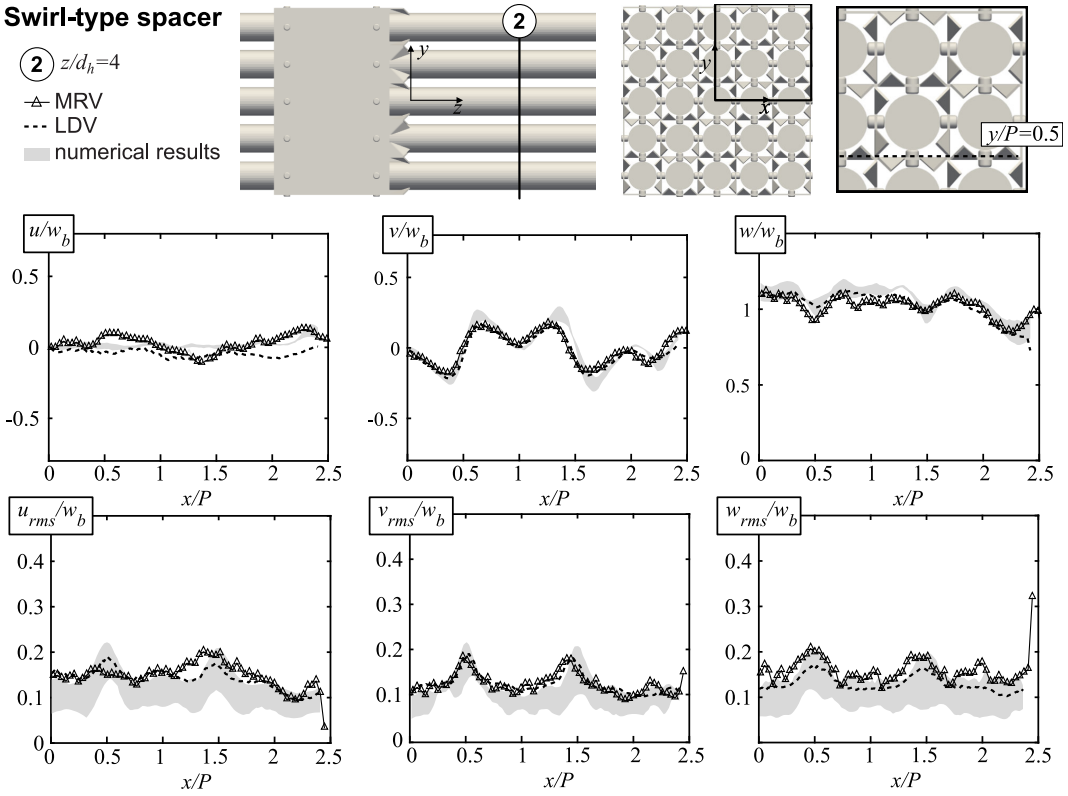

Figure 12.5.: Comparison of MRV with the results published by Lee et al. (2014) in the swirl-type configuration at $z/d_h = 4$ in the gap centerline $y/P = 0.5$.

significantly. However, at this distance to the spacer grid, the MRV data does not appear similarly reliable as the LDV results to rank the CFD methods in terms of turbulence statistics.

With further distance to the spacer grid, the turbulence and the secondary flow intensity decreases, resulting in a lower impact of systematic errors in the MRV measurements. Thus, the data is in significantly better agreement with the reference data, as shown in Fig. 12.5. Deviations in the velocity profiles can be again attributed to the differences in spatial resolution and spatial averaging. In terms of turbulence, the best agreement is observed for v_{rms}. The other components suffer from slight overestimation but generally capture the turbulence intensity well. Again, some CFD methods tend to significantly underestimate the turbulence, which can be detected reliably by both experimental techniques at this distance to the spacer.

12.3. Split-Type Spacer

In the initial benchmark exercise, the majority of participants (22 of 25) handed in results for this type of spacer grid. It was recommended to address this design if one wishes to submit results for only one of the spacer grid designs (NEA, 2013). In the MRV measurements, data downstream of the spacer grid design was acquired after the measurements with the swirl-type spacer grid. This led to some improvements in the experimental setup and the measurement routine. The results are expected to have an increased accuracy. In the following, the results of the 3D mean velocity field and the 2D turbulence quantification is considered, which both are acquired at Reynolds number 50 250.

Figure 12.6 shows the results of vorticity and circulation of the MRV measurements and the LDV and CFD reference data proposed by NEA (2013). The vorticity distribution and the elliptic shape of the vortex inside the subchannel centered at $x/P = 1.5$ and $y/P = 0.5$ compares well with the reference study. Furthermore, both measurement techniques capture the off-center migration of the vortex with further distance to the spacer grid, but it appears that MRV detects a more rapid decay of the vortex. Please note that MRV results at $z/d_h = 9.7$ are compared to the LDV data at $z/d_h = 10$.

However, close to the mixing vanes, the tilt of the vortex core differs, and MRV captures some stronger positive vorticity off the subchannel center. Thus, the circulation inside the subchannel is lower, as shown in Fig. 12.6. The range of four top-ranked CFD results (three RANS, one LES) is also depicted. NEA (2013) pictured the result of the LES simulation (*Sp15*) to show that the prediction of strong secondary flow structures with positive vorticity results in an underestimation of the circulation inside the subchannel. Interestingly, the

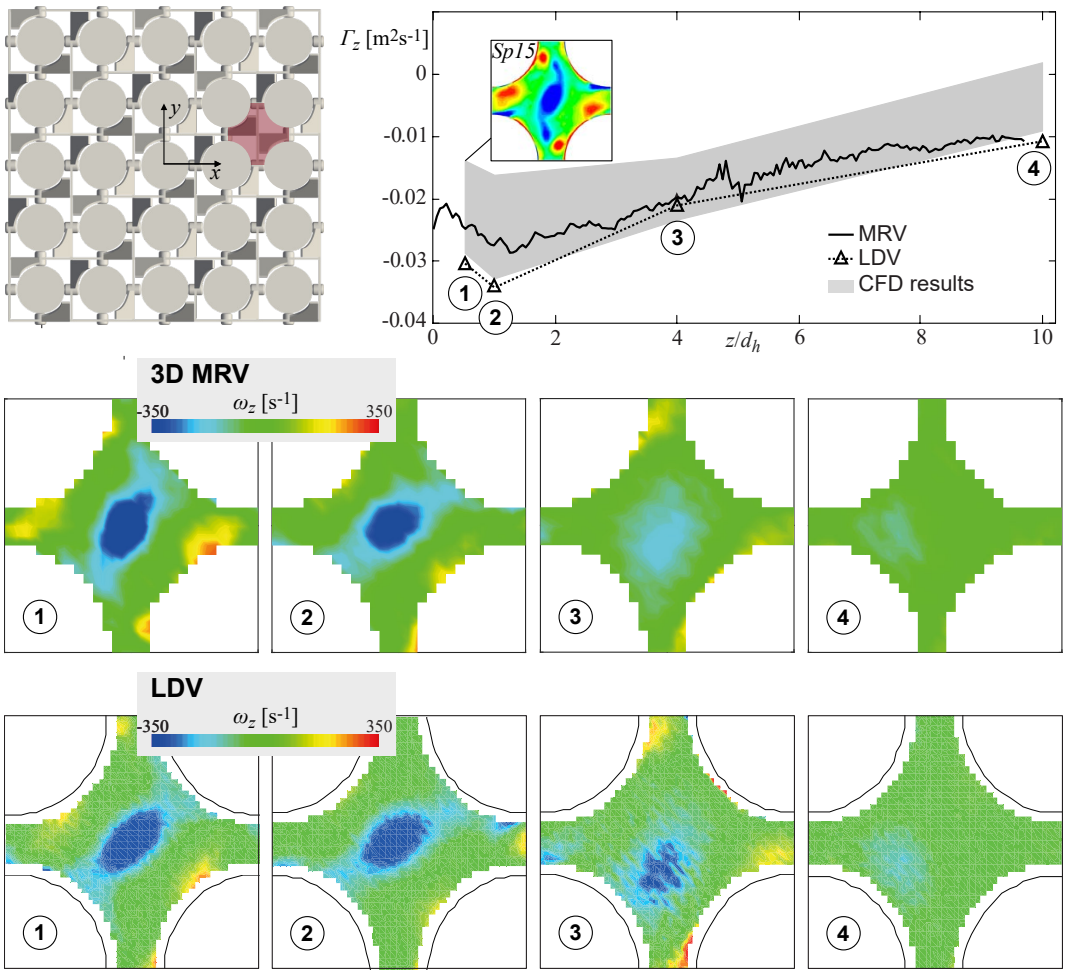

Figure 12.6.: Vorticity and circulation in a single subchannel downstream of the swirl-type spacer grid. Results are calculate from 3D MRV data. The LDV results, the numerical data, and the contour plots originate from NEA (2013).

tilt of the swirl's core and the regions of high positive vorticity compares well with the MRV results.

As for the swirl-type spacer grid, the circulation obtained from the different CFD methods yields that the ranking based on the centerline mean velocity profiles is not correlated to the accuracy in the entire subchannel. The deviations in the experimental methods may result from the different spatial averaging along the axial direction. Still, the swirl generation in the LDV measurements may also be affected by the proximity of the outlet manifold, especially when measuring shortly downstream of the mixing vanes.

Comparison of the velocity and turbulence intensities in the centerline at $y/P = 0.5$ is based on the data published by Lee et al. (2014). The numerical results of the five top-ranked CFD methods (four RANS, one LES) are again summarized in the gray area. Figure 12.7 shows the results at $z/d_h = 1$, which yield a good agreement between the experimental results even in terms of turbulence quantification. This confirms the observations regarding the

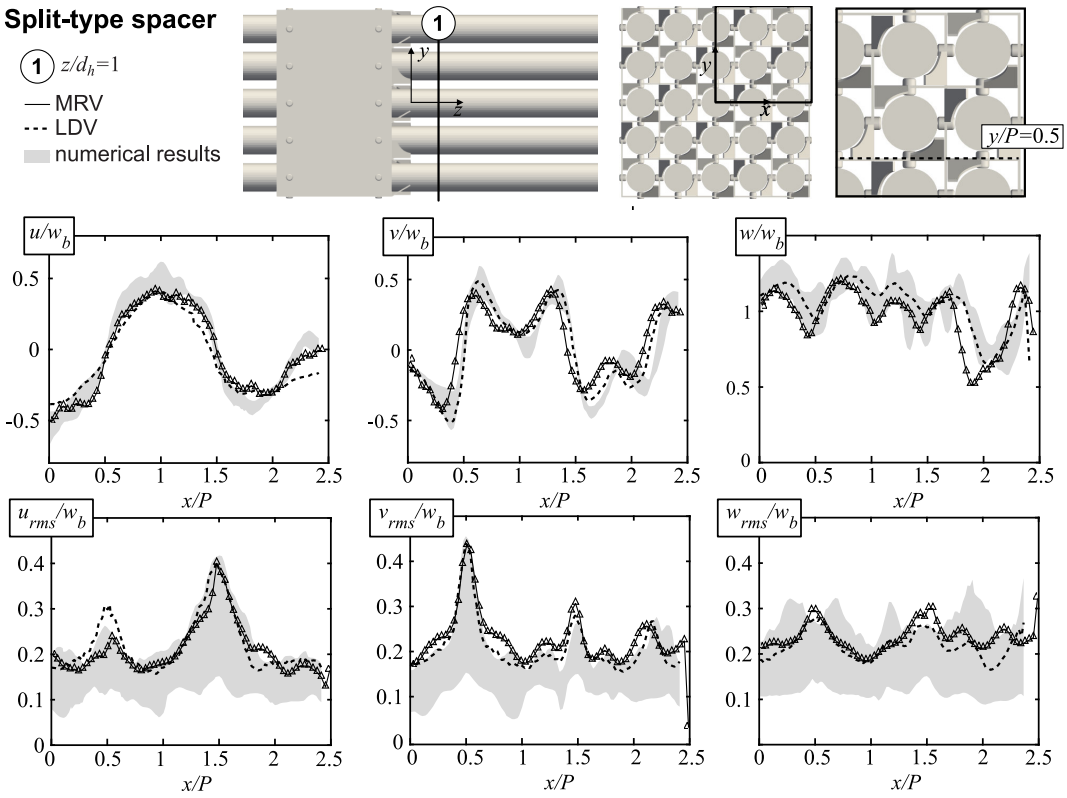

Figure 12.7.: Comparison of MRV with the results published by Lee et al. (2014) in the split-type configuration at $z/d_h = 1$ in the gap centerline $y/P = 0.5$.

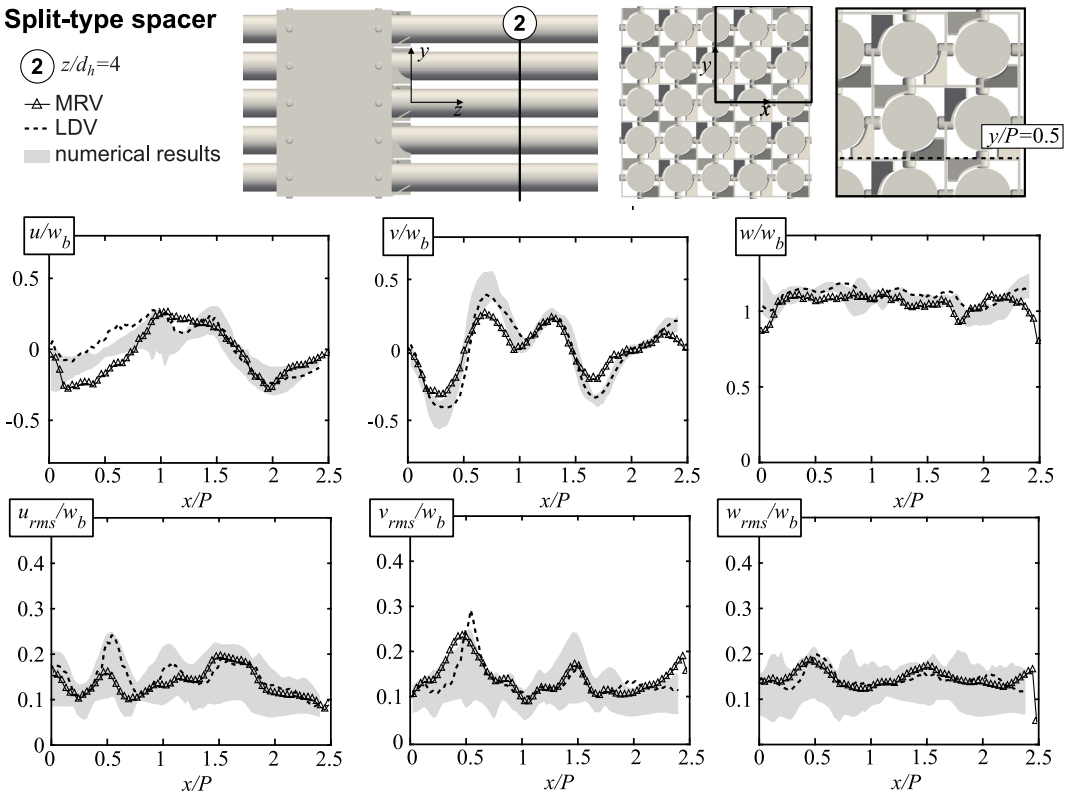

Figure 12.8.: Comparison of MRV with the results published by Lee et al. (2014) in the split-type configuration at $z/d_h = 4$ in the gap centerline $y/P = 0.5$.

reduced influence of systematic errors in the MRV measurements described in chapter 9. As for the swirl-type spacer, some numerical results significantly underestimate the turbulence intensity, which can be identified reliably by both experimental techniques.

In addition, the comparison of CFD methods and LDV in the benchmark study identified an interesting behavior for the lateral velocity u. All of the top-ranked CFD methods predict the velocity peaks of the lateral velocity u in the subchannels at $x/P = 1$ and $x/P = 2$ quite well but also found a third peak near the channel wall that is not covered by the LDV measurements. However, Fig. 12.7 shows, that this peak is also captured in the MRV results. A possible reason for this deviation in the experimental methods is the outlet manifold required in the LDV measurements. In additional LDV measurements with variable distances between the outlet and the measurement plane, minor effects on the flow field were observed (NEA, 2013). Thus, it can be expected that the MRV results are more reliable at this point.

For the sake of completeness, Fig. 12.8 illustrates the comparison of the velocity and turbulence intensities at the centerline at $y/P = 0.5$ at $z/d_h = 4$. Due to the decreased secondary flow and turbulence intensity, a good agreement between the experimental method was already observed at this distance in the spacer grid in the swirl-type spacer measurements. Unsurprisingly, the improved measurements with split-type spacers show a better agreement with the reference data, despite some deviations arising from the differences in the spatial averaging in the different experimental methods.

13. Conclusion of the Comparison with the Benchmark Study

The comparison of the results obtained from the MRV measurements to the data available from the initial OECD/NEA-KAERI benchmark study highlights the reliability and the performance of MRV in terms of producing experimental data in nuclear reactor safety studies. First, it reveals the impact of systematic errors, as discussed in chapter 9 and 8 is correctly identified. In the case of the swirl-type spacer, turbulence quantification shortly downstream of the spacer grid is significantly influenced by these errors, but measurements at $z/d_h = 4$ yield a good agreement with the reference data. Similarly, it was described in chapter 9 that the measurements are expected to provide reliable data at both distances to the spacer grid with some minor effects of systematic errors in the subchannel centers. This also corresponds to the observed agreement between LDV and MRV.

Second, the MRV measurements provide experimental data without requiring complex outlet conditions as necessary in the LDV measurements. The LDV measurements are acquired at 10 mm distance to the outlet manifold, and the distance between the measurement plane and the outlet needs to be adjusted for each measurement position. The comparison with MRV yields some regions in the measurement that may be affected by the outlet condition.

Furthermore, it was noted in the synthesis of the CFD and LDV results that the ranking yields some very different results depending on the used metrics (Lee et al., 2014). Where the centerline comparison of velocity and turbulence intensity showed good agreement, the vorticity and circulation in an entire subchannel may draw a completely different picture. Additionally, the later metrics are cumbersome to quantify, as LDV cannot provide data near walls. Equally, in MRV, these voxels are affected by partial volume effects, making an exact determination of the fuel assembly's geometry challenging.

The advantage of MRV is its capability to provide the entire flow field inside the channel's cross-section or even a whole 3D volume at a low experimental cost. Thus, data matching routines such as those proposed by Wüstenhagen et al. (2021) can be used to get a more comprehensive picture of the agreement

between numerical and experimental results than using only 1D profiles or the data from an individual subchannel. A similar assessment of CFD methods used in the design of turbine blade cooling systems has already demonstrated this approach when comparing different CFD methods (Bruschewski et al., 2022; Wüstenhagen et al., 2023).

Additionally, MRV can provide experimental data in a comparatively short time. Chang et al. (2014) acquired the lateral velocities using LDV in 4173 data points. Each position being measured for 20 s results in a minimum acquisition time of more than 23 h. In contrast, velocity and turbulence measurements using MRV resulted in more than 7000 voxels in the fluid-filled volume. The data was captured in 6.5 hours and holds all components of the mean velocity vector and whole the Reynolds stress tensor. Additionally, 3D measurements provide more than 3 million velocity vectors from shortly upstream, up to $z/d_h = 10$ downstream of the spacer grid within a few hours.

The comparison with the OECD/NEA-KAERI benchmark study yields that MRV provides reliable data for assessing CFD methods in fuel assembly models of pressurized water reactors. MRV provides the entire mean velocity vector and all six components of the Reynolds stress tensor from wider regions of interest at a significantly shorter acquisition time and with lower experimental cost. Additionally, combining automatic data matching routines provides new possibilities in validating CFD methods.

Part V.

Conclusion

14. Summary

This thesis aimed to provide more comprehensive experimental data for the assessment of CFD methods for NRS problems. Previous studies had identified the potential of this measurement technique but also the substantial effects of systematic errors that reduced the accuracy of the measurement results. Compared to conventionally used optical measurement methods, MRV provides all components of the velocity vector and the Reynolds stress tensor in an entire 2D or 3D region of interest at a comparatively short time and without the need for optical or physical access to the flow field. Identification and reduction of measurement errors in current MRV methods is therefore urgently required to exploit the full potential of this measurement technology.

An MRV-compatible replica of the OECD/NEA-KEARI benchmark was set into operation to perform MRV measurements at conditions relevant for NRS problems. This test case was selected as it provides a generic design and reference data from LDV to prove the reliability of MRV. The reduction of systematic errors in MRV was already taken into account with the design of the experimental setup. On the one hand, the materials used in the proximity of the measurements have a similar magnetic susceptibility to the flow medium to avoid systematic errors from magnetic field imperfections. On the other hand, the dimensions of the fuel assembly model were chosen to find a compromise between relative resolution, required flow rate, and flow velocity. Lowering the latter is relevant to minimize the sensitivity towards motion-induced errors.

Substantial differences to the initial setup used to provide LDV reference data for the evaluation of CFD methods in the initial benchmark study illustrated the advantages of MRV over optical measurement methods: The distance between measurement region and outlet is significantly increased, and the outlet manifold is avoided, which simplifies the outlet conditions and meet a concern that was raised by the participants of the benchmark study.

MRV measurements were performed based on Cartesian PC MRI with 4-point encoding to acquire the velocity and ICOSA6 encoding with multiple m_1^{enc} to quantify the RST. In the first commissioning of the experimental setup with the swirl-type spacer grid installed in the fuel assembly model, the same imaging routine as has been validated in an earlier study was used in a previous study by (Schmidt et al., 2020). As it was expected, a significant impact of

errors, in particular, due to higher orders of motion, became apparent. This limits the region of low systematic errors to the flow region downstream of the spacer grid, similar to the study by Bruschewski et al. (2021b). In terms of turbulence quantification, the measurement in the proximity of the mixing vanes at $z/d_h = 1$ was substantially affected by errors making the data not feasible for the assessment of CFD methods. These findings stressed the need to improve MRV further to increase its accuracy in this application. In a final measurement campaign with the split-type spacer, improvements in the imaging routine and a more precise selection of the m_1^{enc} significantly enhanced the measurement results.

These optimizations and the developments compared to the imaging routine proposed by Schmidt et al. (2021b) are summarized in the following section, followed by an evaluation of the objectives of this thesis.

14.1. Improvements Compared to Earlier Studies

The methods to quantify velocity and turbulence statistics used in earlier studies at the MRI Flow Lab by Bruschewski et al. (2021b) and Schmidt et al. (2020) were the starting point for the acquisition of flow parameters in the replica of the OECD/NEA-KEARI benchmark. This thesis focused, in particular, on improving the measurements of the RST, as substantial deviations from optical reference measurements were observed in these previous works.

In general, the post-processing of the turbulence measurement was improved. A weighted least square fit, instead of a threshold, was implemented in the 3D Gaussian fit to minimize the impact of random errors, and the effect of mean velocity variance was corrected. Both approaches build on the suggestions by Dyverfeldt et al. (2009). However, they are not assumed to be the most significant in affecting the accuracy of the measurements.

The most substantial errors resulted from the sensitivity to higher orders of motion. These caused a significant signal attenuation inside the spacer grid and the subchannel centers in the measurements with the swirl-type mixing grid where a similar measurement method as proposed by Schmidt et al. (2020) was used. The effect of these errors was greatly reduced by changing the encoding from ECHO to FAST to shorten the gradient waveform and by using an asymmetric echo to further reduce T_E. As a result, not only the turbulence measurements are much less affected by systematic errors, but also the 3D mean velocity measurement improved significantly.

The Cartesian PC MRI with FAST encoding and an asymmetric echo used in the final measurements allowed for reducing the T_E to 1.3 ms for the 3D measurement. This is close to what can be achieved with SYNC SPI or radial

imaging, and the method used here provides the data in a feasible acquisition time and without complex image reconstruction. The smearing resulting from asymmetric data collection was found to be less relevant to the quality of the results.

14.2. Conclusion on the Objectives of this Thesis

The impression of the enhanced accuracy achieved through the improvements in the imaging routine was manifested in the comparison to the results from the initial benchmark study. The results were compared at $z/d_h = 1$ and $z/d_h = 4$. For the velocity, both measurements yielded a good agreement with the reference data, as the most significant effects of systematic errors appear closer to the spacer grid. The improvement in the RST measurement were much more evident. For the commissioning, significant deviations in the turbulence intensities were obtained at $z/d_h = 1$. The agreement improved with further distance to the spacer grid, but the results appeared noisy, which is assumed to arise from the poorly chosen m_1^{enc}. In contrast, the results for the split-type spacer obtained with the improved imaging routine appeared much smoother and yielded a better agreement with the reference data. Accordingly, the objectives of this study defined in chapter 1 are met as follows:

- The results of the split-type spacer grid provides comprehensive data with low impact of errors for the future validation of CFD methods. The 3D3C enables a full-filed validation of the mean velocity field, and the acquired RST enables evaluation of the evolution of turbulence in the fuel assembly model.

- Comparatively small changes of a conventional PC MRI with robust Cartesian sampling enabled significant improvements in the measurement results and provided reliable data for the validation of CFD methods. Thus, reliable results can be obtained in these applications without requiring time-consuming SYNC SPI or more complicated non-Cartesian imaging.

- The significant agreement of the acquired turbulence with the LDV reference data in the final measurement campaign indicates the reliability of MRV to quantify turbulent statistics. It was found that the performance of the Gaussian fit yields an estimator for the effect of systematic errors on the results.

15. Outlook

The improvements achieved in this thesis are a starting point to strengthen the position of MRV as a reliable method to provide experimental data for the evaluation of CFD methods applied in single-phase NRS problems. Best practice methods are currently elaborated to provide the data to a wide range of users. Moreover, the experimental setup commissioned within this thesis enables further measurements in industrial-relevant fuel assembly designs. Having improved the accuracy of MRV, the previously discussed amount of data can be acquired in three days for a single design. Including assembling the setup, experimental results, as presented in this thesis, can be provided within one week. In these future measurements, minor improvements in the precise acquisition of the inlet flow conditions are desirable to entirely meet the requirements on CFD-grade experiments defined by NEA (2022). This mainly concerns the position of the temperature and pressure probes to be closer or within the FOV.

Additionally, various other applications of MRV in NRS problems have already been identified. Especially the application in multi-phase flows is of great interest, as the extension of CFD methods in this context intended NEA (2014).

To rule out the possibility that the good agreement of the results for the split-type spacer is due to the different experimental setups, a measurement campaign is planned in which the measurement method will be validated on the same setup as done by Schmidt et al. (2020). Additionally, further optimization of MRV turbulence quantification is desirable regarding the dynamic range, the quantification of systematic errors, and the acceleration of the measurements.

In the current method used to quantify the RST, the highest m_1^{enc} defines the timing parameter of the sequence. In applications with highly non-uniform turbulence, this results in a compromise for the measurement accuracy: T_E and the proneness to flow-induced errors increases when the maximum m_1^{enc} is raised to achieve a reasonable sensitivity in regions of low turbulence. Accordingly, decreasing m_1^{enc} reduces systematic errors but also lowers the accuracy at low turbulent regions. Therefore, the practicability of other techniques to increase the dynamic range will be investigated.

Moreover, a more precise method to quantify the uncertainty in the RST

quantification is desired. The estimator based on the background noise, as used in this study, yielded high values which did not reflect the observed smoothness of the data. An alternative is determining the random error from the statistics inside the ROI. More importantly, suitable methods to process this uncertainty through the weighted least square fit are favorable. These approaches are expected to increase the required computational power significantly but will provide a more reliable assessment of the measurement uncertainty. Additionally, methods to recover the partially sampled k-space in the asymmetric readout are investigated to reduce the smearing observed in the readout direction.

Finally, acceleration of the measurements to enable 3D acquisition of the RST is favorable as this would further extend the data available for CFD validation. Possible methods include the implementation of parallel imaging and highly undersampled non-Cartesian imaging routines.

In conclusion, it is undeniable that MRV has demonstrated its dependability in non-medical applications, such as fuel assembly models. This measurement technique can significantly aid in evaluating CFD methods, particularly in settings where optical methods are challenging. The impressive capabilities and precision achieved over the past decades and within this thesis strengthen its relevance in engineering flow analysis. However, it is also essential to note that there are still capabilities to be further investigated, signifying that it is a measurement method that will continue to progress.

List of Figures

List of Tables

Nomenclature

Mathematical Operators

$(...)^*$	complex conjugate
$(...)^{-1}$	inverse
Δ	absolute difference
$\angle$	complex angle
$\exp(...)$	exponential function
$\langle ... \rangle$	average
$[...]^T$	transposed matrix
$\ln(...)$	natural logarithm
∇	nabla operator
$\lvert ... \rvert$	absolute value
FT	Fourier transform

Latin Characters

A	area
$\boldsymbol{a}$	acceleration
B	magnetic field strength
B_0	strength of the static magnetic field
d_h	hydraulic diameter
$\boldsymbol{G}$	magnetic field gradient
$\boldsymbol{g}$	linear velocity gradient
$\boldsymbol{k}$	spatial frequency
$\boldsymbol{k}_v$	velocity sensitivity
M_0	spins initial bulk magnetization
$M_{x,y}$	spins bulk magnetization perpendicular to B_0
$\boldsymbol{m}_0$	0th gradient moment
$\boldsymbol{m}_1$	1th gradient moment
m_1^{enc}	velocity encoding

$\boldsymbol{m}_n$	n-th gradient moment
N	Noise
n	number
P	Pitch
p	coil sensitivity
Q	flow rate
Q_{crit}	Q-criterion
R	autocorrelation function
R_a	mean surface roughness
Re	Reynolds number
r	residuum
S	measurement signal
s	shift in time
S_0	signal of reference measurement
SFI	secondary flow intensity
T	integral time scale
T_1	spin-lattice relaxation time
T_2	spin-spin relaxation time
T_2^*	effective T_2, including magnetic field imperfections
T_E	echo time
TKE	turbulent kinetic energy
T_R	repetition time
t	time
t_G	duration of bipolar gradient
$\boldsymbol{u}$	velocity vector
$\langle \boldsymbol{u} \rangle$	mean velocity
$\boldsymbol{u}'$	velocity fluctuations
u	lateral velocity component
u_{abs}	absolute velocity
u_{rms}	lateral turbulence intensity
$\langle u_i' u_j' \rangle$	mean velocity
v	lateral velocity component
v_{enc}	velocity encoding
v_{rms}	lateral turbulence intensity
W	weighting function
w	axial velocity
w_{rms}	axial turbulence intensity
w_b	bulk velocity
$\boldsymbol{x}$	position vector

Greek Characters

δ	error
μ	dynamic viscosity
ν	kinematic viscosity
ρ_s	spin density
ρ	density
$\tilde{\sigma}$	uncertainty
σ	standard deviation
$\boldsymbol{\tau}$	Reynolds stress tensor
θ	temperature
Φ	phase angle
$\boldsymbol{\Omega}$	rotation of the vector field
ω_L	Lamor frequency
ω_z	axial vorticity
$\boldsymbol{\omega}$	vorticity tensor
Γ	circulation
γ	gyromagnetic ratio

Acronyms

1D	one-dimensional
2D	two-dimensional
3C	three-component
3D	three-dimensional
6C	six-component
BWT	bandwidth time product
CAD	computer aided design
CANDU	Canada Deuterium Uranium
CFD	computational fluid dynamics
ECHO	encoding with controlled displacement
ESPIRIT	eigenvalue approach to autocalibrating parallel MRI
FAST	encoding for fast gradients
FE	frequency encoding
FOV	field of view
GRE	gradient echo
ICOSA6	six-directional icosahedral flow encoding
k-space	matrix of spatial frequencies $\boldsymbol{k}$
KAERI	Korea Atomic Energy Research Institute

LDV	laser Doppler velocimetry
LES	large-eddy-simulation
MATiS-H	experimental setup in Chang et al. (2014)
MRI	magnetic resonance imaging
MRV	magnetic resonance velocimetry
NEA	Nuclear Energy Agency
NRS	nuclear reactor safety
OECD	Organisation for Economic Co-Operation and Development
PC MRI	phase-contrast magnetic resonance imaging
PE	phase encoding
PIV	particle imaging velocimetry
PWR	pressurized water reactor
RANS	Reynolds-averaged-Navier-Stokes
rf-pulse	radio frequency pulse
RO	read out
ROI	region of interest
RST	Reynolds stress tensor
SNR	signal-to-noise ratio
SOS	sum-of-squares
SS	slice selection
SYNC SPI	single point imaging with synchronized encoding

Bibliography

Aja-Fernandez, S., Alberola-Lopez, C., and Westin, C.-F. (2008). Noise and signal estimation in magnitude mri and rician distributed images: A LMMSE approach. *IEEE Transactions on Image Processing*, 17(8):1383–1398.

Bernstein, M. A., King, K. F., and Zhou, X. J. (2004). *Handbook of MRI pulse sequences*. Elsevier.

Bernstein, M. A., Shimakawa, A., and Pelc, N. J. (1992). Minimizing te in moment-nulled or flow-encoded two-and three-dimensional gradient-echo imaging. *Journal of Magnetic Resonance Imaging*, 2(5):583–588.

Bonn, D., Rodts, S., Groenink, M., Rafaï, S., Shahidzadeh-Bonn, N., and Coussot, P. (2008). Some applications of magnetic resonance imaging in fluid mechanics: complex flows and complex fluids. *Annual Review of Fluid Mechanics*, 40(1):209–233.

Brown, R. W., Cheng, Y.-C. N., Haacke, E. M., Thompson, M. R., and Venkatesan, R. (2014). *Magnetic Resonance Imaging: Physical Principles and Sequence Design*. John Wiley & Sons, Ltd.

Bruschewski, M., Flint, S., and Becker, S. (2021a). Magnetic resonance velocimetry measurement of viscous flows through porous media: Comparison with simulation and voxel size study. *Physics*, 3(4):1254–1267.

Bruschewski, M., Freudenhammer, D., Buchenberg, W. B., Schiffer, H.-P., and Grundmann, S. (2016a). Estimation of the measurement uncertainty in magnetic resonance velocimetry based on statistical models. *Experiments in Fluids*, 57(83).

Bruschewski, M., Freudenhammer, D., Schiffer, H.-P., and Grundmann, S. (2016b). Pressure field estimation from 3D MRV velocity data. In *Proceedings of the 18th International Symposium on the Application of Laser and Imaging Techniques to Fluid Mechanics*, Lisbon, Portugal.

Bruschewski, M., John, K., Wüstenhagen, C., Rehm, M., Hadžić, H., Pohl, P., and Grundmann, S. (2021b). Commissioning of an MRI test facility for

CFD-grade flow experiments in replicas of nuclear fuel assemblies and other reactor components. *Nuclear Engineering and Design*, 375:111080.

Bruschewski, M., Kolkmannn, H., John, K., and Grundmann, S. (2019). Phase-contrast single-point imaging with synchronized encoding: a more reliable technique for in vitro flow quantification. *Magnetic Resonance in Medicine*, 81(5):2937–2946.

Bruschewski, M., Piro, M. H. A., Tropea, C., and Grundmann, S. (2020). Fluid flow in a diametrally expanded CANDU fuel channel – Part 1: Experimental study. *Nuclear Engineering and Design*, 357:110371.

Bruschewski, M., Schmidt, S., John, K., Grundmann, S., and Schmitter, S. (2021c). An unbiased method for prf-shift temperature measurements in convective heat transfer systems with functional parts made of metal. *Magnetic Resonance Imaging*, 75:124–133.

Bruschewski, M., Wüstenhagen, C., Domnick, C., Krewinkel, R., Shiau, C.-C., Grundmann, S., and Han, J.-C. (2022). Assessment of the Flow Field and Heat Transfer in a Vane Cooling System Using Magnetic Resonance Velocimetry, Thermochromic Liquid Crystals, and Computational Fluid Dynamics. *Journal of Turbomachinery*, 145(3). 031010.

Buchenberg, W. B., Wassermann, F., Grundmann, S., Jung, B., and Simpson, R. (2016). Acquisition of 3d temperature distributions in fluid flow using proton resonance frequency thermometry. *Magnetic Resonance in Medicine*, 76(1):145–155.

Busco, G. and Hassan, Y. A. (2018). Space and energy-based turbulent scale-resolving simulations of flow in a 5x5 nuclear reactor core fuel assembly with a spacer grid. *International Journal of Heat and Fluid Flow*, 71:420–441.

Caraghiaur, D., Anglart, H., and Frid, W. (2009). Experimental investigation of turbulent flow through spacer grids in fuel rod bundles. *Nuclear Engineering and Design*, 239(10):2013–2021.

Castro, H. F. P. d., Silva, V. V. A., Santos, A. A. C. d., and Veloso, M. A. F. (2020). 5x5 rod bundle flow field measurements downstream a PWR spacer grid. *Brazilian Journal of Radiation Sciences*, 8(1).

Chang, S.-K., Kim, S., and Song, C.-H. (2014). Turbulent mixing in a rod bundle with vaned spacer grids: OECD/NEA–KAERI CFD benchmark exercise test. *Nuclear Engineering and Design*, 279:19–36. SI : CFD4NRS-4.

Chang, S. K., Moon, S. K., Baek, W. P., and Choi, Y. D. (2008). Phenomenological investigations on the turbulent flow structures in a rod bundle array with mixing devices. *Nuclear Engineering and Design*, 238(3):600–609. Benchmarking of CFD Codes for Application to Nuclear Reactor Safety.

Conner, M. E., Hassan, Y. A., and Dominguez-Ontiveros, E. E. (2013). Hydraulic benchmark data for pwr mixing vane grid. *Nuclear Engineering and Design*, 264:97–102. SI:NURETH-14.

Constantinides, C. D., Atalar, E., and McVeigh, E. R. (1997). Signal-to-noise measurements in magnitude images from nmr phased arrays. *Magnetic Resonance in Medicine*, 38(5):852–857.

Dyverfeldt, P., Gårdhagen, R., Sigfridsson, A., Karlsson, M., and Ebbers, T. (2009). On MRI turbulence quantification. *Magnetic Resonance Imaging*, 27(7):913–922.

Dyverfeldt, P., Kvitting, J.-P. E., Sigfridsson, A., Engvall, J., Bolger, A. F., and Ebbers, T. (2008). Assessment of fluctuating velocities in disturbed cardiovascular blood flow: In vivo feasibility of generalized phase-contrast mri. *Journal of Magnetic Resonance Imaging*, 28(3):655–663.

Dyverfeldt, P., Sigfridsson, A., Kvitting, J.-P. E., and Ebbers, T. (2006). Quantification of intravoxel velocity standard deviation and turbulence intensity by generalizing phase-contrast mri. *Magnetic Resonance in Medicine*, 56(4):850–858.

Elkins, C. J. and Alley, M. T. (2007). Magnetic resonance velocimetry: applications of magnetic resonance imaging in the measurement of fluid motion. *Experiments in Fluids*, 43:823–858.

Elkins, C. J., Alley, M. T., Saetran, L., and Eaton, J. K. (2009). Three-dimensional magnetic resonance velocimetry measurements of turbulence quantities in complex flow. *Experiments in Fluids*, 46(2):285–296.

Elkins, C. J., Markl, M., Pelc, N., and Eaton, J. K. (2003). 4D magnetic resonance velocimetry for mean velocity measurements in complex turbulent flows. *Experiments in Fluids*, 34:494–503.

Framatome (2018). GAIA Fuel Assembly - product sheet A0528-P-US-G-EN-395-05-18-GAIA. Technical report, Framatome Inc.

Frayne, R. and Rutt, B. K. (1993). Frequency response of retrospectively gated phase-contrast mr imaging: Effect of interpolation. *Journal of Magnetic Resonance Imaging*, 3(6):907–917.

Fukushima, E. (1999). Nuclear magnetic resonance as a tool to study flow. *Annual review of fluid mechanics*, 31:95.

Gao, J.-H. and Gore, J. C. (1991). Turbulent flow effects on nmr imaging: Measurement of turbulent intensity. *Medical Physics*, 18(5):1045–1051.

Gatenby, J. C. and Gore, J. C. (1994). Mapping of turbulent intensity by magnetic resonance imaging. *Journal of magnetic resonance. Series B*, 104(2):119–224.

Gladden, L. F. and Sederman, A. J. (2013). Recent advances in flow mri. *Journal of Magnetic Resonance*, 229:2–11. Frontiers of In Vivo and Materials MRI Research.

Gladden, L. F. and Sederman, A. J. (2017). Magnetic resonance imaging and velocity mapping in chemical engineering applications. *Annu Rev Chem Biomol Eng*, 8:227–247.

Griswold, M. A., Jakob, P. M., Heidemann, R. M., Nittka, M., Jellus, V., Wang, J., Kiefer, B., and Haase, A. (2002). Generalized autocalibrating partially parallel acquisitions (GRAPPA). *Magnetic Resonance in Medicine*, 47(6):1202–1210.

Gudbjartsson, H. and Patz, S. (1996). The rician distribution of noisy MRI data. *Magn Reson Med*, 34(6):910–914.

Gunady, I. E., Milani, P. M., Banko, A. J., Elkins, C. J., and Eaton, J. K. (2021). Velocity and concentration field measurements and large eddy simulation of a shaped film cooling hole. *International Journal of Heat and Fluid Flow*, 90:108837.

Haase, A., Frahm, J., Matthaei, D., Hanicke, W., and Merboldt, K.-D. (1986). FLASH imaging. rapid NMR imaging using low flip-angle pulses. *Journal of Magnetic Resonance (1969)*, 67(2):258–266.

Haraldsson, H., Kefayati, S., Ahn, S., Dyverfeldt, P., Lantz, J., Karlsson, M., Laub, G., Ebbers, T., and Saloner, D. (2018). Assessment of Reynolds stress components and turbulent pressure loss using 4D flow MRI with extended motion encoding. *Magnetic resonance in medicine*, 79(4):1962–1971.

Hasan, K. M., Parker, D. L., and Alexander, A. L. (2001). Comparison of gradient encoding schemes for diffusion-tensor mri. *Journal of Magnetic Resonance Imaging*, 13(5):769–780.

Henkelman, R. M. (1985). Measurement of signal intensities in the presence of noise in mr images. *Medical Physics*, 12(2):232–233.

Hogendoorn, W., Frank, D., Bruschewski, M., and Poelma, C. (2022). Experimental investigation of shear-induced migration in particle-laden pipe flow using mri. In *Proceedings of the 12th International Symposium on Turbulence and Shear Flow Phenomena (TSFP-12)*.

Hoult, D. and Lauterbur, P. C. (1979). The sensitivity of the zeugmatographic experiment involving human samples. *Journal of Magnetic Resonance (1969)*, 34(2):425–433.

HP Development Company, L.P. (2018). HP Multi Jet Fusion technology; Technical white paper. Technical report.

IAEA (2022). *Nuclear Power Reactors in the World, Reference Data Series No. 2*. Number 2 in Reference Data Series. International Atomic Energy Agengy (IAEA), Vienna.

Janiga, G., Stucht, D., Bordás, R., Temmel, E., Seidel-Morgenstern, A., Thévenin, D., and Speck, O. (2017). Noninvasive 4d flow characterization in a stirred tank via phase-contrast magnetic resonance imaging. *Chemical Engineering & Technology*, 40(7):1370–1327.

Jeong, J. and Hussain, F. (1995). On the identification of a vortex. *Journal of Fluid Mechanics*, 285:69–94.

John, K., Bruschewski, M., Grundmann, S., Rehm, M., Hadžić, H., and Pohl, P. (2023). Validation of fuel assembly CFD models using magnetic resonance velocimetry and turbulence measurements for 5x5 swirl type mixing vane configuration. In *CFD4NRS-9 OECD Nuclear Energy Agency (NEA) Workshop*.

John, K., Jahangir, S., Gawandalkar, U., Hogendoorn, W., Poelma, C., Grundmann, S., and Bruschewski, M. (2020). Magnetic resonance velocimetry in high-speed turbulent flows: sources of measurement errors and a new approach for higher accuracy. *Experiments in Fluids*, 61:1–17.

John, K., Wüstenhagen, C., Schmidt, S., Schmitter, S., Bruschewski, M., and Grundmann, S. (2022). Reynolds stress tensor and velocity measurements in technical flows by means of magnetic resonance velocimetry. *tm - Technisches Messen*, 89(3):201–209.

Kestin, J., Sokolov, M., and Wakeham, W. A. (1978). Viscosity of liquid water in the range −8 to 150°C. *Journal of Physical and Chemical Reference Data*, 7(3):941–948.

Kuethe, D. O. (1989). Measuring distributions of diffusivity in turbulent fluids with magnetic-resonance imaging. *Physical Review A*, 40(8):4542.

Kuethe, D. O. and Gao, J.-H. (1995). NMR signal loss from turbulence: Models of time dependence compared with data. *Phys. Rev. E*, 51:3252–3262.

Larson 3rd, T. C., Kelly, W. M., Ehmann, R. L., and Wehrli, F. W. (1991). Spatial misregistration of vascular flow during MR imaging of the CNS: cause and clinical significance. *American journal of neuroradiology*, 5(11):1041–1048.

Lauterbur, P. C. (1973). Image formation by induced local interactions: examples employing nuclear magnetic resonance. *Nature*, 242(5394):190–191.

Lee, J. R., Kim, J., and Song, C.-H. (2014). Synthesis of the turbulent mixing in a rod bundle with vaned spacer grids based on the oecd-kaeri cfd benchmark exercise. *Nuclear Engineering and Design*, 279:3–18. SI : CFD4NRS-4.

Lustig, M., Donoho, D., and Pauly, J. M. (2007). Sparse mri: The application of compressed sensing for rapid mr imaging. *Magnetic Resonance in Medicine*, 58(6):1182–1195.

Mansfield, P. and Grannell, P. K. (1973). NMR 'diffraction' in solids? *Journal of Physics C: Solid State Physics*, 6(22):L422.

Mark Mitchell, Baurzhan Muftakhidinov, T. W. e. a. (2019). Engauge digitizer software, v12.1.

Markl, M., Chan, F. P., Alley, M. T., Wedding, K. L., Draney, M. T., Elkins, C. J., Parker, D. W., Wicker, R., Taylor, C. A., Herfkens, R. J., and Pelc, N. J. (2003). Time-resolved three-dimensional phase-contrast MRI. *Journal of Magnetic Resonance Imaging*, 17(4):499–506.

Markl, M., Frydrychowicz, A., Kozerke, S., Hope, M., and Wieben, O. (2012). 4D flow MRI. *Journal of Magnetic Resonance Imaging*, 36(5):1015–1036.

Matozinhos, C. F., Tomaz, G. C., Nguyen, T., dos Santos, A. A., and Hassan, Y. (2020). Experimental measurements of turbulent flows in a rod bundle with a 3-d printed channel-type spacer grid. *International Journal of Heat and Fluid Flow*, 85:108674.

Matozinhos, C. F., Tomaz, G. C., Nguyen, T., and Hassan, Y. (2021). Experimental investigation of turbulent flow characteristics in cross-flow planes of a 5×5 rod bundle with a spacer grid. *International Journal of Heat and Fluid Flow*, 87:108757.

McKeon, B., Comte-Bellot, G., Foss, J., Westerweel, J., Scarano, F., Tropea, C., Meyers, J., Lee, J., Cavone, A., Schodl, R., Koochesfahani, M., Andreopoulos, Y., Dahm, W., Mullin, J., Wallace, J., Vukoslavčević, P., Morris, S., Pardyjak, E., and Cuerva, A. (2007). Velocity, vorticity, and mach number. In Tropea, C., Yarin, A. L., and Foss, J. F., editors, *Springer Handbook of Experimental Fluid Mechanics*, pages 215–471. Springer Berlin Heidelberg, Berlin, Heidelberg.

McRobbie, D. W., Moore, E. A., Graves, M. J., and Prince, M. R. (2006). *MRI from picture to proton*. Cambridge University Press, 2 edition.

Moran, P. R. (1982). A flow velocity zeugmatographic interlace for NMR imaging in humans. *Magnetic Resonance Imaging*, 1(4):197–203. Second Annual Meeting of the Society for Magnetic Resonance Imaging.

NEA (2002). Proceedings of the exploratory meeting of experts to define an action plan on the application of computational fluid dynamics (CFD) codes to nuclear reactor safety problems - aix en provence - 15-16 may 2002. *OECD Publishing*.

NEA (2013). Report of the OECD/NEA KAERI rod bundle CFD benchmark exercise. *OECD Publishing*.

NEA (2014). Extension of CFD codes application to two-phase flow safety problems - phase 3. *OECD Publishing*.

NEA (2015a). Assessment of cfd codes for nuclear reactor safety problems - revision 2. *OECD Publishing*.

NEA (2015b). Best practice guidelines for the use of cfd in nuclear reactor safety applications - revision. *OECD Publishing*.

NEA (2022). Requirements for CFD-grade experiments for nuclear reactor thermal hydraulics. *OECD Publishing*.

Nishimura, D. G., Jackson, J. I., and Pauly, J. M. (1991). On the nature and reduction of the displacement artifact in flow images. *Magnetic Resonance in Medicine*, 22(2):481–492.

Oliveira, A. V. S., Stemmelen, D., Leclerc, S., Glantz, T., Labergue, A., Repetto, G., and Gradeck, M. (2020). Velocity field and flow redistribution in a ballooned 7×7 fuel bundle measured by magnetic resonance velocimetry. *Nuclear Engineering and Design*, 369:110828.

Oliveira, A. V. S., Stemmelen, D., Leclerc, S., Glantz, T., Labergue, A., Repetto, G., and Gradeck, M. (2021). Parametric effects on the flow redistribution in ballooned bundles evaluated by magnetic resonance velocimetry. *Experimental Thermal and Fluid Science*, 125:110383.

Panton, R., Kheirandish, S., and Wagner, M. (2007). Experiment as a boundary-value problem. In Tropea, C., Yarin, A. L., and Foss, J. F., editors, *Springer Handbook of Experimental Fluid Mechanics*, chapter A-1, pages 3–31. Springer Berlin Heidelberg, Berlin, Heidelberg.

Pelc, N. J., Bernstein, M. A., Shimakawa, A., and Glover, G. H. (1991). Encoding strategies for three-direction phase-contrast MR imaging of flow. *Journal of Magnetic Resonance Imaging*, 1(4):405–413.

Piro, M., Wassermann, F., Grundmann, S., Tensuda, B., Kim, S., Christon, M., Berndt, M., Nishimura, M., and Tropea, C. (2017). Fluid flow investigations within a 37 element candu fuel bundle supported by magnetic resonance velocimetry and computational fluid dynamics. *International Journal of Heat and Fluid Flow*, 66:27–42.

Piro, M. H. A., Christon, M., Tensuda, B., Poschmann, M., Bruschewski, M., Grundmann, S., and Tropea, C. (2020). Fluid flow in a diametrally expanded CANDU fuel channel – Part 2: Computational study. *Nuclear Engineering and Design*, 357:110372.

Piro, M. H. A., Wassermann, F., Grundmann, S., Leitch, B. W., and Tropea, C. (2016). Progress in on-going experimental and computational fluid dynamic investigations within a CANDU fuel channel. *Nuclear Engineering and Design*, 299:184–200. CFD4NRS-5.

Pope, S. B. (2000). *Turbulent Flows*. Cambridge University Press.

Pruessmann, K. P., Weiger, M., Scheidegger, M. B., and Boesiger, P. (1999). SENSE: Sensitivity encoding for fast MRI. *Magnetic Resonance in Medicine*, 42(5):952–962.

Qu, W., Xiong, J., Chen, S., Qiu, Z., Deng, J., and Cheng, X. (2019). PIV measurement of turbulent flow downstream of mixing vane spacer grid in 5x5 rod bundle. *Annals of Nuclear Energy*, 132:277–287.

Rehme, K. (1973). Pressure drop correlations for fuel element spacers. *Nuclear Technology*, 17(1):15–23.

Rehme, K. and Trippe, G. (1980). Pressure drop and velocity distribution in rod bundles with spacer grids. *Nuclear Engineering and Design*, 62(1):349–359.

Richardson, D. B., MacFall, J. R., Sostman, H. D., and Spritzer, C. E. (1994). Asymmetric-echo, short te, retrospectively gated mr imaging of the heart and pulmonary vessels. *Journal of Magnetic Resonance Imaging*, 4(2):131–137.

Roemer, P. B., Edelstein, W. A., Hayes, C. E., Souza, S. P., and Mueller, O. M. (1990). The nmr phased array. *Magnetic Resonance in Medicine*, 16(2):192–225.

Romano, G., Ouellette, N., Xu, H., Bodenschatz, E., Steinberg, V., Meneveau, C., and Katz, J. (2007). Measurements of turbulent flows. In Tropea, C., Yarin, A. L., and Foss, J. F., editors, *Springer Handbook of Experimental Fluid Mechanics*, pages 745–855. Springer Berlin Heidelberg, Berlin, Heidelberg.

Rowe, D. S. (1973). *Measurement of turbulent velocity, intensity and scale in rod bundle flow channels*. Oregon State University.

Schmalbrock, P., Yuan, C., Chakeres, D. W., Kohli, J., and Pelc, N. J. (1990). Volume MR angiography: methods to achieve very short echo times. *Radiology*, 175(3):861–865.

Schmidt, S., Bruschewski, M., Flassbeck, S., John, K., Grundmann, S., Ladd, M. E., and Schmitter, S. (2021a). Phase-contrast acceleration mapping with synchronized encoding. *Magnetic Resonance in Medicine*, 86(6):3201–3210.

Schmidt, S., Flassbeck, S., Bachert, P., Ladd, M. E., and Schmitter, S. (2020). Velocity encoding and velocity compensation for multi-spoke RF excitation. *Magnetic Resonance Imaging*, 66:69–85.

Schmidt, S., John, K., Kim, S. J., Flassbeck, S., Schmitter, S., and Bruschewski, M. (2021b). Reynolds stress tensor measurements using magnetic resonance velocimetry: expansion of the dynamic measurement range and analysis of systematic measurement errors. *Experiments in Fluids*, 62(121).

Stadler, A., Schima, W., Ba-Ssalamah, A., Kettenbach, J., and Eisenhuber, E. (2007). Artifacts in body mr imaging: their appearance and how to eliminate them. *European radiology*, 17:1242–1255.

Tayler, A. B., Holland, D. J., Sederman, A. J., and Gladden, L. F. (2011). Time resolved velocity measurements of unsteady systems using spiral imaging. *Journal of Magnetic Resonance*, 211(1):1–10.

Tropea, C., Yarin, A. L., Foss, J. F., et al. (2007). *Springer handbook of experimental fluid mechanics*, volume 1. Springer.

Uecker, M., Lai, P., Murphy, M. J., Virtue, P., Elad, M., Pauly, J. M., Vasanawala, S. S., and Lustig, M. (2014). ESPIRiT—an eigenvalue approach to autocalibrating parallel MRI: Where SENSE meets GRAPPA. *Magnetic Resonance in Medicine*, 71(3):990–1001.

Untenberger, M., Tan, Z., Voit, D., Joseph, A. A., Roeloffs, V., Merboldt, K. D., Schätz, S., and Frahm, J. (2016). Advances in real-time phase-contrast flow MRI using asymmetric radial gradient echoes. *Magnetic Resonance in Medicine*, 75(5):1901–1908.

Wapler, M. C., Leupold, J., Dragonu, I., von Elverfeld, D., Zaitsev, M., and Wallrabe, U. (2014). Magnetic properties of materials for mr engineering, micro-mr and beyond. *Journal of Magnetic Resonance*, 242:233–242.

Wood, M. L. and Henkelman, R. M. (1985). Mr image artifacts from periodic motion. *Medical Physics*, 12(2):143–151.

Wüstenhagen, C., Domnick, C. B., John, K., Bruschewski, M., and Grundmann, S. (2023). MRV Measurements of Internal Blade Cooling Flow and CFD Validation by Data Matching with the Experimental Data. *Journal of Thermal Science and Engineering Applications*, pages 1–33.

Wüstenhagen, C., John, K., Langner, S., Brede, M., Grundmann, S., and Bruschewski, M. (2021). CFD validation using in-vitro MRI velocity data – methods for data matching and CFD error quantification. *Computers in Biology and Medicine*, 131:104230.

Xiong, J., Qu, W., Zhang, T., Chai, X., Liu, X., and Yang, Y. (2020). Experimental investigation on split-mixing-vane forced mixing in pressurized water reactor fuel assembly. *Annals of Nuclear Energy*, 143:107450.

Zwart, N. R. and Pipe, J. G. (2013). Multidirectional high-moment encoding in phase contrast mri. *Magnetic Resonance in Medicine*, 69(6):1553–1563.